

ROBUST CONTROL OF SYSTEMS WITH PIECEWISE LINEAR HYSTERESIS

By

Mohamed Mohamed Edardar

A DISSERTATION

Submitted to
Michigan State University
in partial fulfillment of the requirements
for the degree of

Electrical Engineering - Doctor of Philosophy

2013

ABSTRACT

ROBUST CONTROL OF SYSTEMS WITH PIECEWISE LINEAR HYSTERESIS

By

Mohamed Mohamed Edardar

Hysteresis nonlinearity is found in many control system applications such as piezo-actuated nanopositioners. The positioner is represented as a linear system preceded by hysteresis. This hysteresis nonlinearity is usually modeled by operators in order to simulate their effects in the closed-loop system or to use their inverse to compensate for their effects. In order to reduce the hysteresis effect, an approximate inverse operator is used as a feedforward compensator. The first part of our work considers driving an upper bound on the inversion error using the hysteresis model. This bound is a function of the input references, which is much less conservative than constant bounds. It is used in designing the closed-loop control systems.

The second part is to design feedback controller to achieve the desired performance. Three different methods are used throughout this work and a comparison between them is also provided. First, we use the conventional proportional Integral (PI) control method, which is extensively used in commercial applications. However, in our method we add a feedforward component which improves the performance appreciably. Second, a sliding-mode-control (SMC) scheme is used because it is one of the very powerful nonlinear robust control methods. Other schemes like high gain feedback and Lyapunov redesign have close results to SMC and hence it is not included in this work. The third control is H_∞ control. It is a robust linear control method, which deals with uncertainty in the system in an optimal control structure. Unlike the PI controller, the H_∞ controller uses the features of the linear plant in the design which allows to accomplish more than the simple PI controller. Mainly, it can shape the closed-loop transfer function of the system to achieve the

design objectives.

Including the operators in the closed-loop system, makes it hard to obtain explicit solutions of the dynamics using conventional methods. We exploit two features of piezoelectric actuators to provide a complete solution of the tracking error. First, the hysteresis is approximated by a piecewise linear operator. Second, the linear plant has a large bandwidth which allows using singular perturbation techniques to put the system in a two time-scale structure. We show that the slope of a hysteresis loop segment plays an important role in determining the error size. Our analysis also shows how error is affected by increasing the frequency of the reference input. We verify that the accumulation of the error, which is propagating from segment to another is bounded and derive its limit. We provide a comparison between simulation and the analytic expressions of the tracking error at different frequencies. Experimental results are also presented to show the effectiveness of our controllers compared with other techniques.

To my Mother, Father, and Family

ACKNOWLEDGMENTS

It has been a wonderful opportunity to study in Michigan State university with those prominent professors in control engineering field. I am grateful to my main advisor Prof. H. K. Khalil and my co-advisor Prof. X. Tan for their guidance, patience and encouragement. They inspired me with their splendid methods throughout my research. I also thank them for their advices which were very important to ease my way on modeling the system, design different controllers, analyze them and run different simulations and experiments.

I would like to thank Prof. G. Zho and Prof. R. Mukerjii for kindly joining my research committee and for their continuous advices and their willingness to help whenever I ask.

I am so grateful to my colleagues and friends, Particularly A. Esbrook who was very helpful and I extend my congratulation to him for his graduation in 2012.

I would like to thank my wife for her support and the dedicated time to look after my family while I was busy in conducting my research.

TABLE OF CONTENTS

LIST OF TABLES	viii
LIST OF FIGURES	ix
Chapter 1 Introduction	1
1.1 Background	1
1.2 Piezoelectric Actuators	3
1.3 Hysteresis Models	3
1.3.1 Preisach Operator	5
1.3.2 Prandtl-Ishlinskii (PI) Operator	7
1.4 Hysteresis Inverse Compensation	8
1.5 Feedback Control	9
1.5.1 Adaptive Control	9
1.5.2 Robust Control	10
1.5.3 Integral Control	11
1.6 The Research Objective	13
1.7 Research Overview	13
1.8 Dissertation Layout	15
Chapter 2 Hysteresis Model and Inversion Error	17
2.1 Introduction	17
2.2 Characterization of the inversion error	17
2.3 The Inversion Error Bound Using the Slope-Intercept Method	19
2.4 The Inversion Error Bound Using the Weight-Threshold Method	22
2.5 The Relationship Between Segment Slope and Operator Weights	26
2.6 The Relationship Between Segment Intercept and Operator Weights	28
2.7 Simulation of the Hysteresis Loops Based on the Experimental Data	31
2.8 Example of Calculating Bounds on the Inversion Error	32
2.9 Summary	41
Chapter 3 Quantifying the Tracking Error with Proportional-Integral-Controller	42
3.1 Introduction	42
3.2 Closed-Loop System Setup	44
3.3 Tracking Error Analysis	47
3.3.1 Analysis Using the Slow Model Approximation	47

3.3.2	System Model and Coordinates Transformation	50
3.3.3	The Case of a Sinusoidal Reference	52
3.3.4	Bound on All Segments	57
3.3.5	The Case of Periodic References	59
3.4	Simulation, and Experimental Results	61
3.4.1	Simulation Results versus Analytical Results	62
3.4.2	Experimental Results	67
3.5	Mathematical Derivations	69
3.5.1	Slow and Fast Variables in ξ and η Coordinates	69
3.5.2	Solution of ξ_0	73
3.5.3	Calculating the Bound on φ	77
3.5.4	Solution for ξ_1	79
3.5.5	Fast Variable Analysis	80
3.5.6	Calculating the Bound on the Frequency-dependent Term of the Error	85
3.6	Summary	86
Chapter 4	Sliding Mode Control Design	89
4.1	Introduction	89
4.2	Controller Design	91
4.2.1	System Scaling	95
4.3	Determining the tracking error inside the boundary layer	97
4.3.1	Example of the Second Order System	99
4.3.2	Tracking Error for a Sinusoidal Reference	100
4.4	Tracking Error at the Steady State	104
4.5	Simulation Results	106
4.6	Experimental Results	115
4.7	Summary	118
Chapter 5	H_∞ Control Design	124
5.1	Introduction	124
5.2	Problem Formulation	125
5.3	Control System Design and Analysis	128
5.4	Simulation Comparison between including and not including the inverse operator with H_∞ control	131
5.5	Simulation Comparison between H_∞ and PI control	133
5.6	Simulation Comparison between H_∞ , PI, and SMC control	133
5.7	Summary	137
Chapter 6	Conclusion and Future Work	139
6.1	Conclusions	139
6.2	Future Work	142
	BIBLIGORAPHY	145

LIST OF TABLES

Table 3.1	Simulation, analytical, and experimental results on maximum tracking errors in μm for a system involving a perturbed PI-operator and a second-order plant.	88
Table 3.2	Experimental results on maximum tracking errors in μm with and without feedforward compensation.	88
Table 4.1	Comparison between maximum tracking errors for SMC-, MHSC- and SHSC- methods	117
Table 4.2	Comparison between mean tracking errors for SMC-, MHSC- and SHSC- methods	117
Table 5.1	Simulation results providing a comparison between maximum tracking errors for PI, SMC, and H_∞ control	138

LIST OF FIGURES

Figure 1.1:	Major and minor hysteresis loops. For interpretation of the references to color in this and all other figures, the reader is referred to the electronic version of this dissertation.	2
Figure 1.2:	A general control framework for systems preceded by hysteresis [1]	3
Figure 1.3:	The relay operator with parameters α and β	5
Figure 1.4:	The play operator with threshold paramter r	6
Figure 2.1:	Illustration of a hysteresis loop with piecewise linear characteristics. . . .	18
Figure 2.2:	A system with hysteresis preceded by an inverse operator.	19
Figure 2.3:	Inversion error bounds using slop-intercept method.	20
Figure 2.4:	A play operator: the building block of a PI operator.	24
Figure 2.5:	Illustration of the initial loading curve.	28
Figure 2.6:	Ascending branches of hysteresis operator and inverse-operator.	29
Figure 2.7:	Experimental setup includes the nanopositioner Nano-OP65, power drive, and ADC/DAC converter.	32
Figure 2.8:	Measured hysteresis loops.	33
Figure 2.9:	Comparison between the measured hysteresis loop and the operator hysteresis loop.	34
Figure 2.10:	Positioner output used in the PI identification and the resulting model output.	35
Figure 2.11:	The output and inversion error of a perturbed PI operator.	36

Figure 2.12:	Hysteresis loops for a non-perturbed and a perturbed PI operator with a perturbation $\Delta_{w,max} = 0.15$	39
Figure 2.13:	The inversion error of a perturbed PI operator with a $50 \mu\text{m}$ input.	40
Figure 3.1:	Illustration of a hysteresis loop with piecewise linear characteristics.	43
Figure 3.2:	Hysteresis inversion with a control that integrates feedforward with feedback.	44
Figure 3.3:	Hysteresis inverse in the feedback loop.	46
Figure 3.4:	Illustration of the time instants when periodic signals cross different linear segments of the hysteresis loops.	52
Figure 3.5:	Simulations results on tracking a periodic reference composed of two sinusoidal signals of 25 Hz and 50 Hz.	63
Figure 3.6:	Simulation results on tracking a sawtooth reference of 5 Hz.	64
Figure 3.7:	Simulation results on tracking a sawtooth reference with and without feedforward compensation, under perfect hysteresis inversion.	65
Figure 3.8:	Simulation results on tracking a sawtooth reference when uncertainty is present/absent in the hysteresis model.	66
Figure 3.9:	Comparison of simulation and analytical results on the tracking error as the reference frequency is varied.	66
Figure 3.10:	Experimental results on the tracking error for sinusoidal references of different frequencies.	68
Figure 3.11:	Comparison of simulation and experimental results on the tracking error as the reference frequency is varied.	69
Figure 3.12:	Experimental results on the tracking of a triangular reference.	70
Figure 3.13:	Experimental results on the tracking of a multi-sine reference with frequencies of 15 Hz and 30 Hz.	71
Figure 3.14:	Comparison of tracking error with and without feedforward component (a) a triangular reference (b) multi-sine reference.	72

Figure 4.1:	A general control framework for systems preceded by hysteresis.	90
Figure 4.2:	Simulation results on tracking a van der Pol oscillator-generated reference: position, tracking error and s trajectories. The bounds are calculated using slope-intercept method	107
Figure 4.3:	Simulation results on tracking a Van Der Pol oscillator-generated reference: position, tracking error and s trajectories. The bounds are calculated using weight-threshold method	108
Figure 4.4:	Tracking error with different $\Delta_{w,max}$	110
Figure 4.5:	Comparison of simulation and analytical results on the tracking error at different frequencies.	111
Figure 4.6:	Simulation results of the tracking error of 1 Hz, 50 Hz, and 200 Hz sinusoidal references.	111
Figure 4.7:	Simulation results when SMC uses only a switching control to dominate both known and uncertain terms (case 1) and when it uses a switching control to dominate the uncertain terms and equivalent control to cancel the known terms (case 2).	112
Figure 4.8:	Simulation results of the tracking error for different values of β for the same value of μ	113
Figure 4.9:	Simulation results show tracking of sinusoidal references with and without rate limiter for 100 Hz and 200 Hz.	114
Figure 4.10:	Experimental results on tracking a 10 Hz sinusoidal reference. The curve “mea.” was obtained from measurement, while “ref” represents the reference signal.	116
Figure 4.11:	Experimental results at steady state (a) applied control signal on actuator (b) Tracking Error.	118
Figure 4.12:	Experimental results show tracking of sinusoidal references at (a) 100 Hz and (b) 200 Hz.	119
Figure 4.13:	A comparison between experimental and simulation results when the rate limiter is included in the simulated system.	120

Figure 4.14:	Experimental results of the tracking error with saturation function of $5\mu\text{m}$ amplitude.	121
Figure 4.15:	Experimental results of the tracking error with saturation function of $25\mu\text{m}$ amplitude.	122
Figure 5.1:	The closed-loop system with the inversion error represented as multiplicative uncertainty.	126
Figure 5.2:	A general robust control framework for systems uncertainties.	127
Figure 5.3:	Adding weight functions in the closed-loop system for optimal design. . .	128
Figure 5.4:	Two degree of freedom feedback design.	129
Figure 5.5:	Simulations results of H_∞ control with and without inverse-operator at frequencies (a) 25 Hz and (b) 100 Hz.	132
Figure 5.6:	Simulations results for tracking error with PI and H_∞ control for frequencies a) 350 Hz, b) 50 Hz, c) 1 Hz.	134
Figure 5.7:	Simulations results for tracking error with PI and H_∞ control: a) without rate limiter at 50 Hz, b) with rate limiter at 50 Hz, c) without rate limiter at 90 Hz, and d) with rate limiter at 90 Hz.	135
Figure 5.8:	Simulations results for comparing the changes of the tracking errors with frequency for PI, SMC, and H_∞ control.	137

Chapter 1

Introduction

1.1 Background

Hysteresis nonlinearities exist in many control applications, especially those involving smart material-enabled actuators or sensors [2]. Examples of smart materials are piezoelectrics [3], magnetostrictives [1], shape memory alloys [2, 4], electro-active polymers [5], magnetorheological fluids [1], and conjugated polymers [6]. In recent years, nanotechnology has attracted many researchers because it has wide applications. One of the pivotal requirements of nanotechnology is nanopositioning. Piezoelectric actuators are commonly used in nanopositioning applications such as scanning tunneling microscopes (STM) and atomic force microscopes (AFM). They have large bandwidth and can produce large mechanical force [7, 8]. They are typically used for positioning in the range of $10\ \mu\text{m}$ to $100\ \mu\text{m}$ [7]. However, because piezoelectric materials are ferroelectric, they exhibit non-desirable behaviors such as hysteresis, creep, and vibrations [9]. Hysteresis, which is depicted in Fig. 1.1, is a nonlinear phenomenon that not only exists in smart materials but also in various areas, such as: biology, geology, mechanics, and economics. It presents challenges in both understanding and control of such systems. Modeling, analysis, and control of systems with hysteresis has received great attention over the last two decades [7].

To effectively control a system with hysteresis, the first important task is to characterize the hysteresis nonlinearities. Hysteresis models can be roughly classified into physics-based mod-

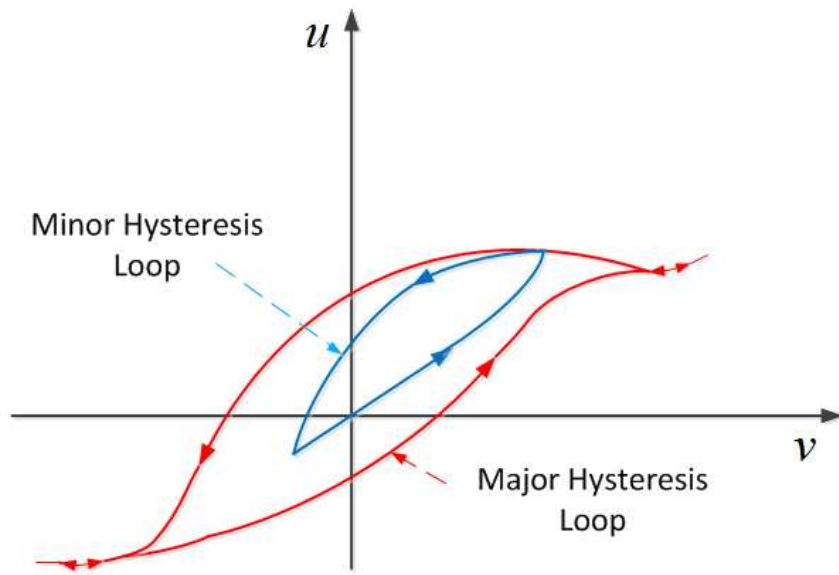


Figure 1.1: Major and minor hysteresis loops. For interpretation of the references to color in this and all other figures, the reader is referred to the electronic version of this dissertation.

els and phenomenological models. Physics-based models are based on first principles of physics [10]. Phenomenological models are used to produce behaviors similar to those of the physical system without necessarily providing physical insight into the problem. A dominant class of phenomenological hysteresis models are formed through weighted superposition of elementary hysteresis units, and notable examples of such models include the Preisach model [11] and the Prandtl-Ishlinskii (PI) model [12]. The Preisach model is parametrized by a pair of threshold variables, whereas the PI model is parametrized by a single threshold variable.

With the developments in various hysteresis models, it is natural to seek means to fuse these hysteresis models with the available control techniques to mitigate the effects of hysteresis. One of the most common approaches in coping with hysteresis is to construct an inverse operator [1] and integrate it with feedback techniques, as illustrated in Fig. 1.2 .

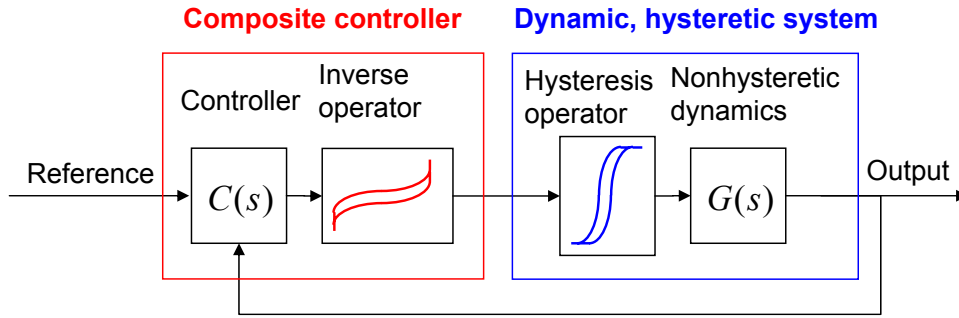


Figure 1.2: A general control framework for systems preceded by hysteresis [1]

1.2 Piezoelectric Actuators

The piezoelectric effect was first discovered in 1880 [7]. It was found that squeezing certain materials (Piezein) resulted in electric charge. However, the use of piezo-electric materials as actuators exploits the converse effect, i.e., the application of electric voltage results in mechanical strain. The main design parameters that characterize the performance of an actuator are displacement range, force, bandwidth (frequency range), size, weight, and power consumption. Piezoelectric actuators have excellent operating bandwidth and can generate large mechanical forces in a compact design for small amounts of power, but they have a relatively small displacement range.

Due to the key role played by piezoelectric actuators and the increase interest in using model-based control design of these devices, interest in understanding the dynamics of these actuators has increased. Two of these dynamics are linear which are creep and vibrations the other one is nonlinear which is hysteresis.

1.3 Hysteresis Models

Models of hysteresis have evolved from two different branches of physics: ferromagnetism [13] and plasticity theory [14]. The roots of both branches go back to the end of th 19th century [15].

The core of this theory is formed by the so-called hysteresis operators which describe hysteretic transducers as a mapping between function spaces. It is only in the 1970's when researchers started to couple the mathematical theory of ordinary differential equation with hysteresis operators [16, 17]. In the 1990s, engineers employed this theory on a larger scale to develop modern strategies for the linearization of hysteretic nonlinearities with an inverse feedforward controller [15]. To successfully exploit the full potential of piezoelectrical transducers in control schemes, it is essential to understand and model their behavior accurately. When the output is plotted against the input, the plots for increasing or decreasing inputs are different and form a loop. See Fig 1.1. Early models used polynomials to capture the major loops in the I/O response. However, such approaches fail to capture the inner (minor) loops.

The Preisach operator [18] was used for modelling and linearization of complex hysteretic nonlinearities occurring in solid-state actuators with the inverse feedforward control approach [19, 20]. But the main drawbacks of the Preisach operator are the strong sensitivity of the identification procedure against input-output data and unknown model errors and the fact that in general the compensator of the Preisach operator has to be calculated numerically. Recent papers also reference the so-called Prandtl-Ishlinskii (PI) operator [21, 15, 12, 22] which belongs to an important subclass of the Preisach operator [23]. The main advantages of this approach are reduced model complexity of the PI-operator in comparison with the Preisach operator and the fact that the compensator of an invertible Prandtl-Ishlinskii operator can be calculated analytically. This allows an efficient implementation of the compensator for real time application.

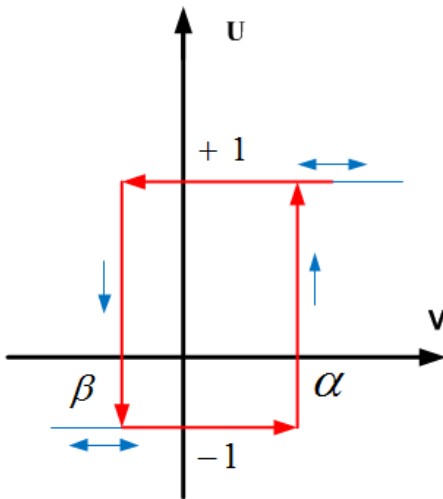


Figure 1.3: The relay operator with parameters α and β .

1.3.1 Preisach Operator

The Preisach model [24, 25, 26, 27, 28, 29, 30] for electromagnetic hysteresis dates from 1935 [31]. This model uses a superposition of simple independent relay operators shown in Fig 1.3. It has been successful in the modeling of hysteresis observed in ferromagnetic, magnetostrictive, and piezoelectric materials. However, in designing with these smart materials, one has to determine the density function for the preisach operator by using input-output behavior of the material at hand [32].

In the past, several researchers have addressed the problem of identifying the preisach density function. Mayergoyz [18] first described a method to identify the density function in the proof of his representation theorem. However, this method has limited applicability in practice when the output signal is corrupted by noise, as it involves a differentiation of the output signal. There are other methods to determine the density function. The most popular involves discretizing the Preisach plane, and identifying step-function approximation to the actual density function via a linear least-squares method. Haffmann and Meyer [33] were perhaps the first to use this method.

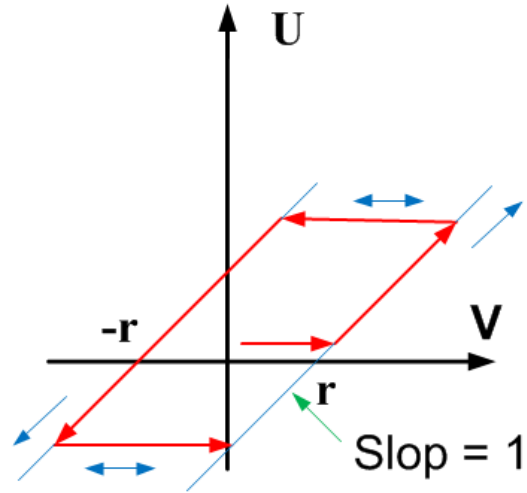


Figure 1.4: The play operator with threshold paramter r .

In this method, no assumptions are made about the actual density function [32]. In [32], the authors consider the basic problem of identifying the Preisach density function when there is not sufficient experimental data. They use singular value decomposition along with a linear least squares method to efficiently identify the best approximation to the density function. In this method, they do not need to process a large amount of data to obtain the density function. In [25], Hysteresis is modeled by Preisach operator with a piecewise uniform density function. It addresses recursive identification and adaptive inverse control of hysteresis. Two classes of identification schemes are proposed and compared, one based on the hysteresis output, the other based on the time-difference of the output. In [24], a model that predicts the expansion of piezoceramic actuators when subject to dynamic-voltage excitations is developed as an extension of the classical Preisach model. The model is presented in a recursive form that is suitable for real-time implementation.

1.3.2 Prandtl-Ishlinskii (PI) Operator

The PI operator dates to 1944 [31], and was proposed as a model for plasticity-elasticity. The foundation of this model is using elementary hysteresis operators, which have simple mathematical structures. One of the most familiar and most important elementary hysteretic mapping between the input signal V and the output U is so called play or backlash operator, which is shown in Fig. 1.4 and described by the following equation. The output of a PI operator [12] can be represented as

$$\Gamma[V] = w^T H_r[V, z_0](t) \quad (1.1)$$

where, $H_r = [H_{r0} H_{r1} \dots H_{r,n-1}]^T$ is the vector of individual play operators, $w^T = [w_0 w_1 \dots w_{n-1}]$ is the vector of weights for individual play operators, $r^T = [r_0 r_1 \dots r_{n-1}]$ with $0 = r_0 < r_1 < \dots < r_{n-1} < \infty$ represents the set of thresholds for the play operators, $z_0^T = [z_{00} z_{01} \dots z_{0,n-1}]$ denotes the initial condition of the PI operator, and n is the number of play operators.

The play operator is defined by

$$H_{ri}[V, z_0] = \max\{V - r_i, \min\{V + r_i, z_{0i}\}\} \quad (1.2)$$

where $i = 0, 1, \dots, n$.

K. Kuhnen published several papers that describe modeling hysteresis by PI-operator [34, 15, 21, 12, 35]. In [34, 35], a simultaneous compensation of the hysteresis and creep transfer characteristics of a piezoelectric stack actuator by interposing an inverse system in an open loop control is described. The maximum linearity error caused by hysteresis and creep effects is lowered by an order of magnitude. It is limited to systems with one input signal.

In [21], an approach introduces the compensation of the hysteretic stack transducers by an

adaptive inverse hysteretic control. Starting with a linear characteristic, the weights of an inverse hysteretic observer are identified during operation by a stable adaptive law and transformed to the controller parameter. Linear dynamics of the actuator are not considered in this approach. Another compensator design method for invertible complex hysteretic nonlinearities is described in [15]. The parameter identification of this model can be formulated as quadratic optimization problem which produces the best L_2 -norm approximation for the measured input-output data of the real hysteretic nonlinearity. Special linear inequality constraints for the parameters guarantee the unique solvability of the identification problem and the invertibility of the identified model. This leads to robustness of the identification procedure against unknown measurement errors and unknown model errors. The corresponding compensator can be directly calculated and thus efficiently implemented from the model by analytic transformation laws. This method was applied on magnetostrictive actuator and reduced error 10 times. In [12], the author extends his work by modifying the operator in order to remove the main drawback of the PI operator, which is its symmetric characteristic. A one-sided dead zone operator is added to modify the PI-operator and make it asymmetrical.

1.4 Hysteresis Inverse Compensation

The control methods that deal with hysteresis are classified into open-loop inverse compensation or feedback control methods, which usually include the inverse operator. Inverse open-loop methods [15, 12, 36] demonstrate that they can reduce the tracking error appreciably, but they are susceptible to model uncertainties and environmental changes. Therefore, a general approach in coping with hysteresis is to construct an inverse operator and integrate it with feedback techniques, as illustrated in Fig. 1.2.

1.5 Feedback Control

Two major groups of feedback control are the classical integral control and modern methods using adaptive and robust control. The main challenge in feedback designs is performance improvement while maintaining the stability of the overall system in the presence of parameter uncertainty and unmodeled high-frequency vibrational modes [37]. Control techniques include high gain feedback [38, 39], adaptive control [25, 40, 41], and robust control [42, 43, 44, 45, 46]. Next, we review the application of these techniques to systems with hysteresis.

1.5.1 Adaptive Control

A main concern in feedback control is stability. Stability analysis for hysteretic systems involving adaptation is presented in [47, 25, 36, 48] under various persistent-excitation-type conditions on the reference signals. In [36] Tao and Kokotovic present a model-reference adaptive inverse scheme for a linear system preceded by a piecewise-linear hysteresis model, and establish global boundedness of the closed-loop signals. In [25], Tan and Baras establish asymptotic tracking for an adaptive inverse algorithm and characterize the parameter convergence behavior for a system modeled by a Preisach operator (without dynamics). Tan and Khalil [48] present a two-time-scale averaging framework for systems with hysteresis, and show that, with slow adaptation, a model-reference adaptive inverse control scheme can achieve arbitrarily small tracking and parameter estimation error when the initial parameter error is sufficiently small. Chen *et al.* [47] prove boundedness of the closed-loop signals under a pseudo-inverse-based adaptive control scheme for

a class of uncertain discrete time systems preceded by hysteresis.

1.5.2 Robust Control

Robust control methods for hysteresis control include for example integral control [49, 50, 51, 52, 53, 43], servo-compensators [54, 55], sliding-mode control (SMC) [56, 57, 58, 59, 60, 61], and H_∞ Control [62, 63, 64, 65]. In these methods, researchers avoid the complex adaptation algorithms and typically assume that a bound on the inversion error is known. For the servocompensator method [55], Esbrook *et al.* show that for T -periodic inputs, trajectories converge to exponentially stable T -periodic solutions. In the SMC methods, Shen *et al.* [56] and Bashash and Jalili [57] use Lyapunov functions to show stability or ultimate boundedness. In [1], Tan and Baras apply an l_1 robust control scheme to a magnetostrictive actuator to accommodate control input constraints and minimize the tracking error.

In order to obtain good tracking performance, most H_∞ control methods are implemented in the Two-Degree-of-Freedom (2DOF) framework. In [62], a novel approach is proposed in which no hysteresis inversion is included. Usually feedforward control is augmented with feedback control to account for adverse effects such as dynamic variations and disturbances. The philosophy of existing 2DOF is to first design a feedback controller to satisfy the regulation requirements, e.g. internal stability, attenuation of disturbance/noise effects; then design a causal, stable feedforward controller to improve tracking performance by using, for example optimal control techniques. On the contrary in [62], the proposed design method starts with the design of a robust inversion-based feedforward controller which achieves a guaranteed tracking performance for bounded dynamic uncertainties. The bound on the tracking error of the feedforward control is utilized in the H_∞ robust feedback control.

In [66], a 2DOF controller for a piezoelectric tube scanner for high speed force microscopy is designed. The closed-loop operation is performed by H_∞ -controller. The scanner simultaneously tracks the last scan line by a model-based feedforward controller. Experimental results obtained at 15 Hz line-scan rate exhibit a maximum control error reduced by a factor of about 6 in comparison with the commercial one.

In [67], the authors study fundamental trade-offs between positioning resolution, tracking bandwidth, and robustness to modeling uncertainties in 2DOF control designs for nanopositioning systems. They show that the primary role of feedback is providing robustness to the closed loop devices whereas the feedforward component is mainly effective in overcoming fundamental algebraic constraints that limit the feedback-only design. In this paper they present three different designs and compare between them. Experimental results show a significant improvement over optimal feedback-only designs

1.5.3 Integral Control

The main advantage of integral control is that it provides high-gain feedback at low frequencies; therefore, integral controllers can overcome creep and hysteresis effects and lead to precision positioning (since the vibrational dynamics is not dominant at low frequency) [68]. In this sense, traditional PID feedback controllers, or double integral for tracking ramp, are well suited for nanopositioning [51] and are popular in SPM applications [69]. In the existing research, most of the work is focused on modeling the hysteresis using different operators, then using a feedforward compensation to reduce the non-linearity. The role of the PI-controller is to compensate for the remaining inversion error. In [52], pure integral control with time-varying gain is studied, with additional dynamics included in the loop. Only constant inputs are considered. It is shown that the system is well-posed and that, if certain conditions are satisfied, the steady state tracking

error is zero. In [49], the system is assumed to satisfy certain assumptions, which are related to monotonicity and a Preisach model is used. For arbitrary reference signals, the closed-loop system is bounded-input-bounded-output (BIBO) stable with a finite gain of one. It is shown that the absolute value of the error decreases monotonically for a constant reference signal. In this case, provided that the desired output is within the limits of the system output, zero steady state error is guaranteed. A bound on the time required to achieve a specified error is also obtained. The authors claim that the results apply to a wide class of hysteretic systems and only a simple bound on the controller parameter is required. The results show robust position control, even in the presence of model errors. In addition, more details about trajectories of the closed-loop system for a constant input are given. In [50], PID control of a second-order system that include a hysteretic component is studied. Under certain conditions, it is shown that the system asymptotically tracks a constant input. One key assumption in these results is that the system has a monotonic input/output behavior. Other papers presented PID controller as the feedback controller without providing system analysis. In [61], an adaptive control scheme combining neural network with traditional PID controller is proposed to improve the performance of precession mechanism in STMs. Parameters in the PID controller are modified through adjusting the weight values in the neural network with the function of self-learning and adaptability.

PID controller is also used in [53], which is one of the first papers that incorporate a feedforward loop in the system in order to reduce hysteresis effect. The inversion in [53] is inserted at a point different from that of the general scheme. They verify their method through experimental results.

Through this survey of the referenced papers or other existing work, we found, to the best of our knowledge, that there is no analysis that presents an explicit expression of the tracking error. In our work we derive an expression of the tracking error, which can be used to study the interaction

of hysteresis parameters, uncertainties, control gains and frequency, and how they determine the size of the tracking error.

1.6 The Research Objective

Our research focuses on the control analysis and design for linear systems preceded by piecewise linear hysteresis operators. The goal is to achieve the smallest tracking error for the frequency range of interest. We seek explicit expressions of the inversion error and use them to design and compare different robust control methods and to use bounds on the inversion error to derive expressions for the tracking errors.

1.7 Research Overview

This research focuses on control of systems that include hysteresis in cascade with linear dynamics. Specifically, it deals with control schemes in which an inverse-operator precedes the hysteresis. This brings two important issues, which this research addresses. First, what is the size of the inversion error when uncertainties of the hysteresis model is considered. Second, how to use the bound on this inversion error to design a controller that can reduce the tracking error.

The importance of this topic comes from two factors; First, hysteresis non-linearity appears in a wide range of applications including most of smart material applications such as piezoelectric actuators. Second, existing results for finding analytical bounds on the inversion error and the use of such bounds in the control design are not available. In most cases, they are choosing these bounds by tuning them in simulations or experiments.

An important assumption in our work is that the hysteresis loop has piecewise linear segments.

This assumption is justified because many hysteresis models have this property. With that, we derive analytical expressions of the bound on the inversion errors in the presence of model uncertainties. Two cases are considered, depending on the parameters we use to represent the hysteresis model. In one method we deal with the PI operator and use the thresholds and the weights of the play operators to determine the bound. In the other method we use the slopes and intercepts of the hysteresis loop segments. We then consider using these bounds in the analysis and design of different robust control methods.

We are interested in three classes of robust controllers. First, The commercial Proportional-Integral controller. Although, this controller is a tuning controller it provides good experimental results. Our work shows that when the linear dynamics are fast and we add a feedforward control to the system, it results in a very good tracking performance. The analysis of the tracking performance provides us with explicit solutions of differential equations. In these expressions, we can determine the effect of different components such as parameter uncertainties, operator parameters, frequency, and control gains on the tracking performance. Second, we explore Sliding Mode Control (SMC) as one of the major methods in robust nonlinear control. We compare the results when we use the bounds obtained from the threshold-weights method and slope-intercept method in feedback design by simulations and experiments. Third, we consider H_∞ linear control. We compare using H_∞ control when the inverse operator is not used as the size of the uncertainty is larger than when the inverse operator is used. We also compare the H_∞ -controller with conventional Proportional-Integral controller.

From these comparisons between different methods using analytical analysis, simulations and experiments we arrived at some interesting results. First the inversion bounds are less conservative when we used the slope-intercept method. This was important for the SMC design. Having large bounds lead to the requirement of large control signals which are usually limited in real ap-

plications and also it reduces the possible positioning range. In sliding-mode control we found analytically and also by the simulation that by increasing the frequency the tracking error has the following behavior. It increases at very low frequency, which is usually the operation range that most of current positioners use, then it almost stays constant, then it starts to decrease at the range which is close to resonance frequency and finally it increases again. This behavior differs from the Proportional-integral controller in the third stage where we did not see the decreasing in the tracking error. In the experiment, we only examined a low frequency range for the safety of the piezo-actuator where we found that the tracking error has qualitatively similar behavior to the simulation. We also included a rate limiter in the experiment which affects the frequency response and adds more error, particularly, when we increased the frequency. For the H_∞ control, we found that it has a better performance when the inverse operator was included. We also found that it outperformed the PI controller for a moderate range of frequency, but it did worse at very low and high frequency. That range can be chosen by designer which depends also on the plant dynamics.

1.8 Dissertation Layout

The remainder of this dissertation is organized as follows. In Chapter 2, we derive bounds on the inversion error using two methods and compare them. We call the first one the slope-intercept method, and the other the weight-threshold method. In Chapter 3, we describe a PI control scheme. We use the analysis of the inversion error based on the slope-intercept method to quantify the tracking of the closed-loop system when a Proportional-Integral PI controller is used. Separation of the controller variables from the plant variables is accomplished by using singular perturbations techniques. The development of the solution around one hysteresis loop in the presence of a periodic input is obtained. The interaction between different components and their effects on the

solutions are discussed. We explore how to use the inversion bounds to design more sophisticated nonlinear controllers in Chapter 4, where sliding-mode-control (SMC) is considered. Stability analysis and tracking performance are also presented. Chapter 5 presents a linear robust method which considers the plant dynamics in the design. This method relies on H_∞ optimal control design. We provide simulation comparisons for the three method in Chapter 5. In Chapter 6, conclusions are drawn on the research and recommendations are proposed for future work.

Chapter 2

Hysteresis Model and Inversion Error

2.1 Introduction

This chapter is divided into two parts. In the first part, we discuss how to derive bounds on the inversion error. We will present two different methods and show how they relate to each other. These bounds will be used in the following chapters in design and analysis of different feedback control methods. In the second part of this chapter, we will examine these bounds by running simulations for open-loop system. First, we will measure the hysteresis loops of the PI model and compare it with real hysteresis, which has been obtained from experimental data. Then we will perturb the model and measure the size of the inversion error. We will compare this error with model error. Then we compare the inversion errors with analytical bounds, which are derived in the first part.

2.2 Characterization of the inversion error

We calculate a bound on the inversion error using two methods. In the first, we assume that the hysteresis nonlinearity has piecewise linear characteristics; in other words, all hysteresis loops (major loops and minor loops) consist of linear segments, where each segment s_i has a slope m_i and an intercept γ_i with the output axis, and $i = 1, 2, \dots, l$, where l is the number of segments.

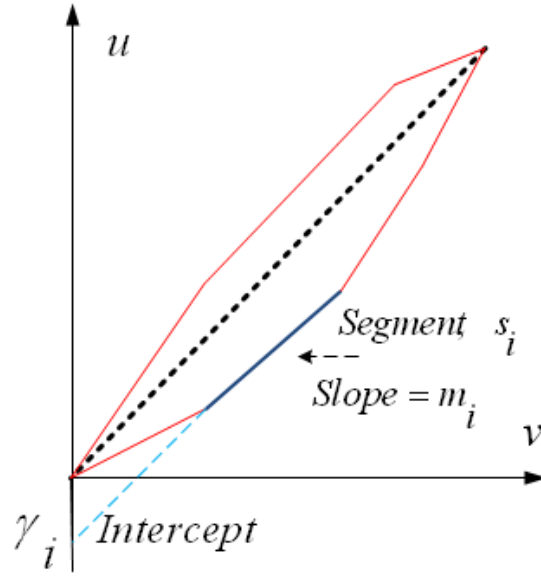


Figure 2.1: Illustration of a hysteresis loop with piecewise linear characteristics.

See Fig. 2.1 for illustration. The bound on the inversion error is calculated using the slopes and intercepts of linear segments. We refer to this method as the *slope-intercept* method. Note that this method is not confined to the PI operator; indeed, it applies to wide class of models used in the literature, including the piecewise linear model adopted in [36], the Prandtl-Ishlinskii (PI) operator [21, 15], the modified PI operator [12], and the Krasnoselskii-Porkovskii (KP) operator [70] among others. The second method applies only to PI operator and the bound is derived from weights of the play operators with different thresholds. We refer to it as *weight-threshold* method. We will also compare between these two methods for the PI operator.

Fig. 2.2 illustrates the system with a feedforward inverse hysteresis compensator. We assume that the actual hysteresis is represented by an operator Γ_p , defined by a vector of play thresholds and a vector of play weights w^* . We further assume that a nominal model Γ_m for the hysteresis is identified for implementation of Γ_m^{-1} , an approximate inverse to Γ_p . It is assumed that Γ_m shares the same set of play thresholds with Γ_p , but its weight vector w differs from that of Γ_p ,

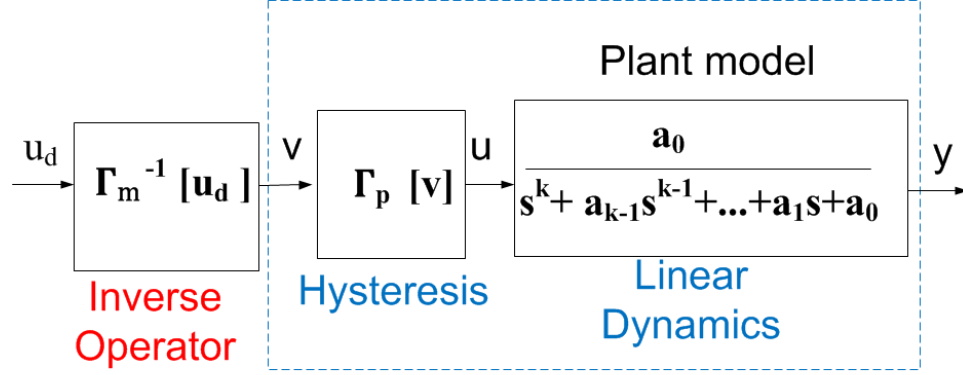


Figure 2.2: A system with hysteresis preceded by an inverse operator.

which represents the source of model uncertainty. In particular, we write $w^* = w + \Delta_w$, with Δ_w denoting the weight perturbation. The control u_d is applied to the inverse model and $d = u_d - u$ is the inversion error.

2.3 The Inversion Error Bound Using the Slope-Intercept

Method

In this method, the uncertainty in the weight vector is translated into uncertainties in the slope and intercept of each segment j of the hysteresis loop, denoted as Δm_j and $\Delta \gamma_j$, and $j = 1, 2, \dots, l$, where l is the number of segments. Let the input-output relationship for the operator be

$$u = m_j v + \gamma_j \quad (2.1)$$

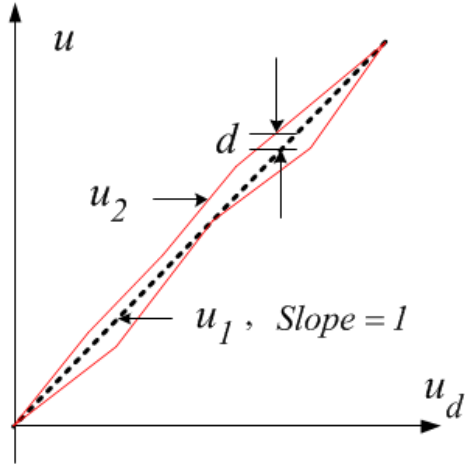


Figure 2.3: Inversion error bounds using slop-intercept method.

and the input-output relationship for the inverse-operator be

$$v = \frac{1}{m_j} u_d + \gamma_{inv,j} \quad (2.2)$$

By inserting (2.2) into (2.1) we obtain

$$\begin{aligned} u &= m_j \left(\frac{1}{m_j} u_d + \gamma_{inv,j} \right) + \gamma_j \\ &= u_d + m_j \gamma_{inv,j} + \gamma_j \end{aligned} \quad (2.3)$$

Hence, for perfect inversion we require

$$m_j \gamma_{inv,j} + \gamma_j = 0 \quad (2.4)$$

Fig. 2.3 illustrates how these uncertainties can be used to determine an upper-bound on the inversion error. The term u_1 represents the output u when the inversion is perfect, and its slope is

one, while u_2 represents the output in the presence of uncertainties,

$$u_1(t) = u_d(t) \quad (2.5)$$

$$u_2(t) = \left(1 + \frac{\Delta m_j}{m_j}\right) u_d(t) + \Delta_{dc,j} \quad (2.6)$$

where $\Delta_{dc,j}$ can be obtained from (2.4) by including the uncertainties as

$$\begin{aligned} \Delta_{dc,j} &= \Delta m_j \gamma_{inv,j} + \Delta \gamma_j \\ &= \frac{\Delta m_j \gamma_j - m_j \Delta \gamma_j}{m_j} \end{aligned} \quad (2.7)$$

The difference between u_2 and u_1 represents the size of the uncertainty and is denoted by $d(t)$:

$$\begin{aligned} d(t) &= u_2(t) - u_1(t) \\ &= \left(1 + \frac{\Delta m_j}{m_j}\right) u_d(t) + \Delta_{dc,j} - u_d(t) \end{aligned} \quad (2.8)$$

The upper bound for each segment is

$$|\Delta_{dc,max}| \leq |\Delta \gamma,max| + \frac{|\gamma_{max}| |\Delta m,max|}{m_{min}} \quad (2.9)$$

The upper bound for all segments is

$$|d(t)| \leq \left| \frac{\Delta m_{max}}{m_{min}} \right| |u_d(t)| + |\Delta_{dc,max}| \quad (2.10)$$

where m_{min} is the smallest slope, $|\Delta m_{max}|$ is the largest slope uncertainty, and $|\Delta_{dc,max}|$ is the largest intercept uncertainty among segments and can be obtained from (2.7) as

$$\Delta_{dc,max} \leq \frac{|\Delta m_{max} \gamma_{max}| + |m_{max} \Delta \gamma_{max}|}{m_{min}} \quad (2.11)$$

A bound on the inversion error can be obtained from (2.10) as

$$|d| \leq k_1 + k_0 |u_d| \quad (2.12)$$

where $\frac{|\Delta m_{max}|}{|m_{min}|} \leq k_0$ and $|\Delta_{dc,max}| \leq k_1$.

2.4 The Inversion Error Bound Using the Weight-Threshold

Method

Since the hysteresis operator is modeled by PI operator for simulation and experimental purposes, it is natural to derive bounds using its immediate parameters, which are thresholds and weights of the play operators. Fig. 2.4 illustrates the basic behavior of a play operator. The output of a PI operator can be represented as [12]

$$\Gamma[v] = w^T H_r[v; z_0](t) \quad (2.13)$$

where, $H_r = [H_{r0} H_{r1} \dots H_{rn-1}]^T$ is the vector of individual play operators,

$w^T = [w_0 w_1 \dots w_{n-1}] \geq 0$ is the vector of weights for individual play operators,

$r^T = [r_0 r_1 \dots r_{n-1}]$ denotes the vector of play thresholds, and we have n play operators. It is assumed that $0 = r_0 < r_1 < \dots < r_{n-1} = r_{max}$, where r_{max} denotes the largest threshold, and

$w_0 > 0$. A play operator with threshold r_i , and initial condition z_{0i} is defined by

$$H_{r_i}[v, z_0] = \max\{v - r_i, \min\{v + r_i, z_{0i}\}\} \quad (2.14)$$

where $i = 0, 1, \dots, n - 1$. To simplify the notation, we will not explicitly put the initial condition for operators H_{r_i} , Γ_m , etc.

$$u = \Gamma_p[v] = w^{*T} H_r[v] \quad (2.15)$$

$$v = \Gamma_m^{-1}[u_d] \quad (2.16)$$

Eq. (2.16) implies

$$u_d = \Gamma_m[v] = w^T H_r[v] \quad (2.17)$$

$$d = u_d - u = \Gamma_m[v] - \Gamma_p[v] = \Delta_w^T H_r[v] \quad (2.18)$$

Hence,

$$|d| = \left| \Delta_w^T H_r[v] \right| \quad (2.19)$$

From Fig. 2.4, it can be readily verified that, for a play operator with threshold r_i ,

$$|H_{r_i}[v](t) - v(t)| \leq r_i \quad (2.20)$$

which implies

$$|H_{r_i}[v](t)| \leq |v(t)| + r_{max} \quad (2.21)$$

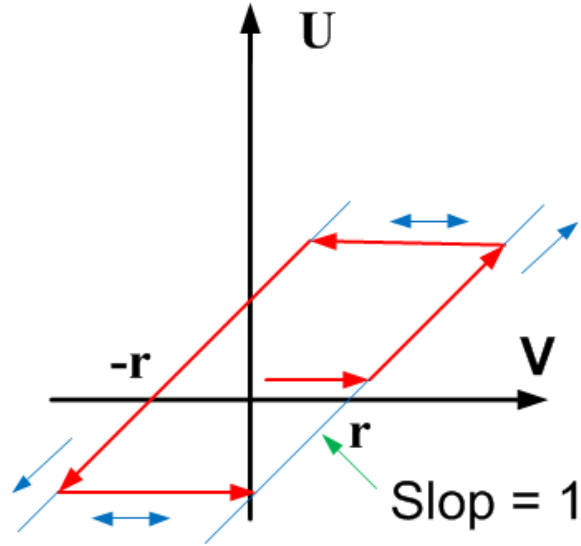


Figure 2.4: A play operator: the building block of a PI operator.

for $i = 0, \dots, n - 1$. We assume that the maximum error in the vector Δ_w is given by $\Delta_{w,max}$.

Combining (2.19) and (2.21), we obtain

$$|d| \leq n\Delta_{w,max} (|v| + r_{max}) \quad (2.22)$$

We are interested in deriving a bound for $|d|$ in terms of u_d . Recall that v is related to u_d through the inversion operator Γ_m^{-1} . The inverse operator can be represented with yet another PI operator Γ_{inv} [12]. Γ_{inv} has n play operators, and its vector of thresholds $r_{inv} = [r_{inv,0}, \dots, r_{inv,n-1}]^T$ and vector of weights $w_{inv} = [w_{inv,0}, \dots, w_{inv,n-1}]^T$ can be computed based on the parameters of the forward hysteresis model Γ_m . Therefore, we can write

$$v = w_{inv}^T H r_{inv} [u_d] \quad (2.23)$$

From (2.23), we have

$$|v(t)| \leq \sum_{i=0}^{n-1} |w_{inv,i}| (|u_d(t)| + r_{inv,max}) \quad (2.24)$$

where $r_{inv,max} = r_{inv,n-1}$ is the maximum threshold among the play operators for the inverse hysteresis operator Γ_{inv} . Combining (2.22) and (2.24), we have

$$\begin{aligned} |d(t)| &\leq n|\Delta_{w,max}| \sum_{i=0}^{n-1} |w_{inv,i}| |u_d(t)| \\ &\quad + n|\Delta_{w,max}| (r_{max} + \sum_{i=0}^{n-1} |w_{inv,i}| r_{inv,max}) \end{aligned} \quad (2.25)$$

Hence,

$$|d| \leq k_1 + k_0 |u_d| \quad (2.26)$$

where, $k_0 = n|\Delta_{w,max}| (\sum_{i=0}^{n-1} |w_{inv,i}|)$ and $k_1 = n|\Delta_{w,max}| (r_{max} + \sum_{i=0}^{n-1} |w_{inv,i}| r_{inv,max})$. Note that the evaluation of k_0 and k_1 requires knowing the maximum weight error $\Delta_{w,max}$ for the forward hysteresis model and the vector of weights w_{inv} for the inverse hysteresis model. The analysis in the following chapters requires the assumption $0 < k_0 < 1$, which holds true when $\Delta_{w,max}$ is sufficiently small. Also, note that the expressions of k_0 and k_1 are different from the one obtained from Eq. (2.12).

2.5 The Relationship Between Segment Slope and Operator

Weights

The hysteresis characteristics of a PI operator can be determined by the so-called initial loading curve (or the generating function). This curve is traversed if the initial state of the PI hysteresis operator is zero and a monotone increasing input signal is applied [12]. The initial loading curve can be fully characterized by a threshold-dependent piecewise linear function $\Phi(r) = \sum_{j=0}^i w_j(r - r_j)$, where $i = 0, \dots, n-1$ and $r_i \leq r < r_{i+1}$. The inverse of the initial loading curve $\Phi(r)$, denoted as $\Phi_{inv}(r_{inv})$, exists uniquely for $r_{inv} \geq 0$ and can be regarded as a generating function for the inverse operator, $\Phi_{inv}(r_{inv}) = \sum_{j=0}^i w_{inv,j}(r_{inv} - r_{inv,j})$, where $r_{inv,i} \leq r < r_{inv,i+1}$. The slopes can be calculated from the derivative of these generating functions to obtain

$$\frac{d}{dr}\Phi(r) = \sum_{j=0}^i w_j = m_i \quad (2.27)$$

$$\frac{d}{dr_{inv}}\Phi_{inv}(r_{inv}) = \sum_{j=0}^i w_{inv,j} = m_{inv,i} \quad (2.28)$$

The transformation law for weights results from $\frac{d}{dr_{inv,i}}\Phi_{inv}(r_{inv,i}) = 1/\frac{d}{dr}\Phi(r_i)$. After simplifying this expression, the weights of the inverse operator can be calculated as

$$w_{inv,0} = \frac{1}{w_0}$$

$$w_{inv,i} = \frac{-w_i}{(w_0 + \sum_{j=1}^i w_j)(w_0 + \sum_{j=1}^{i-1} w_j)} \quad (2.29)$$

where $i = 1 \cdots n - 1$. Hence combining the effect of the inverse operator with slope $m_{inv,i} = \frac{1}{w_0 + w_1 + \cdots + w_i}$ and that of the operator with slope $m_i = w_0 + w_1 + \cdots + w_i$ would result in an identity operator with slope of 1. See Fig 2.6. To examine how a perturbation of operator weights affects the signal passing through the cascaded operators, let us assume that the uncertainties on each weight w_i is Δ_{w_i} . The perturbed slope is

$$m_i + \Delta_{m,i} = w_0 + \Delta_{w_0} + w_1 + \Delta_{w_1} + \cdots + w_i + \Delta_{w_i} \quad (2.30)$$

From (2.27) and (2.30) we can obtain $\Delta_{m,i} = \Delta_{w_0} + \Delta_{w_1} + \cdots + \Delta_{w_i}$. It is obvious that the uncertainties accumulate and the maximum error will be in the last segment (with $l = n - 1$) which is $\Delta_{m,l} = \Delta_{w_0} + \Delta_{w_1} + \cdots + \Delta_{w_{n-1}}$. Because the uncertainties are increasing as the signal increases and crosses the hysteresis segments, we cannot rely on the weight perturbation in obtaining a non-conservative estimate of the uncertainty in the slopes. We also can show that the slope-intercept approach has less conservative inversion error than the weight-threshold method by comparing (2.25) and (2.10). To compare the inversion error portion due to uncertainties in the slopes, the first term in (2.25) and that in (2.10) are compared. We express the slopes of the first term of (2.10) in terms of the weights of the play operators

$$\begin{aligned} \left| \frac{\Delta m_i}{m_i} \right| |u_d(t)| &\leq \left| \frac{\Delta_{w_0} + \Delta_{w_1} + \cdots + \Delta_{w_{n-1}}}{w_0} \right| |u_d| \\ &\leq \frac{n |\Delta_{w,max}|}{|w_0|} |u_d| \end{aligned} \quad (2.31)$$

We know that from (2.29) the inverse operator weights $w_{inv,i}$ are negative quantities except $w_{inv,0}$. As a result, their summation $\sum_{i=0}^{n-1} w_{inv,i}$ is smaller than $\frac{1}{w_0}$. But, because we use the triangular inequality to obtain (2.25) and we sum the absolute values of $|w_{inv,i}|$, this results in a larger bound

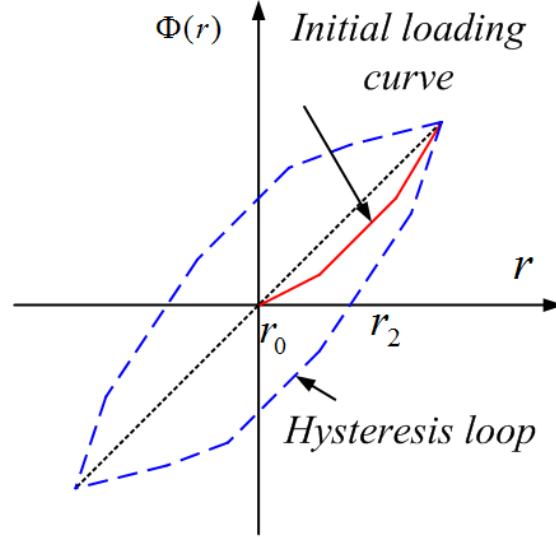


Figure 2.5: Illustration of the initial loading curve.

($\sum_{i=0}^{n-1} |w_{inv,i}| > \frac{1}{|w_0|} > \sum_{i=0}^{n-1} w_{inv,i}$). Then by comparing the bound on the first term in (2.25) with (2.31) we find

$$\frac{n|\Delta_{w,max}|}{|w_0|} |u_d| < n|\Delta_{w,max}| \left(\sum_{i=0}^{n-1} |w_{inv,i}| \right) |u_d(t)| \quad (2.32)$$

From (2.32), we can see that the bound on the error using the intercept-slope approach is less conservative than the bound which is obtained from the weight-threshold approach. Similarly, we can derive the relationship between segment intercepts and operators weights and thresholds.

2.6 The Relationship Between Segment Intercept and Operator Weights

The intercept of the segment with the y-axis can be calculated from the weighted superposition of play operators as follows. For the hysteresis operator $\gamma = \sum_{i \in A} w_i r_i$, and for the inverse-operator

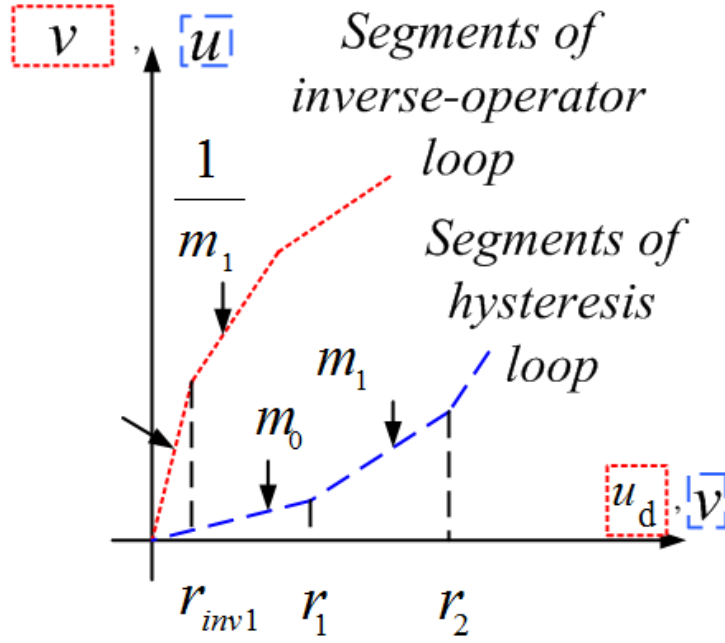


Figure 2.6: Ascending branches of hysteresis operator and inverse-operator.

$\gamma_{inv} = \sum_{i \in A} w_{inv,i} r_{inv,i}$, where A is the set of plays that are active. Note that the operator becomes active when the input signal is large enough to pass from playing region to linear region of the play operator.

When the weight vector is perturbed by Δw the slopes are perturbed by Δm and Eq. (2.4) becomes

$$\Delta m \gamma_{inv} + \Delta \gamma = \Delta dc \quad (2.33)$$

Then by expressing m , Δm , γ_{inv} , and γ_{per} in (2.33) in terms of w and Δw we get

$$\Delta dc,i = \left(\sum_{i \in A} \Delta w,i \right) \left(\sum_{i \in A} w_{inv,i} r_{inv,i} \right) + \sum_{i \in A} \Delta w,i r_i \quad (2.34)$$

An upper bound for the i th segment is obtained by taking the absolute value as

$$|\Delta_{dc,i}| \leq \left| \left(\sum_{i \in A} \Delta_{w,i} \right) \right| \left(\left| \left(\sum_{i \in A} w_{inv,i} r_{inv,i} \right) \right| + |r_i| \right) \quad (2.35)$$

The worst case happens when all plays are active (i.e. $\gamma = \sum_{i=0}^{n-1} w_i r_i$) because the terms will have the same sign. The bound on all segments then is obtained by

$$|\Delta_{dc,max}| \leq n |\Delta_{w,max}| \left(\left| \left(\sum_{i=0}^{n-1} w_{inv,i} r_{inv,i} \right) \right| + |r_{max}| \right) \quad (2.36)$$

By comparing this equation with what obtained from weight-threshold method which is given in (2.25), we can see that they differ in the term $\sum_{i=0}^{n-1} |w_{inv,i}| r_{inv,max}$, where taking absolute value before summing the terms makes this bound very conservative in (2.25).

Based on these different bounds on the inversion error, we propose to design robust controllers of two general classes and examine how useful are these bounds in control design. The first class is nonlinear robust control. This class has three different methods; Sliding-Mode-Control (SMC), Lyapunov re-design, and high-gain feedback control. SMC and Lyapunov redesign are close in dealing with uncertainty. The only difference is which we design first; the sliding-surface or the Lyapunov function. The high-gain method is basically included in the previous two methods when trajectories enter the boundary layer of the surface. Thus, we only focus on SMC method to describe the first class. The other class of controllers with which we examine these bounds is robust linear-control. We assume that the hysteresis precedes the linear dynamics of the plant. The system fits in linear design as the remaining non-linearity after inversion is treated as uncertainty. Since the reference signals that we often use are periodic, the H_∞ control is a good candidate for designing a robust controller for these systems. Proportional-Integral control is another simple robust control

method which is used particularly when the application requires low operating speed.

2.7 Simulation of the Hysteresis Loops Based on the Experimental Data

To examine the proposed control methods in improving the system performance when it involves hysteresis, we use a piezo-actuator nanopositioner. The commercial nanopositioner (Nano-OP65) and its power drive, shown in Fig. 2.7, are supplied by Mad City Labs Inc. We first identify the positioner characteristics to determine its linear dynamics and hysteresis characteristics. The hysteresis was experimentally characterized by applying a quasi-static input that sweeps the positioner over its operational range. The measured Hysteresis loops are shown in Fig. 2.8. Then the hysteresis is modeled with a PI-operator with 5 play operators with thresholds $r = [0, 0.63, 1.27, 2.54, 4.45]^T$ and the vector of weights is $w = [5.88, 1.58, 0.47, 0.98, 0.4]^T$. The major loop of the output of the model using the same input data which is used in characterizing the hysteresis is shown in Fig. 2.9. The error between the Model output and the actual hysteresis output is illustrated in Fig. 2.10 for a decreasing sinusoidal input. Then, we calculated the inverse-operator, which has almost zero-inversion error ($\times 10^{-14} \mu\text{m}$) when it is cascaded with the modeled hysteresis (the hysteresis operator). Note that because of the modeling error, the cascading of the inverse-operator with the actual nanopositioner hysteresis would result in an inversion error. Hence, for all of simulations in next chapters we will perturb the model such that it results in an error close to the one comes from cascading the inverse-operator with the actual positioner hysteresis. Each component on the weight vector is perturbed by a maximum value of $\Delta_{w,max} = 0.15$. Fig. 2.11 shows the error results from cascading the inverse-operator with the

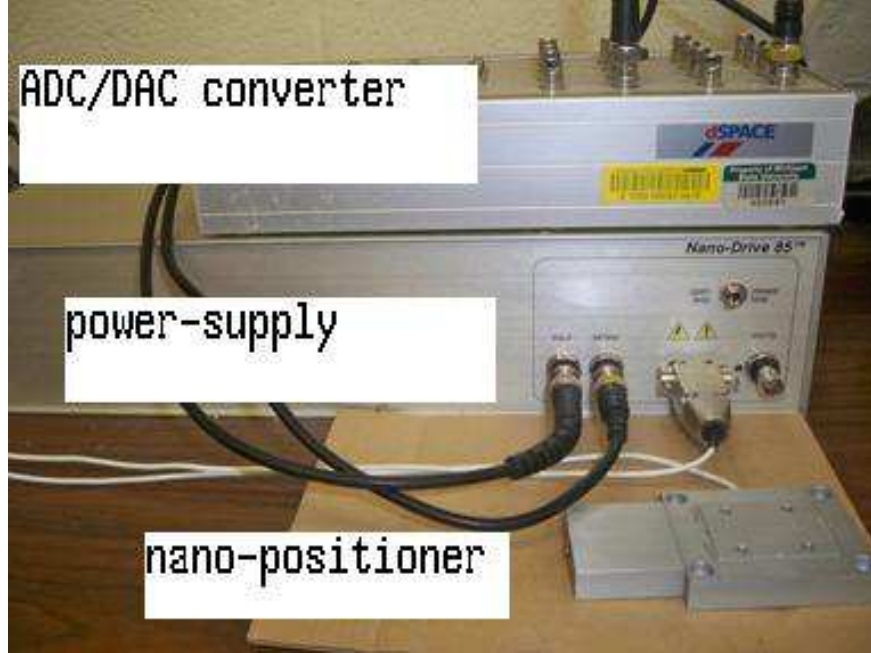


Figure 2.7: Experimental setup includes the nanopositioner Nano-OP65, power drive, and ADC/DAC converter.

perturbed hysteresis operator. This error has a size close to the one obtained in Fig. 2.10.

2.8 Example of Calculating Bounds on the Inversion Error

We consider, in this example, a PI operator composed of the superposition of weighed play operators of slopes equal to one. Hence the slope of any segment is calculated by the summation of the weights of play operators which are acting in their linear region at that segment. Let us denote the set of operators which act in their linear region by A_j . Then the slope m_j is given by $m_j = \sum_{A_j} w_j$ and the upper bound on the play operator is given from (2.21) by $|H_{r_j}[v](t)| \leq |v(t)| + r_{max}$. A bound on the segment j output can be expressed using the weighted superposition of the active operators between thresholds r_j and r_{j+1} as

$$|u| = \sum_{A_j} w_j |H_{r_j}[v](t)| \leq \sum_{A_j} w_j (|v(t)| + r_{max}) \quad (2.37)$$

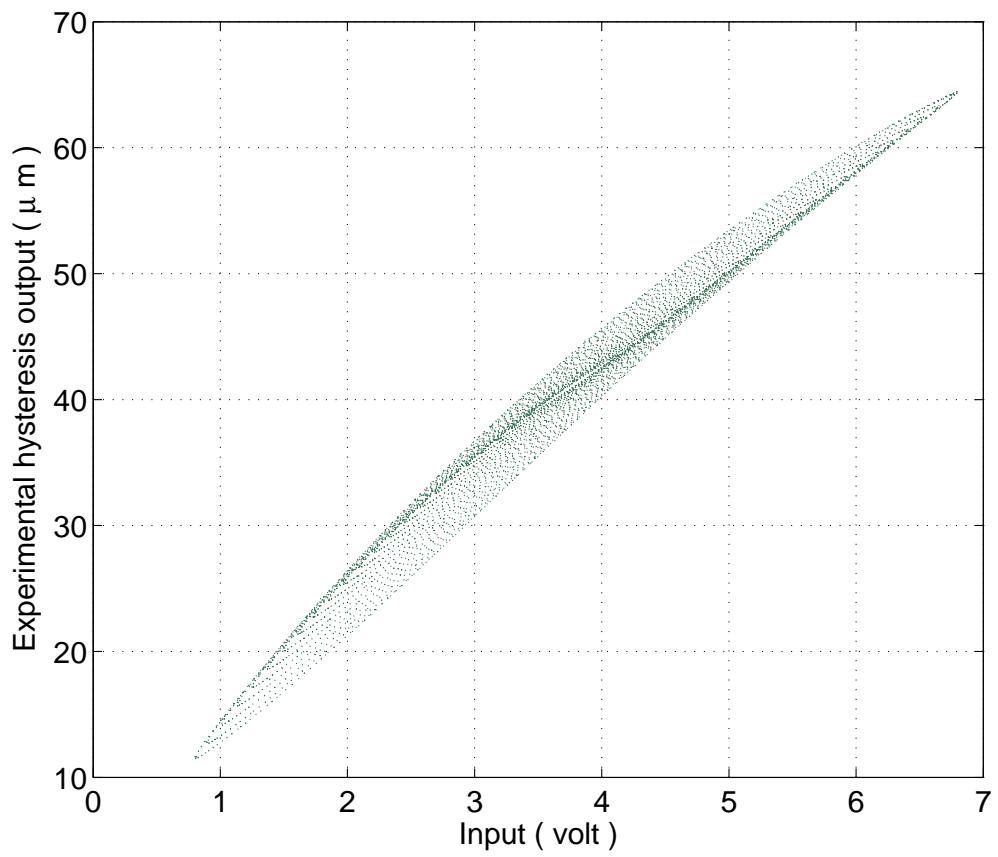


Figure 2.8: Measured hysteresis loops.

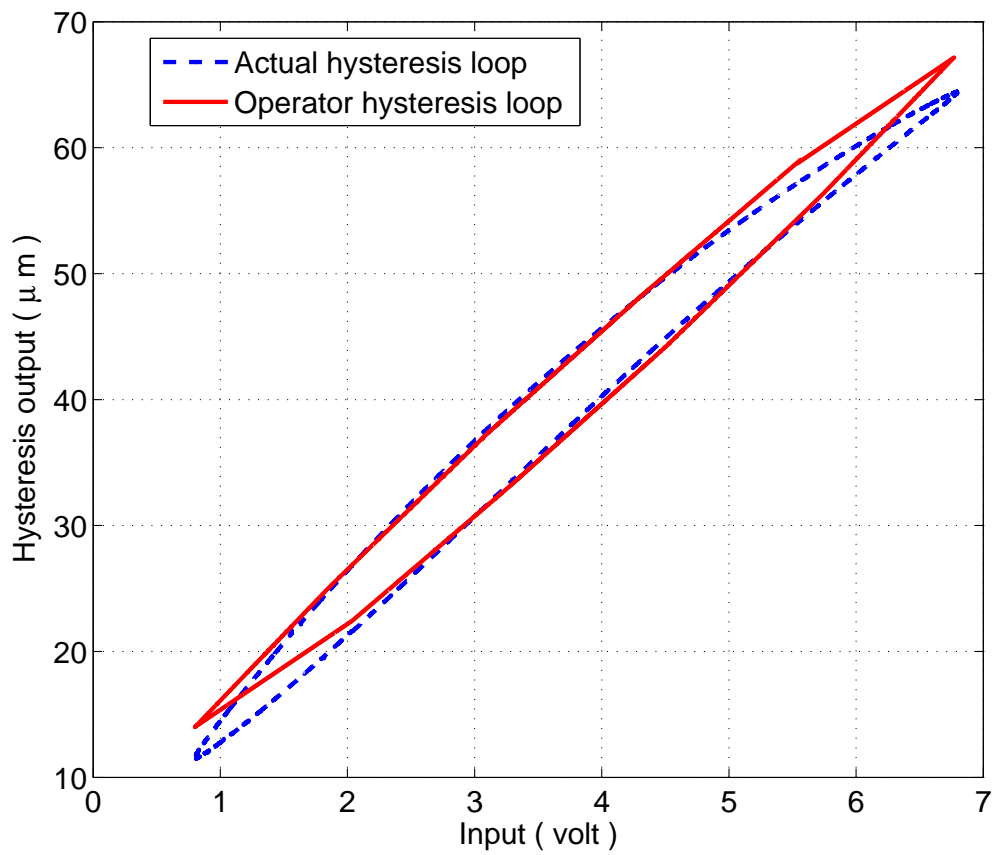


Figure 2.9: Comparison between the measured hysteresis loop and the operator hysteresis loop.

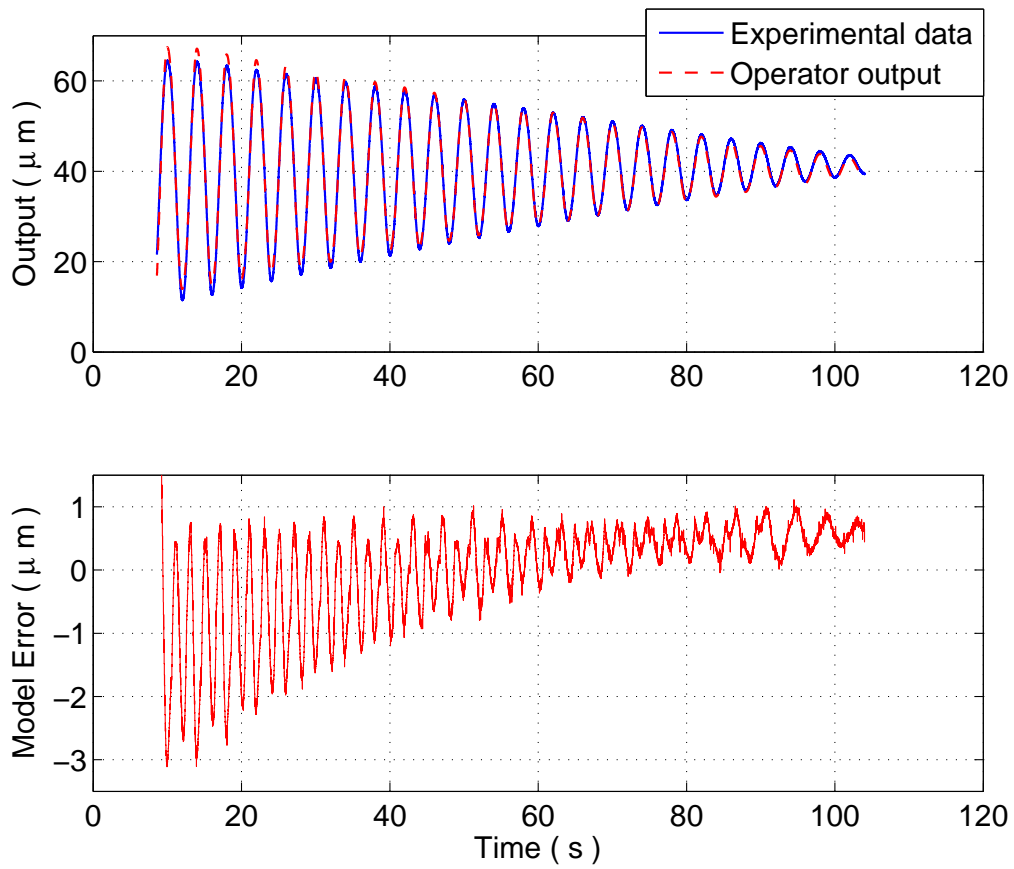


Figure 2.10: Positioner output used in the PI identification and the resulting model output.

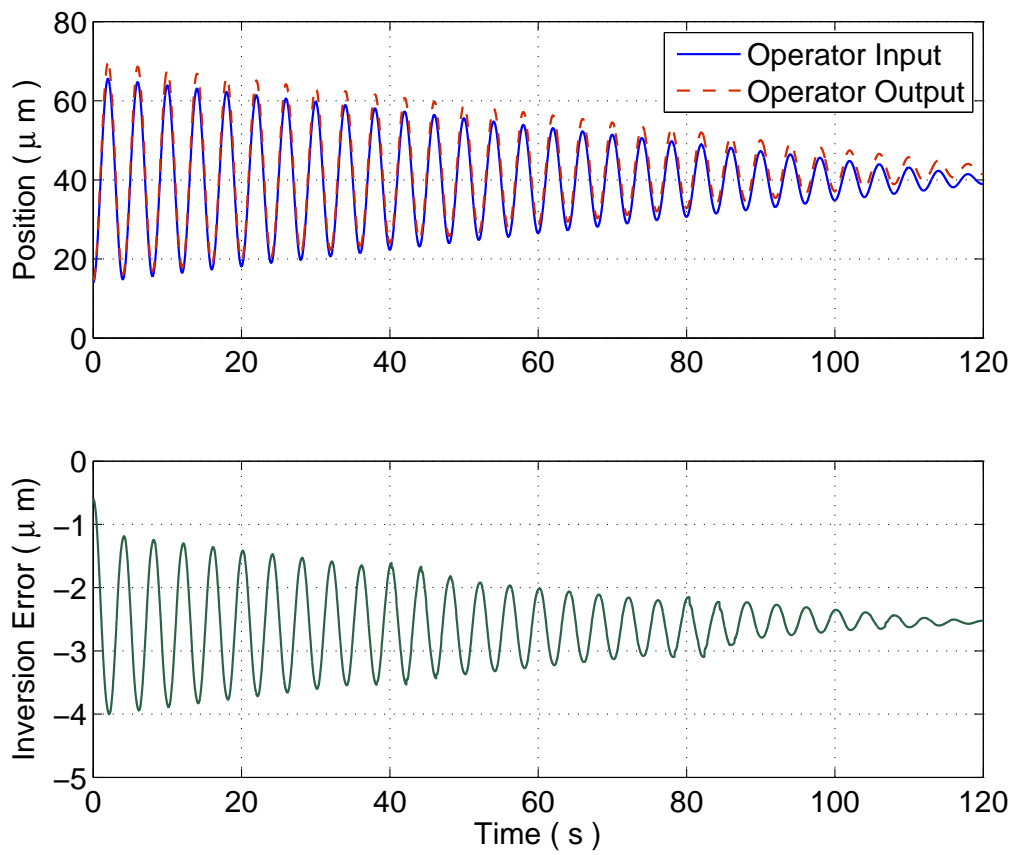


Figure 2.11: The output and inversion error of a perturbed PI operator.

Then, we insert u from (2.1) into (2.37)

$$|m_j v(t) + \gamma_j| \leq \sum_{A_j} w_j (|v(t)| + r_{max}) \quad (2.38)$$

By setting $v = 0$ in (2.38), the intercepts satisfy the inequality

$$|\gamma_j| \leq \sum_{A_j} w_j r_{max} \quad (2.39)$$

The upper bound of slopes and intercepts for all segments can be obtained from (2.27) and (2.39), respectively, as $m_{max} = \sum_{j=0}^{n-1} w_j$ and $|\gamma_{max}| \leq \sum_{j=0}^{n-1} w_j r_{max}$, where n is the number of play operators.

To examine how a perturbation of operator weights affects the signal passing through the cascaded operators, let us assume that the uncertainties on each weight w_j is Δ_{w_j} . The perturbed slope is

$$m_j + \Delta_{m,j} = \sum_{A_j} (w_j + \Delta_{w_j}) \quad (2.40)$$

From (2.27) and (2.40) we can obtain $\Delta_{m,j} = \sum_{A_j} \Delta_{w_j}$. Hence, the upper bound on slope uncertainties of all segment is $|\Delta_{m,max}| \leq n |\Delta_{w,max}|$. Similarly, the upper bound of the intercept uncertainties for all segments can be obtained as $|\Delta_{\gamma,max}| \leq n |\Delta_{w,max}| r_{max}$.

In this example, we want to examine the bounds calculated on the inversion error versus the inversion error results from perturbing the operator. First, the perturbation on the hysteresis loop is illustrated in Fig. 2.12 for a sinusoidal input with a range of $50 \mu\text{m}$. Note that we apply a voltage to the hysteresis input with a maximum of 5.7 volt, but we scaled the input in Fig. 2.12 to represent

it in the corresponding positioning range in μm . We also shifted the hysteresis loops to the first input-output quadrant by biasing the input with $25 \mu\text{m}$ dc input. Each component on the weight vector is perturbed by a maximum value of $\Delta_{w,max} = 0.15$. This results in an uncertainty on the slopes and the intercepts of each segment. It is easy to calculate these uncertainties by determining the slopes and intercepts of each segment for the perturbed and non-perturbed operator and then subtract them. We obtained the following values. $m_{min} = 0.7$, $m_{max} = 1.1$, $|\Delta_{m,min}| = 0.016$, $|\Delta_{m,max}| = 0.08$, $|\gamma_{max} = 16|$, and $|\Delta\gamma_{max}| = 1.03$.

Now to calculate the bounds on the inversion error for the slope-intercept method, we have $\frac{|\Delta m_{max}|}{|m_{min}|} \leq k_0$ and $|\Delta_{dc,max}| \leq k_1$, where $|\Delta_{dc,max}|$ can be calculated from (2.11). We obtain $k_0 = 0.12$ and $k_1 = 8.9$. Then the bound is calculated from (2.12) with $|u_d|_{max} = 50$, we get $|d| \leq 8.1$.

For the weight-threshold method, the bounds are calculated from the expressions;

$k_0 = n|\Delta_{w,max}|(\sum_{i=0}^{n-1} |w_{inv,i}|)$ and $k_1 = n|\Delta_{w,max}|(r_{max} + \sum_{i=0}^{n-1} |w_{inv,i}|r_{inv,max})$. We obtain $k_0 = 0.1282$ and $k_1 = 10.53$. Similarly, we insert these values in (2.26) to obtain the bound $d \leq 17$.

We can see this bound is more conservative than the one obtained by slope-intercept method. Next, we apply the same input, $u_d = 25 \times 10^{-6}(1 + \sin\omega t)$, to the cascaded inverse-operator with perturbed operator to obtain the inversion error shown in Fig. 2.13, where we can see that maximum absolute value of the error is $|e|_{max} = 3.7\mu\text{m}$. This value is smaller than the two bounds, which are calculated using both methods with a large safe margin.

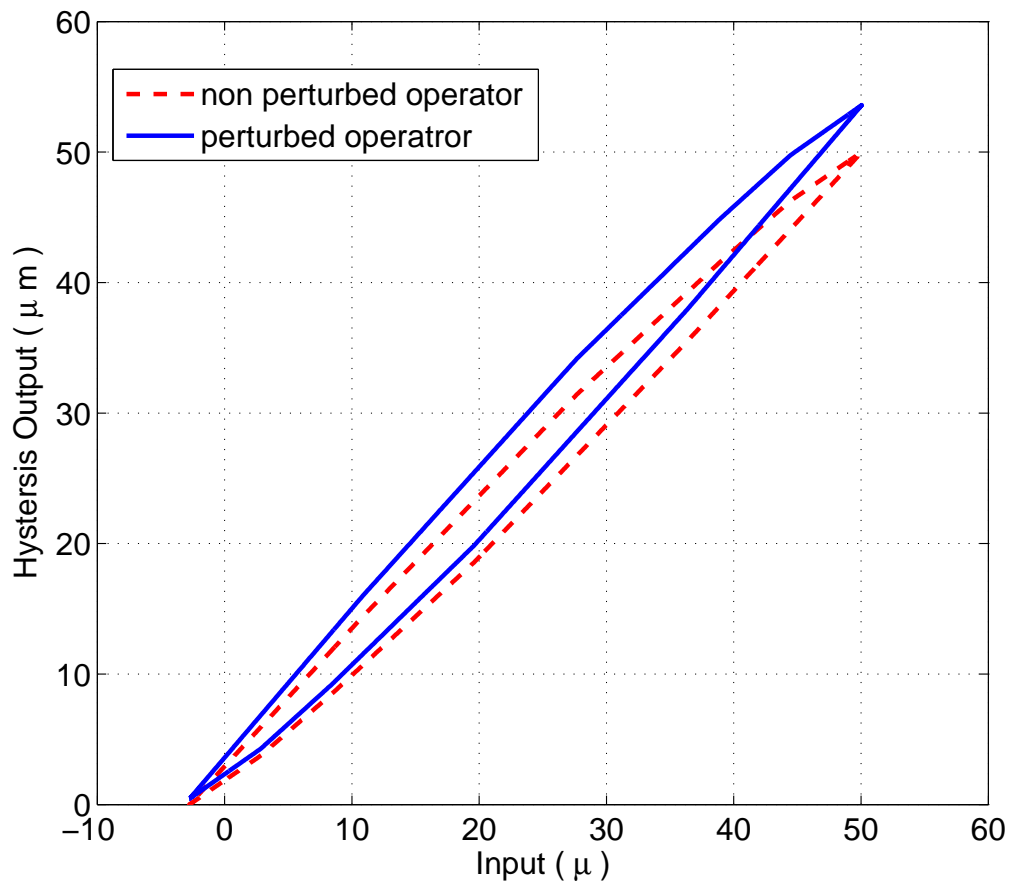


Figure 2.12: Hysteresis loops for a non-perturbed and a perturbed PI operator with a perturbation $\Delta_{w,max} = 0.15$.

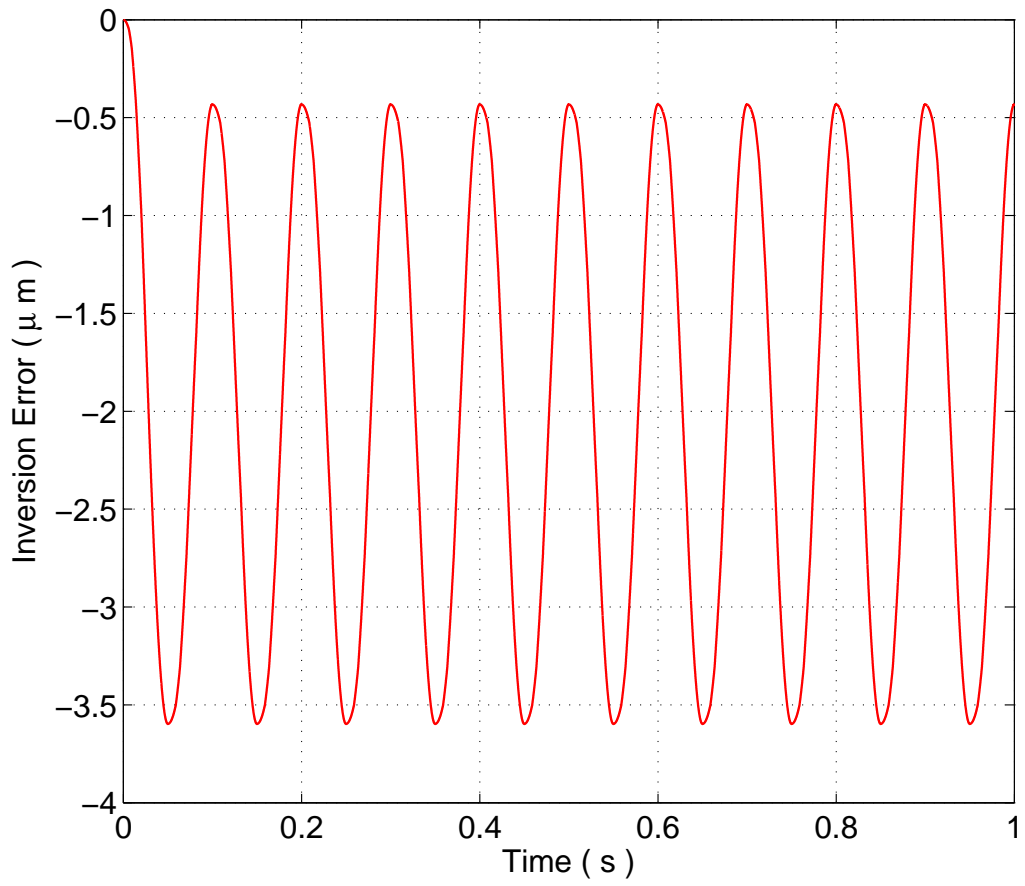


Figure 2.13: The inversion error of a perturbed PI operator with a $50 \mu\text{m}$ input.

2.9 Summary

In this chapter, we introduced two methods to characterize the inversion error when the hysteresis model has some uncertainty. The error is characterized by a perturbation in the weight vector of the PI operator which is used to implement the inverse-operator. A more general way which includes more classes of hysteresis operators is to characterize the operator by the slope (m) and intercept (γ) of the hysteresis loop segments. This class includes all operators with linear piecewise hysteresis loops. We compared these bounds in order to use them in the design and the analysis in the following chapters.

Chapter 3

Quantifying the Tracking Error with Proportional-Integral-Controller

3.1 Introduction

In this work we derive an expression of the tracking error under the popular control architecture that combines hysteresis inversion and feedback. What distinguishes this work from the literature reviewed in Chapter 1 is that it allows us to discuss the interaction among hysteresis parameters, uncertainties, and control gains, as well as how they determine the size of the tracking error. Furthermore, we will be able to study how the tracking error scales with the reference frequency, a question that is of practical interest but remains largely open. We will provide the analysis considering a particular linear segment and then provide a full analysis considering the cumulative behavior when the hysteresis traverses different linear segments.

Motivated by the properties of piezo-actuated nan positioning systems, we assume that the linear dynamics of the plant are stable and have large bandwidth. This assumption allows us to use singular perturbation techniques to separate the slow dynamics of the controller from the fast dynamics of the plant. Then by solving the equations for the separated models we are able to obtain an explicit expression for the tracking error where we can discuss the effect of different parameters on the size of the error. In addition, we assume that the hysteresis nonlinearity has piecewise linear

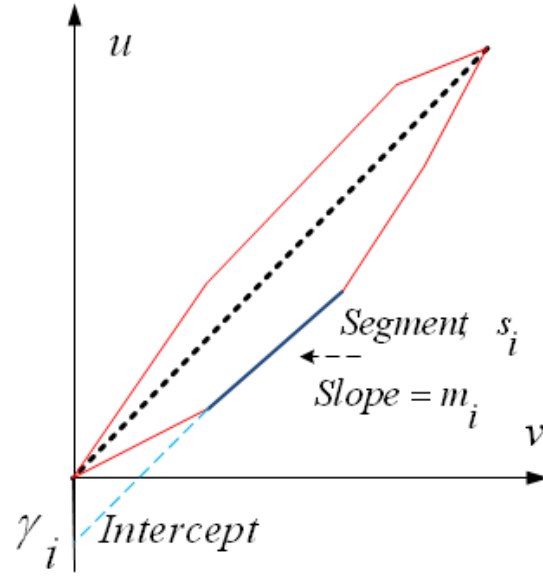


Figure 3.1: Illustration of a hysteresis loop with piecewise linear characteristics.

characteristics; in other words, all hysteresis loops (major loops and minor loops) consist of linear segments, where each segment s_i has a slope m_i and an intercept γ_i with the output axis. See Fig. 3.1 for illustration.

To fix the ideas, the tracking error analysis is conducted for a control scheme that combines the hysteresis inversion with proportional-integral feedback controller as illustrated in Fig. 3.2. In addition, we consider adding a constant-gain feedforward term to the output of the feedback controller. The analysis procedure is still applicable for the typical case of cascaded feedback and inversion by removing this feedforward branch. Although the case without the feedforward component has been reported extensively in the literature [21, 70, 47, 25, 48, 55, 56, 57], we show in this work the potential advantage of adding a feedforward gain component when the linear plant has fast dynamics. We note that feedforward control has been discussed in tracking problems with Two-Degree-of-Freedom control [71, 63, 64, 65, 62, 67] and proved to be useful in disturbance rejection and performance improvement in general, but its combination with feedback and inversion for systems with hysteresis has not been reported before. Simulation results are compared with

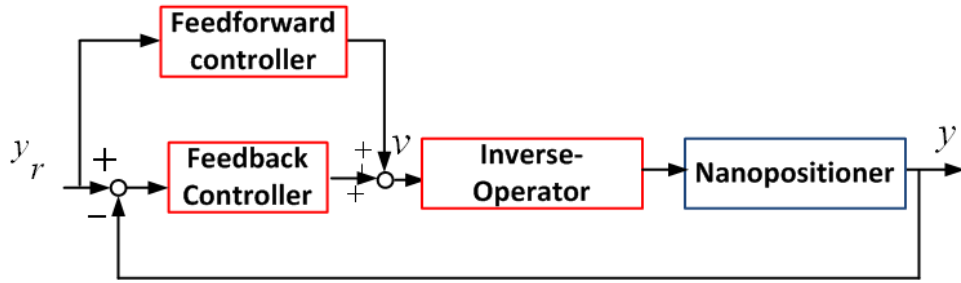


Figure 3.2: Hysteresis inversion with a control that integrates feedforward with feedback.

analytical results with good agreement. Experimental results on a commercially available nanopositioner further support our conclusions.

3.2 Closed-Loop System Setup

In this section we briefly describe the components of the closed-loop system as illustrated in Fig. 3.3. The linear dynamics of the plant are represented by a singularly perturbed system. The bandwidth of the dynamics ω_n is assumed to be large and of the order $1/\varepsilon$, where ε is a small positive parameter. The model of the linear plant is given by

$$\varepsilon \dot{z} = Az + Bu,$$

$$y = Cz \tag{3.1}$$

where A is a Hurwitz matrix, B and C are matrices with proper dimensions, and z is the state vector.

We assume that the feedback controller is a proportional-integral controller, represented as

$$\dot{x} = e = y_r - y = y_r - Cz$$

$$w = k_i x + k_p e \quad (3.2)$$

where e is the tracking error and w is the controller output. A feedforward path with a gain g is used to compensate for the DC gain of the linear dynamics. When $g = 0$, the scheme falls back into the general scheme that combines hysteresis inversion (in the feedback loop) and feedback control.

We denote the hysteresis operator by Γ_p and the inverse operator as Γ_m^{-1} , where Γ_m is the nominal model of the actual hysteresis Γ_p . The input-output relationship of Γ_p can be described in each segment of a hysteresis loop as follows

$$u = m_i v + \gamma_i \quad (3.3)$$

The DC gain of the plant is

$$h = -CA^{-1}B \quad (3.4)$$

The input to the inverse operator, u_d , and its output, v , are expressed as ¹

$$u_d = gy_r + k_i x + k_p e \quad (3.5)$$

¹For convenience, we will drop the subscript i in the analysis unless necessary and use m and γ to denote the slope and intercept of the line segment under consideration.

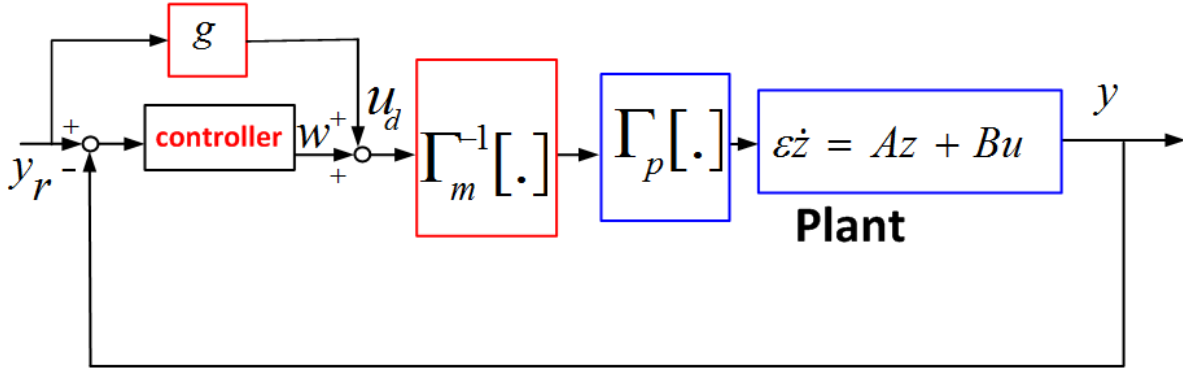


Figure 3.3: Hysteresis inverse in the feedback loop.

$$v = \frac{1}{m}(u_d - \gamma) \quad (3.6)$$

Note that (3.6) is essentially the inversion process for the piecewise linear hysteresis model, and it requires determining which linear segment of the hysteresis is on at each time instant. Such an assumption is standard in hysteresis inversion since the past history of v is available. We further note that (3.6) requires knowing the slope and intercept of the current linear segment; when such knowledge is not precise, we can represent it as follows. Let us denote the corresponding slope of the plant hysteresis Γ_p by m_p and the intercept by γ_p with parameter uncertainties Δm and $\Delta \gamma$, where $m_p = m + \Delta m$ and $\gamma_p = \gamma + \Delta \gamma$, which implies

$$u = (m + \Delta m)v + (\gamma + \Delta \gamma) \quad (3.7)$$

By substituting u_d from (3.5) and v from (3.6) into (3.7), we express u as

$$u = \frac{m + \Delta m}{m} [gy_r + k_i x + k_p (y_r - Cz)] + \frac{m\Delta\gamma - \gamma\Delta m}{m} \quad (3.8)$$

The singularly perturbed closed-loop system, obtained by inserting u from (3.8) into (3.1), is given by

$$\begin{aligned} \dot{x} &= y_r - Cz \\ \varepsilon \dot{z} &= \left[A - \frac{k_p(m + \Delta m)}{m} BC \right] z + B \frac{m + \Delta m}{m} (g + k_p) y_r + B \frac{m + \Delta m}{m} k_i x + B \left(\frac{m \Delta \gamma - \gamma \Delta m}{m} \right) \end{aligned} \quad (3.9)$$

3.3 Tracking Error Analysis

In order to get a rough idea of what factors determine the size of the error, we first assume in Section 3.3.1 that the plant is represented by a DC gain (i.e., it has an infinite bandwidth). This is equivalent to setting $\varepsilon = 0$. In this case, the tracking error e is captured by the slow model alone. We focus here on showing how the tracking error is affected by the input reference. Then, in the following subsections we discuss other factors that determine the size of the tracking error by solving the closed-loop system equations with sinusoidal or periodic references.

3.3.1 Analysis Using the Slow Model Approximation

For the fast model of the singularly perturbed system to be exponentially stable, we assume that the matrix $\left[A - \frac{k_p(m + \Delta m)}{m} BC \right]$ of (3.9) is Hurwitz. To obtain an approximation of the slow model, we set $\varepsilon = 0$, to get

$$z = - \left[A - \frac{k_p(m + \Delta m)}{m} BC \right]^{-1} B \left[\frac{m + \Delta m}{m} (g + k_p) y_r + \frac{m + \Delta m}{m} k_i x + \left(\frac{m \Delta \gamma - \gamma \Delta m}{m} \right) \right] \quad (3.10)$$

We insert z from (3.10) into the \dot{x} -equation (3.9) to obtain the approximate slow model as

$$\dot{x} = y_r + C\left(A - \frac{k_p(m + \Delta m)}{m}BC\right)^{-1}B\left[\frac{m + \Delta m}{m}(g + k_p)y_r + \frac{m + \Delta m}{m}k_i x + \left(\frac{m\Delta\gamma - \gamma\Delta m}{m}\right)\right] \quad (3.11)$$

To simplify (3.11), let us denote the expression $C\left(A - \frac{k_p(m + \Delta m)}{m}BC\right)^{-1}B$ by V and use the Matrix Inverse Lemma lemma [72] to simplify V as

$$\begin{aligned} V &= CA^{-1}B + \frac{k_p(m + \Delta m)}{m + k_p(m + \Delta m)h}CA^{-1}BCA^{-1}B \\ &= -h + \frac{k_p(m + \Delta m)}{m + k_p(m + \Delta m)h}h^2 \\ &= \frac{-mh}{m + k_p(m + \Delta m)h} \end{aligned} \quad (3.12)$$

\dot{x} can be expressed now in a simpler form by inserting the expression of V obtained from (3.12) into (3.11)

$$\dot{x} = y_r + \frac{-mh}{m + k_p(m + \Delta m)h}\left[\frac{m + \Delta m}{m}(g + k_p)y_r + \frac{m + \Delta m}{m}k_i x + \left(\frac{m\Delta\gamma - \gamma\Delta m}{m}\right)\right] \quad (3.13)$$

By rearranging and simplifying terms in (3.13), we can express, the tracking error, \dot{x} , in a form that describes the effect of different parameters and signals on it.

$$\dot{x} = \frac{-(m + \Delta m)hk_i}{m + k_p(m + \Delta m)h}x + \frac{m(1 - gh) - \Delta mgh}{m + k_p(m + \Delta m)h}y_r - h\frac{m\Delta\gamma - \gamma\Delta m}{m + k_p(m + \Delta m)h} \quad (3.14)$$

Equation (3.14) motivates the choice of $g = 1/h$. This would reduce the error due to y_r term, and \dot{x} becomes

$$\dot{x} = \frac{-(m + \Delta m)hk_i}{m + k_p(m + \Delta m)h}x + \frac{-\Delta m}{m + k_p(m + \Delta m)h}y_r - h\frac{m\Delta\gamma - \gamma\Delta m}{m + k_p(m + \Delta m)h} \quad (3.15)$$

When the feedforward path is not included, we set $g = 0$ in (3.14) and obtain

$$\dot{x} = \frac{-(m + \Delta m)hk_i}{m + k_p(m + \Delta m)h}x + \frac{m}{m + k_p(m + \Delta m)h}y_r + h\frac{m\Delta\gamma - \gamma\Delta m}{m + k_p(m + \Delta m)h} \quad (3.16)$$

To have a general idea from this approximation about the tracking error at steady state, here we only discuss the second term on the right-hand side of (3.15) and (3.16), which determines the contribution of the reference signal y_r to the tracking error e (i.e., \dot{x}). By comparing (3.15) and (3.16) we notice that when Δm is small compared to the slope m , the tracking error e will be less influenced by y_r . Moreover, we see from (3.15) that, in the ideal case ($\Delta m = 0 = \Delta\gamma$), the tracking error becomes independent of the reference signal y_r . In this case, the solution of the differential equation will only have a decaying transient term dependent on the initial value of x but independent of the segment's slope m , and according to singular perturbation theory [73] the full solution x is $O(\varepsilon)$ close to the solution of (12); that is,

$$x(t) = x(0)e^{-\frac{k_i h}{1+k_p h}t} + O(\varepsilon) \quad (3.17)$$

The effect of the linear dynamics, which are ignored in the low-frequency approximation, is abstracted in the term $O(\varepsilon)$. It is important to consider this term at high frequencies as we will see

in later analysis. From (3.15) and (3.16), one can say that by increasing the gain k_p the error would decrease. However, k_p might be constrained by the stability of the system because, for high-order linear dynamics, increasing the gain k_p beyond a certain value may destabilize the closed-loop matrix $[A - \frac{k_p(m+\Delta m)}{m}BC]$. It is also important to have the ratio k_i/k_p high in order to achieve fast decay in (3.17). In later analysis we will see that these decaying terms will be initiated whenever the signal moves to a new segment.

3.3.2 System Model and Coordinates Transformation

For more accurate approximation, we consider $\varepsilon \neq 0$ in this subsection. The system (3.9) is written in a general form as

$$\begin{bmatrix} \dot{x} \\ \varepsilon \dot{z} \end{bmatrix} = \begin{bmatrix} A_{11} & A_{12} \\ A_{21} & A_{22} \end{bmatrix} \begin{bmatrix} x \\ z \end{bmatrix} + \begin{bmatrix} B_1 \\ B_2 \end{bmatrix} y_r + \begin{bmatrix} 0 \\ \gamma' \end{bmatrix} \quad (3.18)$$

where $A_{11} = 0$, $A_{12} = -C$, $B_1 = 1$ and $(A_{21}, A_{22}, B_2, \text{ and } \gamma')$ are the corresponding matrix/vector coefficients of x, z, y_r and the constant term of equation (3.9), respectively. We keep $O(\varepsilon)$ terms of the series expansion and sum the rest as $O(\varepsilon^2)$. We use the following transformation [74], which allows us to separate the slow and fast variables:

$$\begin{bmatrix} \xi \\ \eta \end{bmatrix} = \begin{bmatrix} I_n - \varepsilon \mathcal{H} \mathcal{L} & -\varepsilon \mathcal{H} \\ \mathcal{L} & I_m \end{bmatrix} \begin{bmatrix} x \\ z \end{bmatrix} + \begin{bmatrix} \varepsilon \mathcal{H} W \\ -W \end{bmatrix} y_r \quad (3.19)$$

where ξ is the slow variable and η is the fast variable in the new coordinates. I_n and I_m are identity matrices of the dimensions of the slow and fast variables, respectively. W is a constant vector of

the dimension of the fast variable. \mathcal{L} and \mathcal{H} are analytical functions of ε , which are defined in 3.5.1. To get back to the original coordinates, we use the inverse of the above transformation:

$$\begin{bmatrix} x \\ z \end{bmatrix} = \begin{bmatrix} I_n & \varepsilon \mathcal{H} \\ -\mathcal{L} & I_m - \varepsilon \mathcal{L} \mathcal{H} \end{bmatrix} \begin{bmatrix} \xi \\ \eta \end{bmatrix} + \begin{bmatrix} 0 \\ W \end{bmatrix} y_r \quad (3.20)$$

Since we are interested in an $O(\varepsilon^2)$ approximation, we use the approximations $\mathcal{L} = L + \varepsilon A_{22}^{-2} A_{21} A_0 + O(\varepsilon^2)$ and $\mathcal{H} = H + \varepsilon A_1 + O(\varepsilon^2)$, where $L = A_{22}^{-2} A_{21}$, $H = A_{12} A_{22}^{-1}$, $A_1 = (A_0 H - H L A_{12}) A_{22}^{-1}$. $A_0 = A_{11} - A_{12} A_{22}^{-1} A_{21}$ is a scalar. We follow similar steps as in [74] to derive the system model in the new coordinates. We note that in [74] the driving term does not exist. This term will allow us to discuss the dependence of the solution on the reference y_r and its derivative \dot{y}_r . By ignoring the $O(\varepsilon^2)$ terms in all coefficients, we arrive at the following equations in which the slow and fast models are separated:

$$\dot{\xi} = (A_0 - \varepsilon H L A_0) \xi + [\varepsilon A_0 H W - H B_2 - \varepsilon A_1 B_2 + (I_n - \varepsilon H L) B_1] y_r + \varepsilon H W \dot{y}_r - H \dot{\gamma} - \varepsilon A_1 \dot{\gamma} \quad (3.21)$$

$$\varepsilon \dot{\eta} = (A_{22} + \varepsilon L A_{12}) \eta + [B_2 + \varepsilon L B_1 + (A_{22} - \varepsilon L A_{12}) W] y_r + \dot{\gamma} - \varepsilon W \dot{y}_r \quad (3.22)$$

The detailed derivation is given in Section 3.5.2. We solve (3.21) and (3.22) to get the expression of the tracking error e as follows. First for ξ , we express the solution of (3.21) as a power series

$$\xi = \xi_0 + \varepsilon \xi_1 + \varepsilon^2 \xi_2 + \dots \quad (3.23)$$

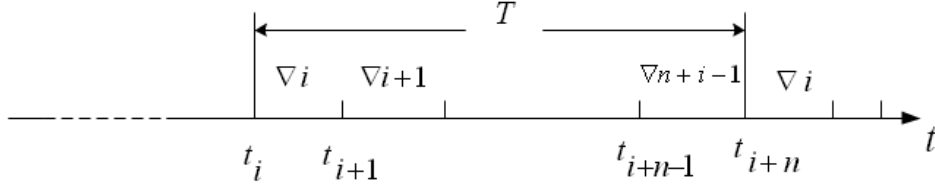


Figure 3.4: Illustration of the time instants when periodic signals cross different linear segments of the hysteresis loops.

By matching the ε - coefficients on the two sides of (3.21), we obtain

$$\dot{\xi}_0 = A_0 \xi_0 + B_0 y_r - H \gamma' \quad (3.24)$$

$$\dot{\xi}_1 = A_0 \xi_1 - H L A_0 \xi_0 + [A_0 H W - H L B_1 - A_1 B_2] y_r + H W \dot{y}_r - A_1 \gamma' \quad (3.25)$$

where $B_0 = -H B_2 + B_1$. In order to see how the solution develops and the error propagates from one hysteresis segment to another, we solve the equations for each segment by dividing the time into intervals that correspond to the periods hysteresis stays in different segments. We specify the time at the beginning of each slot by t_i , where $i = 0, 1, \dots$. Then, for the current segment i , we have the time t bounded as $t_i \leq t < t_{i+1}$. See Fig. 3.4 for illustration.

3.3.3 The Case of a Sinusoidal Reference

We now consider a sinusoidal reference $y_r = A_c \sin(\omega t)$. We assume that the solution of the closed-loop system converges to a periodic function with the same period T of the reference input. This assumption is justified by the simulation and experimental results in this work and also in [53, 55, 56, 1, 57]. Moreover, we assume that all the components which compose the solution such as the slow ξ and fast η variables are periodic of the same period T .

The idea of getting a solution that shows the impact of all hysteresis segments on each other is explained by the following steps. We start by solving (3.24) for the segment i with initial value $\xi_0(t_i)$. Then, the final value of this segment $\xi_0(t_{i+1})$ will be inserted as the initial value for the following segment $i + 1$. We continue this process around one cycle until we get $\xi_0(t_i + T)$. The periodicity of the solution implies that $\xi_0(t_i + T) = \xi_0(t_i)$ and this allows us to obtain an expression for $\xi_0(t_i)$. By substituting this expression in the solution of (3.24) we get $\xi_0(t)$, $t_i \leq t < t_{i+1}$,

$$\xi_0(t) = \varphi + \frac{H\gamma'}{A_0} + B_0 A_c \left[-\frac{A_0}{A_0^2 + \omega^2} \sin(\omega t) - \frac{\omega}{A_0^2 + \omega^2} \cos(\omega t) \right] \quad (3.26)$$

where φ is in the form

$$\varphi = e^{A_0 i(t-t_i)} \sum_{j=1}^n e^{-A_0 j K_j} \left(\frac{L_j}{A_0 j} + \frac{M_j \omega}{A_0^2 j + \omega^2} + \frac{N_j A_0 j}{A_0^2 j + \omega^2} \right) \quad (3.27)$$

n is the number of hysteresis segments traversed in one cycle, and K_j , L_j , M_j , and N_j are constants dependent on the parameters of the j -th segment in the cycle. The complete derivation of $\xi_0(t)$ and the full expression of φ are given in Section 3.5.2. The bound on φ is derived Section 3.5.3. The term φ can be described by a periodic term, which has a peak value at the beginning of each segment and decays exponentially with a speed dependent on the value A_0 until the following segment. φ is important in the sense that it connects the solutions of different segments by summing the propagated error of all previous segments in each cycle. However, this term can be made small by choice of a large value of $|A_0|$. Since the choice of A_0 is important, let us derive its expression

and see how it changes from one segment to another

$$\begin{aligned}
A_0 &= A_{11} - A_{12}A_{22}^{-1}A_{21} \\
&= 0 - C[A - k_p \frac{m + \Delta m}{m} BC]^{-1} B \frac{m + \Delta m}{m} k_i \\
&= \frac{-(m + \Delta m)k_i h}{1 + k_p(m + \Delta m)h}
\end{aligned} \tag{3.28}$$

Under the assumption that $m + \Delta m > 0$, for all segments $A_0 < 0$. By choosing k_p such that $k_p(m + \Delta m)h$ is much larger than 1, A_0 becomes independent of the segment slope and is determined by the ratio $\frac{k_i}{k_p}$. By having the integral gain much larger than the proportional gain ($k_i \gg k_p$), we guarantee that $|A_0|$ is large enough to make the value of φ significantly small and decays in a short time within each segment.

In Section 3.5.4, we show that ξ_1 is bounded uniformly in ω . Hence, the slow variable ξ is obtained by substituting ξ_0 form (3.26) into (3.23). The solution of the fast variable is derived in Section 3.5.5 as

$$\eta = \psi - A_\eta^{-1} B_\eta A_c \sin(\omega t) - A_\eta^{-1} \gamma' + \varepsilon(A_\eta^{-1} W - A_\eta^{-2} B_\eta) A_c \omega \cos(\omega t) + O(\varepsilon^2) \tag{3.29}$$

where $A_\eta = (A_{22} + \varepsilon L A_{12})$, $B_\eta = B_2 + \varepsilon L B_1 + (A_{22} + \varepsilon L A_{12})W$, and ψ is a term similar to the φ term of the slow variable, but it decays much faster than φ . The tracking error for $t_i \leq t < t_{i+1}$ in terms of ξ and η is given by

$$\begin{aligned}
e(t) &= B_1 y_r - C z \\
&= B_1 y_r + A_{12} \left[-(L + \varepsilon A_{22}^{-2} A_{21} A_0) \xi + (I_m - \varepsilon L H) \eta + W y_r \right] + O(\varepsilon^2) \\
&= -A_{12} (L + \varepsilon A_{22}^{-2} A_{21} A_0) \xi + A_{12} \eta - \varepsilon A_{12} L H \eta + (B_1 + A_{12} W) y_r + O(\varepsilon^2) \tag{3.30}
\end{aligned}$$

By inserting ξ from (3.26) and (3.23) and η from (3.29) into (3.30) and using $A_0 = -A_{12}L$ we obtain the final expression of the error with its $O(\varepsilon^2)$ approximation

$$\begin{aligned}
e(t) &= (B_1 + A_{12}W)y_r + A_0 \left[\varphi + \frac{H\gamma'}{A_0} + B_0A_c \left(\frac{-A_0}{A_0^2 + \omega^2} \sin(\omega t) - \frac{\omega}{A_0^2 + \omega^2} \cos(\omega t) \right) \right. \\
&\quad \left. + \varepsilon\xi_1 \right] - \varepsilon A_{12}A_{22}^{-2}A_{21}A_0\xi_0 + A_{12} \left[\psi - A_{\eta}^{-1}B_{\eta}A_c \sin(\omega t) - A_{\eta}^{-1}\gamma' + \varepsilon(A_{\eta}^{-1}W \right. \\
&\quad \left. - A_{\eta}^{-2}B_{\eta})A_c\omega \cos(\omega t) \right] - \varepsilon A_{12}LH[\psi - A_{\eta}^{-1}B_{\eta}A_c \sin(\omega t) - A_{\eta}^{-1}\gamma'] + O(\varepsilon^2) \quad (3.31)
\end{aligned}$$

To discuss how these terms change with the frequency, we will separate the error expression into three groups:

$$e = e_0 + \varepsilon e_{\varepsilon} + \varepsilon\omega e_{\varepsilon\omega} + O(\varepsilon^2) \quad (3.32)$$

where e_0 , e_{ε} , and $e_{\varepsilon\omega}$ are bounded uniformly in ε and ω . In other words, $|e_0| \leq k_1$, $|e_{\varepsilon}| \leq k_2$, and $|e_{\varepsilon\omega}| \leq k_3$, where k_1 , k_2 , and k_3 are some positive constants independent of ε and ω . The contribution from the e_{ε} term can be ignored because it is multiplied by a small number ε . The term $e_{\varepsilon\omega}$ becomes significant at high frequency when its coefficient $\varepsilon\omega$ is not small. Let us start with analyzing the e_0 term. By ignoring $O(\varepsilon)$ terms, A_{η}^{-1} can be approximated by A_{22}^{-1} and the term $-A_{12}A_{\eta}^{-1}$ is replaced by $-H$. Then $H\gamma'$ cancels out the term $-A_{12}A_{\eta}^{-1}\gamma'$

$$\begin{aligned}
e_0(t) &= (B_1 + A_{12}W)y_r + A_0 \left[\varphi + B_0A_c \left(\frac{-A_0}{A_0^2 + \omega^2} \sin(\omega t) - \frac{\omega}{A_0^2 + \omega^2} \cos(\omega t) \right) \right] \\
&\quad - A_{12}A_{\eta}^{-1}B_{\eta}A_c \sin(\omega t) + A_{12}\psi \quad (3.33)
\end{aligned}$$

W can be chosen such that $A_{12}W = -B_1 = -1$ and the first term is eliminated. This is always possible because $A_{12} = -C$ is rank 1 and it is a row vector with all of its elements zeros except the element representing the output of the linear plant. We can also show that $-A_{12}A_{\eta}^{-1}B_{\eta} = 1 - HB_2 = B_0$ and simplify the equation by combining sine terms together, which produces $B_0A_c \frac{\omega^2}{A_0^2 + \omega^2} \sin(\omega t)$. B_{η} is approximated by $B_2 + A_{22}W$ and multiplied by $-A_{12}A_{22}^{-1}$ to get $1 - HB_2$ and then replaced in (3.33). Then $e_0(t)$ becomes

$$e_0(t) = A_0\phi + B_0 \frac{\omega^2}{A_0^2 + \omega^2} A_c \sin(\omega t) + A_{12}\psi \quad (3.34)$$

It is noted that for a sufficiently high frequency ($|A_0| \ll \omega \ll 1/\varepsilon$), $\frac{\omega^2}{A_0^2 + \omega^2}$ becomes constant and almost independent on frequency. The $\varepsilon\omega e_{\varepsilon\omega}$ term is

$$\varepsilon\omega e_{\varepsilon\omega}(t) = A_{12}[A_{\eta}^{-1}\varepsilon W - \varepsilon A_{\eta}^{-2}B_{\eta}]\omega A_c \cos(\omega t) \quad (3.35)$$

By replacing $A_{12}[A_{\eta}^{-1}]$ by H in (3.35) we have

$$\begin{aligned} \varepsilon\omega e_{\varepsilon\omega}(t) &= \varepsilon(HW - HA_{\eta}^{-1}B_{\eta})\omega A_c \cos(\omega t) \\ &= \varepsilon(HW - HA_{22}^{-1}(B_2 + A_{22}W))\omega A_c \cos(\omega t) \\ &= -\varepsilon(HA_{22}^{-1}B_2)\omega A_c \cos(\omega t) \end{aligned} \quad (3.36)$$

By ignoring $\varepsilon e_{\varepsilon}$ and $O(\varepsilon^2)$ in (3.32) and substituting e_0 from (3.34) and $\varepsilon\omega e_{\varepsilon\omega}$ from (3.36) into (3.32), we obtain an approximate expression for the error during each segment i for a sufficiently

high frequency ($|A_0| \ll \omega \ll 1/\varepsilon$)

$$e(t) = A_0\varphi + B_0A_c \frac{\omega^2}{A_0^2 + \omega^2} \sin(\omega t) - \varepsilon(HA_{22}^{-1}B_2)\omega A_c \cos(\omega t) + A_{12}\psi \quad (3.37)$$

In summary, The bound on error is composed of two components. The decaying component which is represented by $A_0\varphi + A_{12}\psi$. This component has its peak at the beginning of each segment which can be controlled by the choice of control gains. The other non-decaying component has the following characteristics. At a very low frequency ($\omega \ll |A_0|$), the error is proportional to the frequency. This is due to the cosine term of (3.33) which is ignored later in (3.37) and the sine term of (3.37). Then, by increasing the frequency, we reach a range where the error becomes almost constant with a value that depends on the system parameters and uncertainties, B_0A_c of (3.37). Then, it starts to increase linearly with the frequency again when $\varepsilon\omega$ of the third term of (3.37) becomes large enough to contribute to the total amount of the error. This is true as long as the $O(\varepsilon^2)$ approximation is valid.

3.3.4 Bound on All Segments

The error expression (3.37) is valid for each segment. Let us again use the subscript i to denote each segment. By taking the absolute value of e and using the triangular inequality, we obtain

$$|e_i| \leq |A_{0i}\varphi_i| + |B_{0i}A_c| + |-\varepsilon(H_iA_{22,i}^{-1}B_{2,i})|\omega A_c + |A_{12}\psi_i| \quad (3.38)$$

The upper bound $|e|_{\max}$ of the error for all segments can be determined by studying when the highest value of each term in (3.38) occurs. Let us start with the second term $|B_{0i}|$. Note that

$$B_{0i} = 1 - H_i B_2 = 1 - A_{12} A_{22}^{-1} B_2 \quad (3.39)$$

Then substituting the matrices A_{12} , A_{22}^{-1} and B_2 from (3.9) into (3.39), we get

$$B_{0i} = 1 - C \left[A - k_p \frac{m_i + \Delta m_i}{m_i} BC \right]^{-1} B \frac{m_i + \Delta m_i}{m_i} (g + k_p) \quad (3.40)$$

Using the Matrix Inversion Lemma, we simplify $C \left[A - k_p \frac{m_i + \Delta m_i}{m_i} BC \right]^{-1} B$ to

$$C \left[A - k_p \frac{m_i + \Delta m_i}{m_i} BC \right]^{-1} B = \frac{-m_i h}{m_i + k_p (m_i + \Delta m_i) h} \quad (3.41)$$

Then we insert (3.41) into (3.40) to get

$$B_{0i} = \frac{m_i (1 - gh) - \Delta m_i gh}{m_i + k_p (m_i + \Delta m_i) h} \quad (3.42)$$

This expression appears as the coefficient of the driving term of Eq. (3.14). By taking the feedforward gain $g = 1/h$, we can reduce the absolute value of B_{0i} as in (3.15)

$$B_{0i} = \frac{-\Delta m_i}{m_i + k_p (m_i + \Delta m_i) h} \quad (3.43)$$

Let us denote the bound on B_{0i} by $B_{0,\max}$ for all segments. This is obtained by substituting the largest $|\Delta m|_{\max}$ in the numerator and the smallest m_{\min} in the denominator of (3.42)

$$|B_0|_{\max} < \frac{|\Delta m|_{\max}}{m_{\min} + k_p(m_{\min})h} \quad (3.44)$$

The bound on φ on all segments, $|\varphi|_{\max}$, is given in Section 3.5.3. The bound $|\psi|_{\max}$ on all segments is derived in Section 3.5.5. The upper bound $(HA_{22}^{-1}B_2)_{\max}$ on the third term of (3.38) is given in Section 3.5.6. We find that this high-frequency term is nearly independent of m and Δm for the case $|\Delta m| \ll m$. In other words, this term does not change much from one segment to another.

We conclude that the upper bound of the error can be determined by substituting m_i by m_{\max} and Δm_i by $|\Delta m|_{\max}$ in the numerator and m_i by m_{\min} in the denominator. Applying this to $|A_{0i}|$ we obtain $|A_0|_{\max}$ which replaces A_{0i} for the upper-bound on the error

$$|e|_{\max} \leq |A_0|_{\max}|\varphi|_{\max} + |B_0|_{\max}A_c + |-\varepsilon(HA_{22}^{-1}B_2)_{\max}|\omega A_c + |A_{12}\psi|_{\max} \quad (3.45)$$

3.3.5 The Case of Periodic References

The earlier analysis on the case of a sinusoidal reference can be extended to the case of a general periodic reference. We have found from the solutions of the slow and fast variables in the case of a sinusoidal reference that the steady-state solution contains two parts. One has a decaying form and is dependent on all previous segments of the hysteresis loop. The other is only dependent on the current segment and is obtained by solving an integral equation as in the conventional linear system. It is easy to show that a similar procedure can be applied to any periodic reference. For

instance,

$$\xi_0(t) = \phi_i + \frac{H_i \gamma_i'}{A_{0i}} + \int_{t_i}^t e^{A_{0i}(t-\tau)} B_{0i} y_r(\tau) d\tau \quad (3.46)$$

where ϕ_i is given by

$$\begin{aligned} \phi_i = & \frac{e^{A_{0i}(t-t_i)}}{1-M} \left[e^{A_{0,i+n-1}\Delta_{i+n-1}} \dots e^{A_{0,i+1}\Delta_{i+1}} \left(\frac{H_i \gamma_i'}{A_{0i}} - \frac{H_{i+1} \gamma_{i+1}'}{A_{0,i+1}} \right) \right. \\ & \left. + e^{A_{0i}t_{i+1}} \int_{t_i}^{t_{i+1}} e^{-A_{0i}\tau} B_{0i} y_r(\tau) d\tau \right) + \dots \\ & + e^{A_{0,i+n-1}\Delta_{i+n-1}} \left(\frac{H_{i+n-2} \gamma_{i+n-2}'}{A_{0,i+n-2}} - \frac{H_{i+n-1} \gamma_{i+n-1}'}{A_{0,i+n-1}} \right) \\ & + e^{A_{0,i+n-2}t_{i+n-1}} \int_{t_{i+n-2}}^{t_{i+n-1}} e^{-A_{0,i+n-2}\tau} B_{0,i+n-2} y_r(\tau) d\tau \\ & \left. + \left(\frac{H_{i+n-1} \gamma_{i+n-1}'}{A_{0,i+n-1}} - \frac{H_i \gamma_i'}{A_{0i}} \right) + e^{A_{0,i+n-1}t_{i+n}} \int_{t_{i+n-1}}^{t_{i+n}} e^{-A_{0,i+n-1}\tau} B_{0,i+n-1} y_r d\tau \right] \end{aligned} \quad (3.47)$$

and M is defined as

$$M = e^{A_{0,i+n-1}\Delta_{i+n-1}} \dots e^{A_{0,i+1}\Delta_{i+1}} e^{A_{0i}\Delta_i} \quad (3.48)$$

The fast variable η is derived for any periodic reference in Section 3.5.5 as

$$\eta(t) = \psi - A_{\eta_i}^{-1} \gamma_i' - A_{\eta_i}^{-1} B_{\eta_i} y_r(t) + \varepsilon A_{\eta_i}^{-1} W \dot{y}_r(t) - \varepsilon A_{\eta_i}^{-2} B_{\eta_i} \dot{y}_r(t) + O(\varepsilon^2) \quad (3.49)$$

Then, for a given periodic input $y_r(t)$ we solve the integration of (3.46) and substitute ξ and η in (3.30) to obtain the expression of the tracking error.

Since any periodic signal is bounded by a constant K , $|y_r| \leq K$, an upper bound on ϕ_i can be obtained by calculating an upper bound on the right-hand side of (3.47) and replacing $|y_r|$ by K to get

$$\begin{aligned}
|\phi_i| \leq & \frac{e^{A_{0i}(t-t_i)}}{1-M} \left[M \left| \frac{B_{0,i}K}{A_{0,i}} \right| + e^{A_{0,i+n-1}\Delta_{i+n-1}} \dots e^{A_{0,i+1}\Delta_{i+1}} \left(\left| \frac{H_i \gamma'_i}{A_{0i}} - \frac{H_{i+1} \gamma'_{i+1}}{A_{0,i+1}} \right| \right. \right. \\
& \left. \left. + \left| \frac{B_{0i}K}{A_{0i}} \right| + \left| \frac{B_{0,i+1}K}{A_{0,i+1}} \right| \right) + \dots \right. \\
& \left. + e^{A_{0,i+n-1}\Delta_{i+n-1}} \left(\left| \frac{H_{i+n-2} \gamma'_{i+n-2}}{A_{0,i+n-2}} - \frac{H_{i+n-1} \gamma'_{i+n-1}}{A_{0,i+n-1}} \right| + \left| \frac{B_{0,i+n-2}K}{A_{0,i+n-2}} \right| \right. \right. \\
& \left. \left. + \left| \frac{B_{0,i+n-1}K}{A_{0,i+n-1}} \right| \right) + \left| \frac{H_{i+n-1} \gamma'_{i+n-1}}{A_{0,i+n-1}} - \frac{H_i \gamma'_i}{A_{0i}} \right| + \left| \frac{B_{0,i+n-1}K}{A_{0,i+n-1}} \right| \right] \quad (3.50)
\end{aligned}$$

Although the bound on $|\phi_i|$ looks different from the one obtained in the case of a sinusoidal reference, they both can be made small by increasing the value of $|A_{0i}|$. However, in the case of a sinusoidal reference we have the full solution with the coefficients $\frac{A_{0i}}{A_{0i}^2 + \omega^2}$ or $\frac{\omega}{A_{0i}^2 + \omega^2}$ appearing instead of $\frac{1}{A_{0i}}$, which shows that this bound is smaller in high frequencies, $\omega > |A_{0i}|$. We should note that increasing the value of $|A_{0i}|$ reduces the value of $|\phi|$ but this is not helping much with the tracking error because we multiply ϕ by A_0 when the error is calculated.

3.4 Simulation, and Experimental Results

The simulation is based on the model and parameters identified experimentally for a commercial nanopositioner (Nano-OP65 with Nano Drive controller, Mad City Labs Inc.) The linear dynamics

are fitted experimentally with a second-order system with a natural frequency of 2086 Hz, which corresponds to $\varepsilon = 7.63 \times 10^{-5}$. The hysteresis is modeled with a PI operator with 5 play operators having thresholds $r = [0, 0.63, 1.27, 2.54, 4.45]^T$ and the vector of weights for the operator is $w^T = [5.88, 1.58, 0.47, 0.98, 0.4]$. When we apply a periodic reference signal of (with single maximum and minimum in each period, with amplitude $50 \mu\text{m}$, we obtain a loop of five segments in the ascending side and similarly in the descending side at the steady state. The slopes of the ascending side of the loop are ($m_1 = 0.67, m_2 = 0.85, m_3 = 0.9, m_4 = 1.01, m_5 = 1.057$). The slopes of the descending side of the loop are ($m_6 = 0.67, m_7 = 0.85, m_8 = 0.9, m_9 = 1.01, m_{10} = 1.057$). The intercepts are ($\gamma_1 = -6.8, \gamma_2 = -3.31, \gamma_3 = -2.58, \gamma_4 = -2.8, \gamma_5 = -2.9, \gamma_6 = 6.8, \gamma_7 = 3.31, \gamma_8 = 2.58, \gamma_9 = 2.8, \gamma_{10} = 2.9$). The weight vector of the operator is perturbed for the simulation purpose by adding 0.15 for each element to w . This perturbation changes the slopes of the loop and is equivalent to uncertainties as ($\Delta_{m1} = 0.016, \Delta_{m2} = 0.03, \Delta_{m3} = 0.05, \Delta_{m4} = 0.07, \Delta_{m5} = 0.08, \Delta_{m6} = 0.016, \Delta_{m7} = 0.03, \Delta_{m8} = 0.05, \Delta_{m9} = 0.07, \Delta_{m10} = 0.08$) and ($\Delta_{\gamma1} = -1.0313, \Delta_{\gamma2} = -0.7, \Delta_{\gamma3} = -0.46, \Delta_{\gamma4} = -0.413, \Delta_{\gamma5} = -0.7, \Delta_{\gamma6} = 1.0313, \Delta_{\gamma7} = 0.7, \Delta_{\gamma8} = 0.46, \Delta_{\gamma9} = 0.413, \Delta_{\gamma10} = 0.7$).

3.4.1 Simulation Results versus Analytical Results

Fig. 3.5 and Fig. 3.6 show the simulated tracking errors results when the feedforward branch is included, for a reference consisting of two sinusoids and a sawtooth reference signal, respectively. We observe that, in each case, the tracking error is also periodic with the same period as the reference. We also observe that the tracking error has a similar waveform as the reference input but it is distorted when the slope changes from one segment to another. This change in slopes is more obvious in the case of triangular waveform. Fig. 3.7 depicts the tracking errors for the same triangular

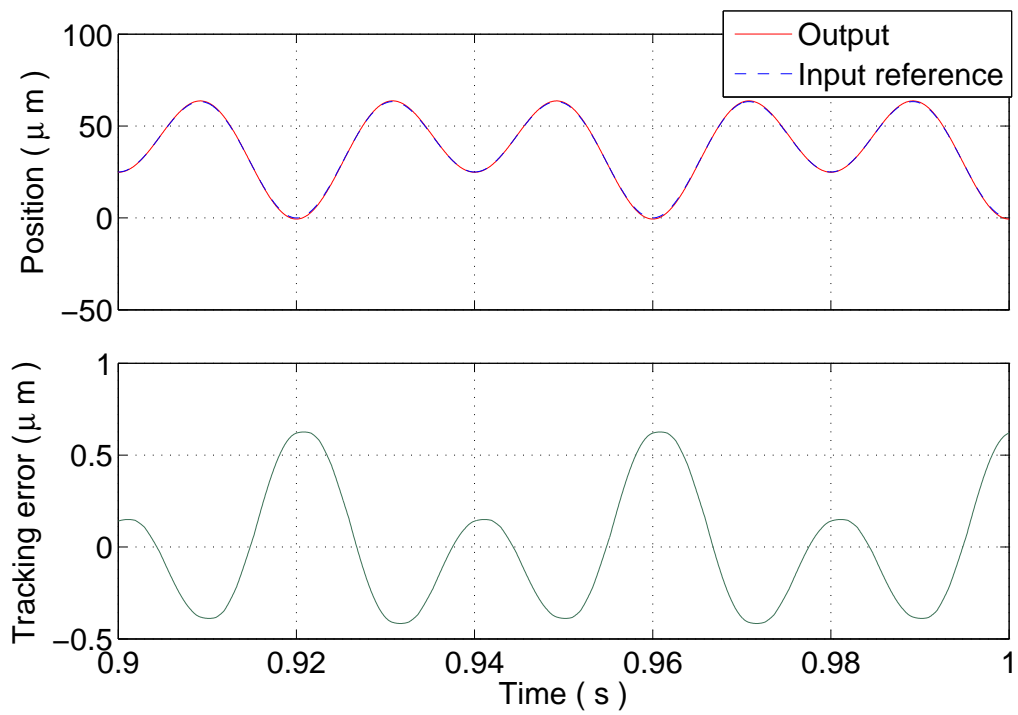


Figure 3.5: Simulations results on tracking a periodic reference composed of two sinusoidal signals of 25 Hz and 50 Hz.

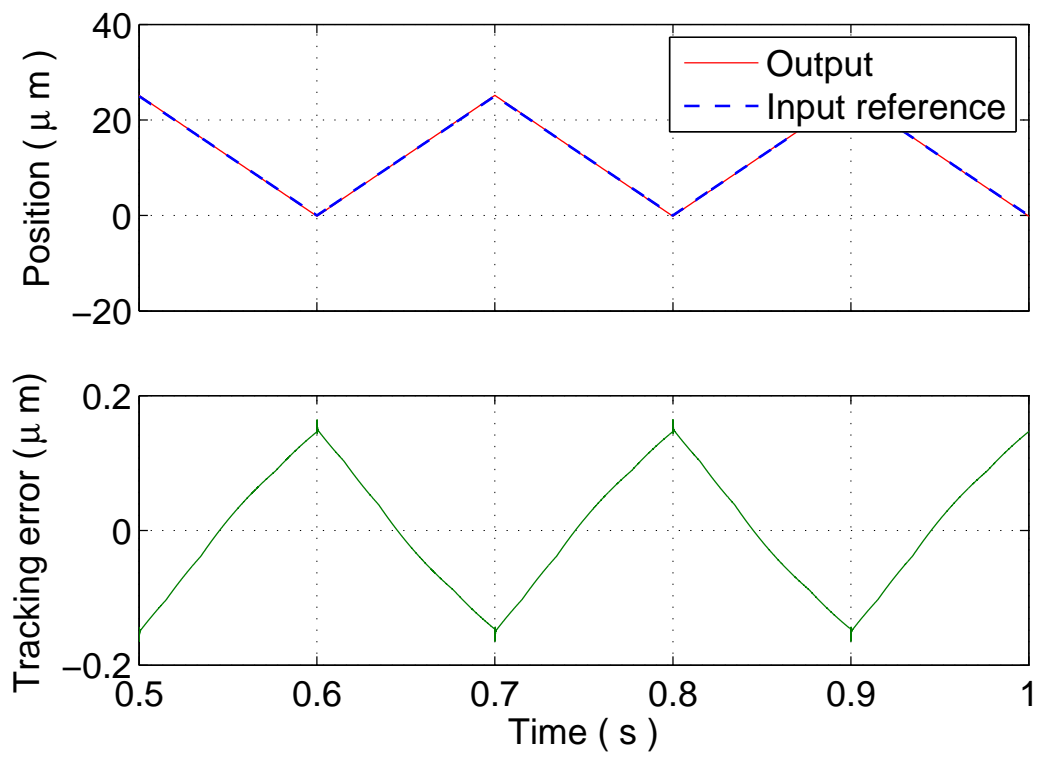


Figure 3.6: Simulation results on tracking a sawtooth reference of 5 Hz.

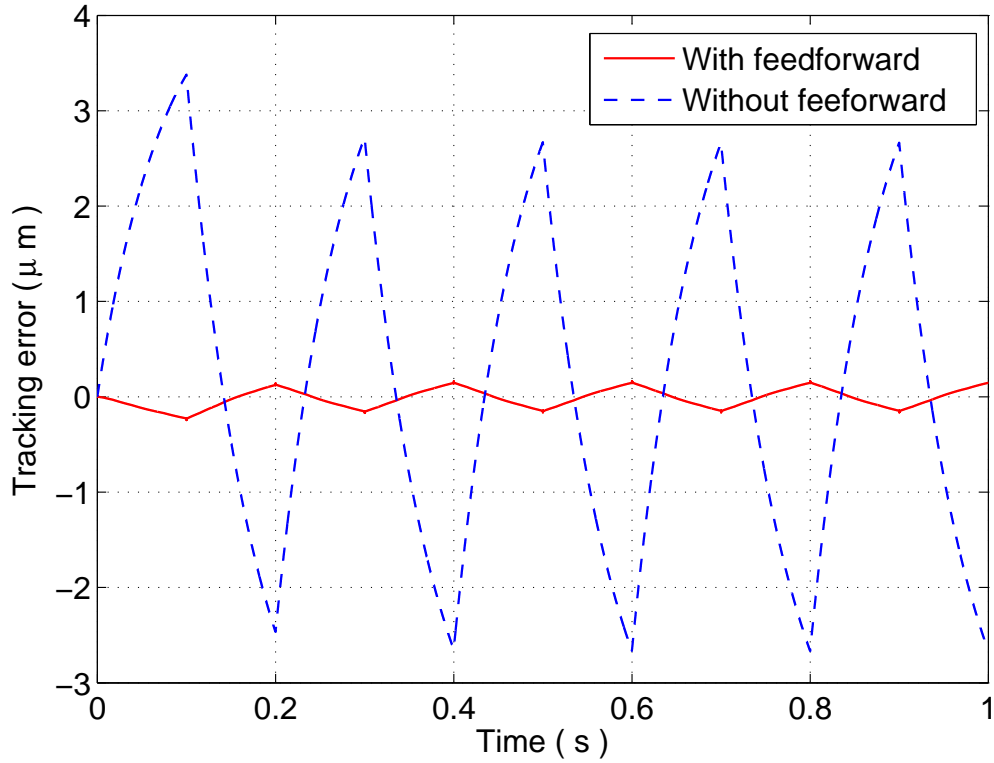


Figure 3.7: Simulation results on tracking a sawtooth reference with and without feedforward compensation, under perfect hysteresis inversion.

input reference of 5 Hz with and without feedforward term, where perfect hysteresis inversion is assumed. From these results we confirm that feedforward-augmented feedback outperforms feedback alone. Further simulation results involving the sawtooth reference are also depicted in Fig. 3.8, where we compare the tracking errors when uncertainty is present and absent in the hysteresis model. The uncertainty is introduced by perturbing the weights of play operators, as explained above. Here the feedforward term is included in the controller. From Fig. 3.8, the influence of the model uncertainty on the tracking error is evident. The size of the error for each segment is dependent on the segment slope and may be large or small depending on the value of m at that segment.

In Table 3.1, we compare the maximum amplitudes of the tracking error, when the reference

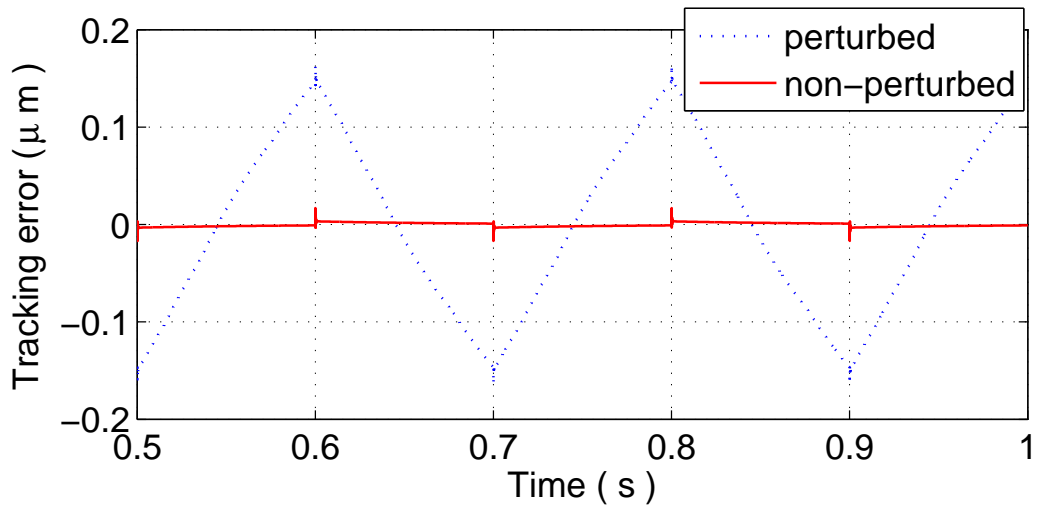


Figure 3.8: Simulation results on tracking a sawtooth reference when uncertainty is present/absent in the hysteresis model.

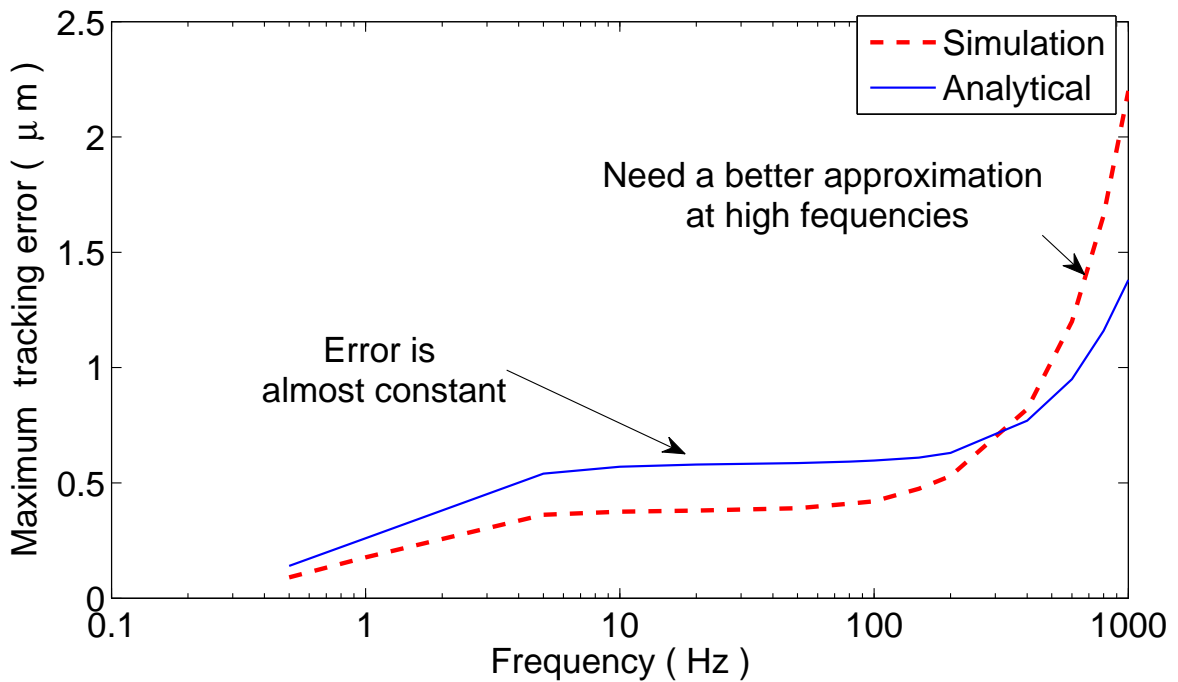


Figure 3.9: Comparison of simulation and analytical results on the tracking error as the reference frequency is varied.

signal is a sinusoid with amplitude of $50 \mu\text{m}$ and its range of frequencies is 1–1000 Hz. Here we adopt the control scheme with the feedforward term and consider the model uncertainty as discussed earlier. The gains for the proportional-integral controller are chosen as $k_i = 50$ and $k_p = 3$. Moreover, a comparison between simulation and analytical results is provided. These results are also plotted in Fig. 3.9 for a better illustration. The identified second-order plant is used in the calculation of the analytic results. The value of φ is provided in Table 3.1, which shows that it has a little effect on calculating the error especially at high frequencies. The maximum contribution of ψ to the error, which is calculated but not included in Table 3.1 is $|A_{12}\psi|_{\max} = 0.0948$. This term is almost not changing by increasing the frequency. From Table 3.1 and Fig. 3.9, we notice the following. First, for this particular example, the φ term is small and can be ignored for all frequencies of 10 Hz or higher. Second, the error obtained in simulation increases with the frequency at low frequencies, then it remains almost constant for the mid-frequency range, and then it starts to increase again with frequency. This is consistent with the error bound we calculated in the previous section. Third, the calculated error bound is close to the error from the simulation. This bound is good up to 200 Hz, because we use $O(\varepsilon^2)$ approximation which is valid for $\omega \ll 1/\varepsilon$. It is clear from these results that when frequencies become closer to the closed-loop system bandwidth, we should consider approximations higher than $O(\varepsilon^2)$ approximation.

3.4.2 Experimental Results

In experiments, sinusoidal signals are used as reference trajectories in order to compare the methods with and without the feedforward term. Fig. 3.10 shows the results for the cases of tracking 10 Hz, 35 Hz, and 50 Hz signals with amplitude of $20 \mu\text{m}$. For the best results, the control gains are chosen as $k_i = 2000$ and $k_p = 1.5$. The maximum tracking error is about $0.05 \mu\text{m}$ and slightly

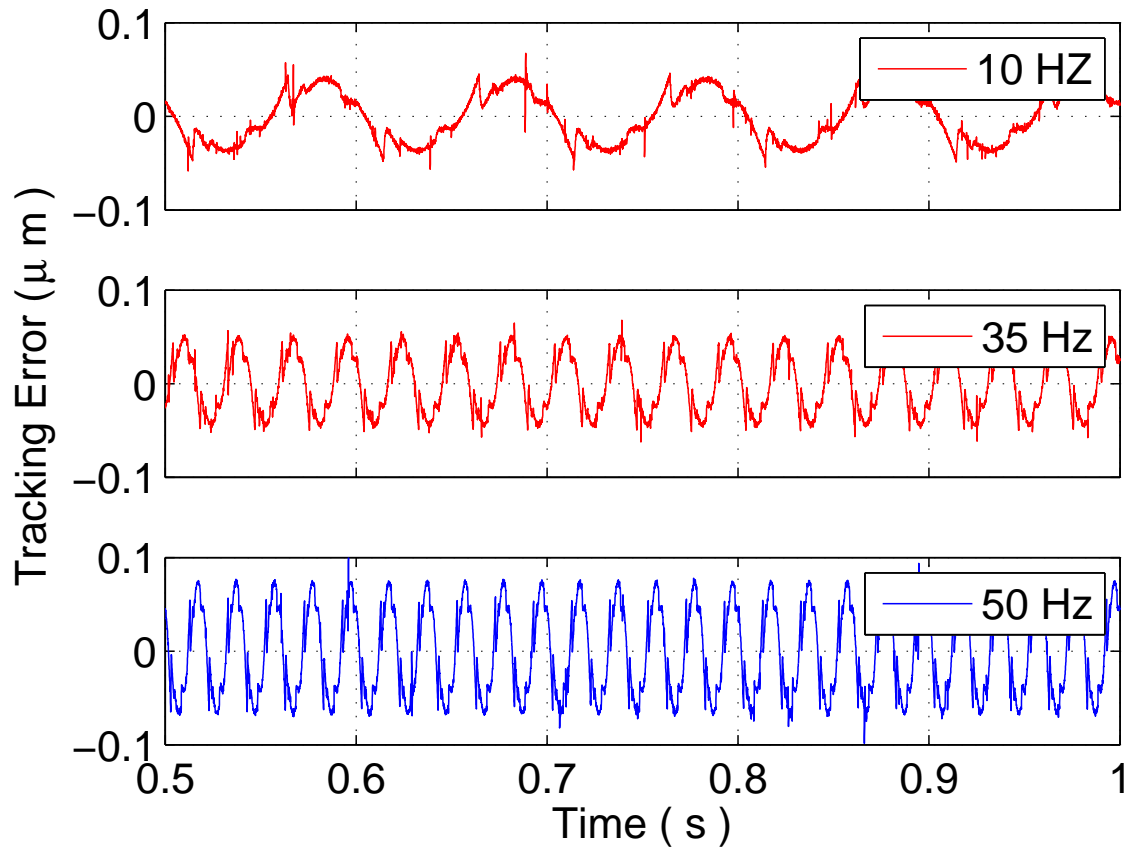


Figure 3.10: Experimental results on the tracking error for sinusoidal references of different frequencies.

increases through the range from 10 Hz to 35 Hz. We see a large increase of about $0.08 \mu\text{m}$ at 50 Hz. We also compare the tracking performance of the experimental results with simulations for the range of frequencies from 1 Hz-to- 200 Hz. The results which is plotted in Fig. 3.11 show a similar qualitative behavior of the tracking error. The tracking performance of triangular and a multi-sine signals are shown in Fig. 3.12 and Fig. 3.13, respectively. In Table 3.2, we provide more experimental results and compare the maximum tracking error between the cases when the feedforward compensation is added or removed. Fig. 3.14 shows a comparison of tracking error when the feedforward is added or removed for the triangular and multi-sine inputs. The results confirm our analysis that the scheme with the feedforward component outperforms the one without it at all

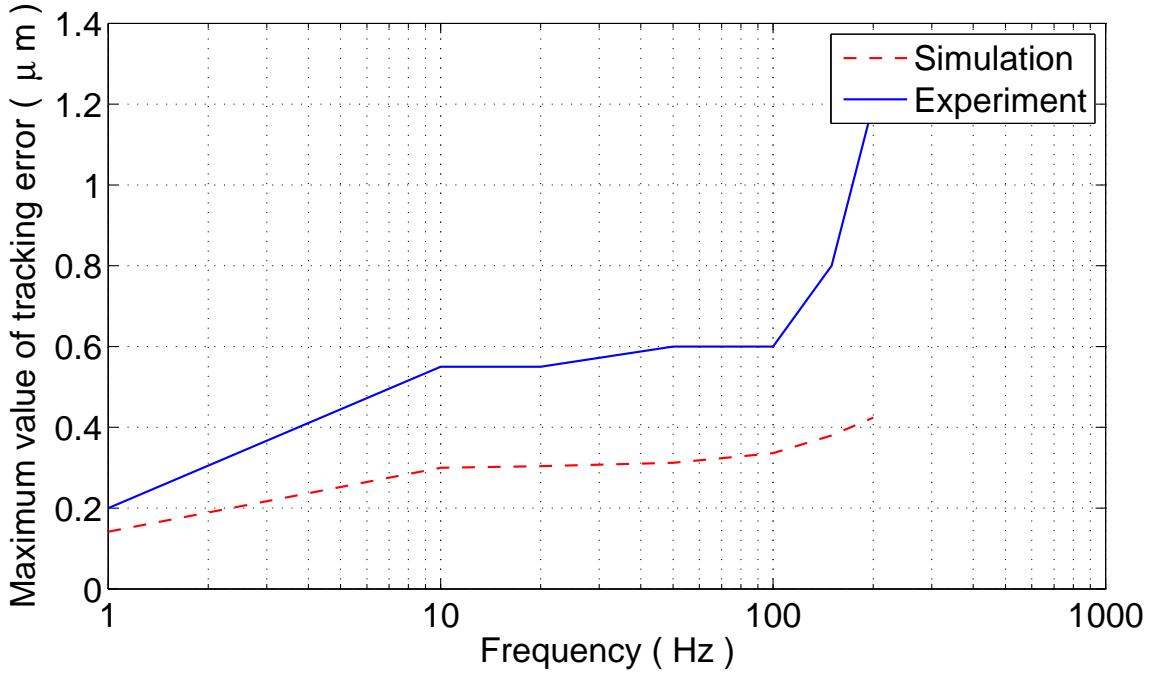


Figure 3.11: Comparison of simulation and experimental results on the tracking error as the reference frequency is varied.

frequencies and with different waveforms. In addition, we note that the frequency-dependence of the maximum tracking error follows well the trend predicted by our analytical results.

3.5 Mathematical Derivations

In this section, we will present the long derivations for the previous sections of Chapter 3.

3.5.1 Slow and Fast Variables in ξ and η Coordinates

The \mathcal{H} and \mathcal{L} matrices of (3.19) are obtained by solving the equations [74]:

$$A_{21} - A_{22}\mathcal{L} + \varepsilon\mathcal{L}A_{11} - \varepsilon\mathcal{L}A_{12}\mathcal{L} = 0 \quad (3.51)$$

$$\varepsilon(A_{11} - A_{12}\mathcal{L})\mathcal{H} - \mathcal{H}(A_{22} + \varepsilon\mathcal{L}A_{12}) + A_{12} = 0 \quad (3.52)$$

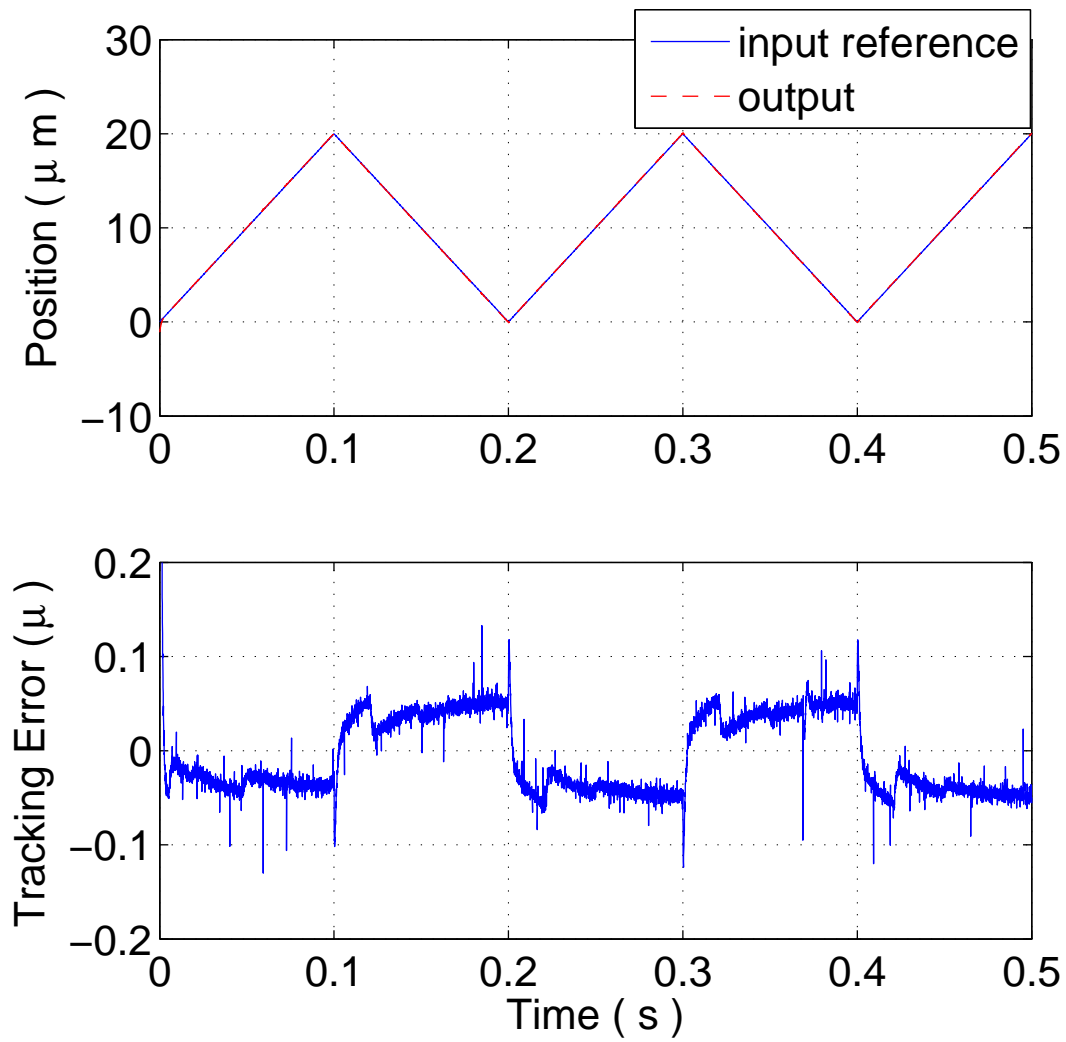


Figure 3.12: Experimental results on the tracking of a triangular reference.

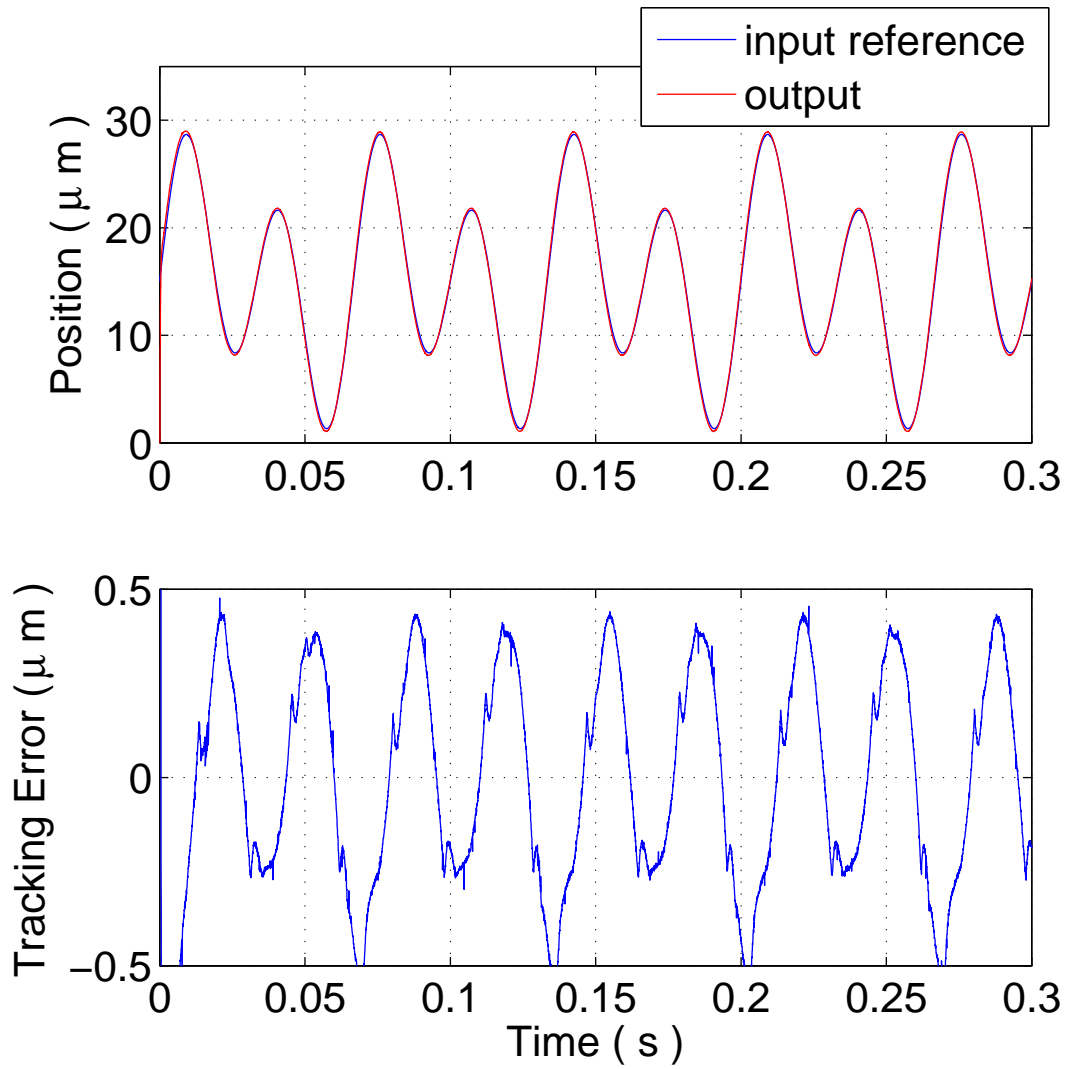


Figure 3.13: Experimental results on the tracking of a multi-sine reference with frequencies of 15 Hz and 30 Hz.

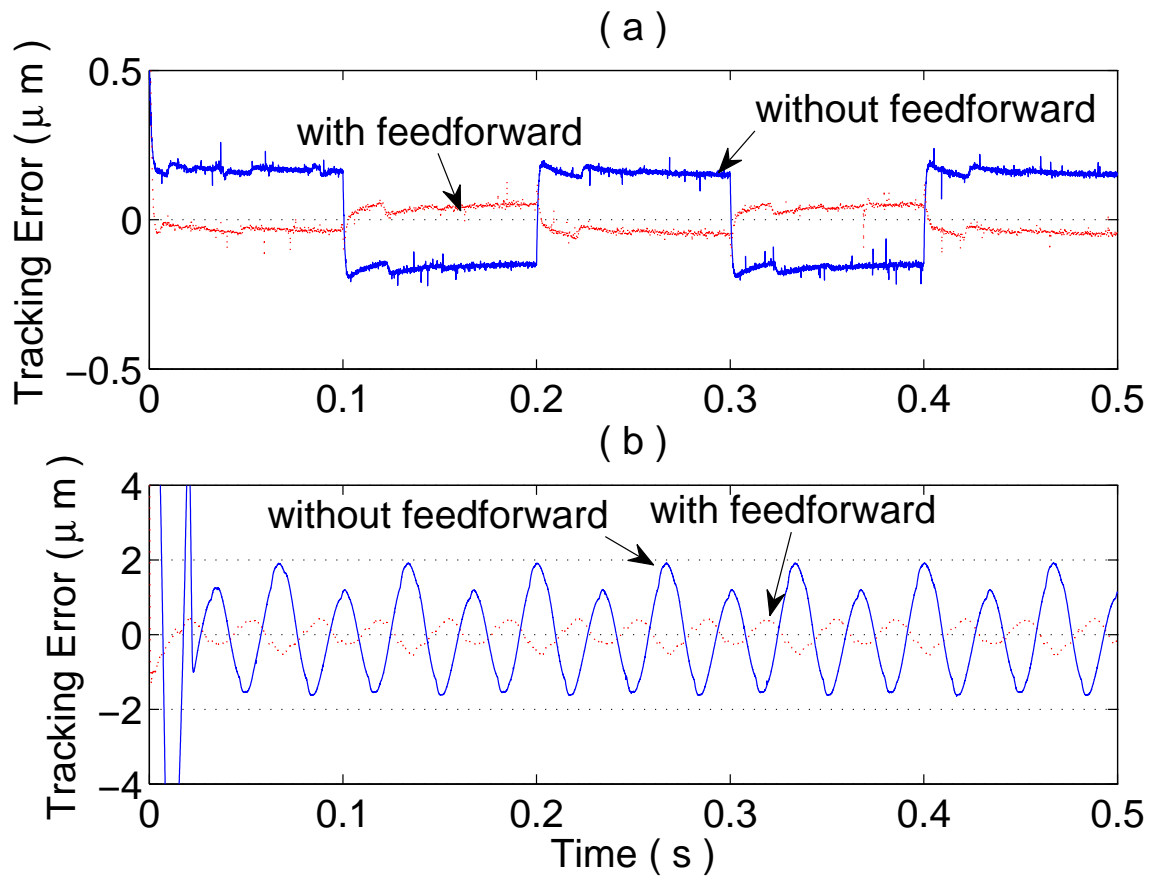


Figure 3.14: Comparison of tracking error with and without feedforward component (a) a triangular reference (b) multi-sine reference.

Following similar steps as in [74], we can show that the solutions of (3.51) and (3.52) have off-diagonal elements equal zero, and derive the system dynamics in the new coordinates as

$$\begin{aligned}
\begin{bmatrix} \dot{\xi} \\ \varepsilon \dot{\eta} \end{bmatrix} &= \begin{bmatrix} A_{11} - \mathcal{L}A_{12} & 0 \\ 0 & A_{22} + \varepsilon \mathcal{L}A_{12} \end{bmatrix} \begin{bmatrix} \xi \\ \eta \end{bmatrix} \\
&+ \begin{bmatrix} \varepsilon(A_{11} - \mathcal{L}A_{12})\mathcal{H}W - \mathcal{H}B_2 + (I_n - \varepsilon \mathcal{H}\mathcal{L})B_1 \\ B_2 + \varepsilon \mathcal{L}B_1 - (A_{22} + \varepsilon \mathcal{L}A_{12})W \end{bmatrix} y_r \\
&+ \begin{bmatrix} \varepsilon \mathcal{H}W \\ -\varepsilon W \end{bmatrix} \dot{y}_r + \begin{bmatrix} -\mathcal{H}\gamma' \\ \gamma' \end{bmatrix}
\end{aligned} \tag{3.53}$$

where $A_0 = A_{11} - A_{12}A_{22}^{-1}A_{21}$. It is often helpful that, instead of using the exact solutions of \mathcal{L} and \mathcal{H} , we use their approximations [74]. It is shown in [74] that \mathcal{L} and \mathcal{H} can be approximated by $\mathcal{L} = L + \varepsilon A_{22}^{-2}A_{21}A_0 + O(\varepsilon^2)$ and $\mathcal{H} = H - \varepsilon A_1 + O(\varepsilon^2)$, respectively, where, $L = A_{22}^{-1}A_{21}$, $H = A_{12}A_{22}^{-1}$, $A_1 = (A_0H - HLA_{21})A_{22}^{-1}$. By substituting the approximations of \mathcal{L} and \mathcal{H} into (3.53) and ignoring the $O(\varepsilon^2)$ terms, we obtain an $O(\varepsilon^2)$ approximation of $\dot{\xi}$ and $\varepsilon \dot{\eta}$ shown in (3.21) and (3.22).

3.5.2 Solution of ξ_0

In order to see how the solution develops and the error propagates from one hysteresis segment to another, we solve the equations for each segment by dividing the time into intervals that correspond to the time periods of the hysteresis staying in different segments. The solution of (3.24) for

$t_i \leq t < t_{i+1}$ is

$$\xi_0(t) = e^{A_{0i}(t-t_i)} \xi_0(t_i) + \int_{t_i}^t e^{A_{0i}(t-\tau)} (B_{0i} A_c \sin(\omega\tau) - H_i \gamma_i') d\tau \quad (3.54)$$

which can be readily derived as

$$\begin{aligned} \xi_0(t) &= e^{A_{0i}(t-t_i)} \xi_0(t_i) + \frac{H_i \gamma_i'}{A_{0i}} [1 - e^{A_{0i}(t-t_i)}] \\ &\quad - e^{A_{0i}(t-t_i)} B_{0i} A_c \left[\frac{-A_{0i}}{A_{0i}^2 + \omega^2} \sin(\omega t_i) - \frac{\omega}{A_{0i}^2 + \omega^2} \cos(\omega t_i) \right] \\ &\quad + B_{0i} A_c \left[\frac{-A_{0i}}{A_{0i}^2 + \omega^2} \sin(\omega t) - \frac{\omega}{A_{0i}^2 + \omega^2} \cos(\omega t) \right] \end{aligned} \quad (3.55)$$

With the assumption that the solution is periodic, we solve ξ_0 by starting at one segment i and continue solving for all n segments until we return back to segment i after a period T . At time $t = t_{i+1}$, Eq. (3.55) becomes

$$\begin{aligned} \xi_0(t_{i+1}) &= e^{A_{0i}(t_{i+1}-t_i)} \xi_0(t_i) + \frac{H_i \gamma_i'}{A_{0i}} [1 - e^{A_{0i}(t_{i+1}-t_i)}] \\ &\quad - e^{A_{0i}(t_{i+1}-t_i)} B_{0i} A_c \left[\frac{-A_{0i}}{A_{0i}^2 + \omega^2} \sin(\omega t_i) - \frac{\omega}{A_{0i}^2 + \omega^2} \cos(\omega t_i) \right] \\ &\quad + B_{0i} A_c \left[\frac{-A_{0i}}{A_{0i}^2 + \omega^2} \sin(\omega t_{i+1}) - \frac{\omega}{A_{0i}^2 + \omega^2} \cos(\omega t_{i+1}) \right] \end{aligned} \quad (3.56)$$

By accumulation of the foregoing expression over n segment we obtain

$$\begin{aligned}
\xi_0(t_{n+i}) = & e^{A_{0,i+n-1}(t_{n+i}-t_{n+i-1})} e^{A_{0,n+i-2}(t_{n+i-1}-t_{n+i-2})} \dots e^{A_{0i}(t_{i+1}-t_i)} [\xi_0(t_i) \\
& - \frac{H_i \gamma_i'}{A_{0i}} - B_{0i} A_c \left[\frac{-A_{0i}}{A_{0i}^2 + \omega^2} \sin(\omega t_i) - \frac{\omega}{A_{0i}^2 + \omega^2} \cos(\omega t_i) \right] \\
& + e^{A_{0,i+n-1}(t_{n+i}-t_{n+i-1})} e^{A_{0,i+n-2}(t_{n+i-1}-t_{n+i-2})} \dots e^{A_{0,i+1}(t_{i+2}-t_{i+1})} \\
& \left[\left(\frac{H_i \gamma_i'}{A_{0i}} - \frac{H_{i+1} \gamma_{i+1}'}{A_{0,i+1}} \right) + A_c \left[\left(\frac{-B_{0i} A_{0i}}{A_{0i}^2 + \omega^2} + \frac{B_{0,i+1} A_{0,i+1}}{A_{0,i+1}^2 + \omega^2} \right) \sin(\omega t_{i+1}) - \left(\frac{B_{0i} \omega}{A_{0i}^2 + \omega^2} \right. \right. \right. \\
& \left. \left. - \frac{B_{0,i+1} \omega}{A_{0,i+1}^2 + \omega^2} \right) \cos(\omega t_{i+1}) \right] + \dots + e^{A_{0,i+n-1}(t_{n+i}-t_{n+i-1})} \\
& \left[\left(\frac{H_{i+n-2} \gamma_{i+n-2}'}{A_{0,i+n-2}} - \frac{H_{i+n-1} \gamma_{i+n-1}'}{A_{0,i+n-1}} \right) + A_c \left[\left(\frac{-B_{0,i+n-2} A_{0,i+n-2}}{A_{0,i+n-2}^2 + \omega^2} \right. \right. \right. \\
& \left. \left. + \frac{B_{0,i+n-1} A_{0,i+n-1}}{A_{0,i+n-1}^2 + \omega^2} \right) \sin(\omega t_{n+i-1}) - \left(\frac{B_{0,i+n-2} \omega}{A_{0,i+n-2}^2 + \omega^2} \right. \right. \\
& \left. \left. - \frac{B_{0,i+n-1} \omega}{A_{0,i+n-1}^2 + \omega^2} \right) \cos(\omega t_{n+i-1}) \right] + \frac{H_{i+n-1} \gamma_{i+n-1}'}{A_{0,i+n-1}} \\
& + B_{0,i+n-1} A_c \left[\frac{-A_{0,i+n-1}}{A_{0,i+n-1}^2 + \omega^2} \sin(\omega t_{n+i}) - \frac{\omega}{A_{0,i+n-1}^2 + \omega^2} \cos(\omega t_{n+i}) \right] \quad (3.57)
\end{aligned}$$

Because the solution is periodic, we can replace t_{n+i} by t_i in the left side of equation (3.57) and rewriting it in terms of $\xi_0(t_i)$:

$$\begin{aligned}
\xi_0(t_i) = & \frac{M}{1-M} \left[-\frac{H_i \gamma_i'}{A_{0i}} - B_{0i} A_c \left[\frac{-A_{0i}}{A_{0i}^2 + \omega^2} \sin(\omega t_i) - \frac{\omega}{A_{0i}^2 + \omega^2} \cos(\omega t_i) \right] \right] \\
& + \frac{1}{1-M} \left(e^{A_{0,i+n-1}(t_{n+i} - t_{n+i-1})} e^{A_{0,i+n-2}(t_{n+i-1} - t_{n+i-2})} \dots \right. \\
& e^{A_{0,i+1}(t_{i+2} - t_{i+1})} \left[\left(\frac{H_i \gamma_i'}{A_{0i}} - \frac{H_{i+1} \gamma_{i+1}'}{A_{0,i+1}} \right) + A_c \left[\left(\frac{-B_{0i} A_{0i}}{A_{0i}^2 + \omega^2} + \frac{B_{0,i+1} A_{0,i+1}}{A_{0,i+1}^2 + \omega^2} \right) \sin(\omega t_{i+1}) \right. \right. \\
& \left. \left. - \left(\frac{B_{0i} \omega}{A_{0i}^2 + \omega^2} - \frac{B_{0,i+1} \omega}{A_{0,i+1}^2 + \omega^2} \right) \cos(\omega t_{i+1}) \right] \right) + \dots \\
& + e^{A_{0,i+n-1}(t_{n+i} - t_{n+i-1})} \left[\left(\frac{H_{i+n-2} \gamma_{i+n-2}'}{A_{0,i+n-2}} - \frac{H_{i+n-1} \gamma_{i+n-1}'}{A_{0,i+n-1}} \right) \right. \\
& + A_c \left[\left(\frac{-B_{0,i+n-2} A_{0,i+n-2}}{A_{0,i+n-2}^2 + \omega^2} + \frac{B_{0,i+n-1} A_{0,i+n-1}}{A_{0,i+n-1}^2 + \omega^2} \right) \sin(\omega t_{n+i-1}) \right. \\
& \left. \left. - \left(\frac{B_{0,i+n-2} \omega}{A_{0,i+n-2}^2 + \omega^2} - \frac{B_{0,i+n-1} \omega}{A_{0,i+n-1}^2 + \omega^2} \right) \cos(\omega t_{n+i-1}) \right] \right] + \frac{H_{i+n-1} \gamma_{i+n-1}'}{A_{0,i+n-1}} \\
& \left. + B_{0,i+n-1} A_c \left[\frac{-A_{0,i+n-1}}{A_{0,i+n-1}^2 + \omega^2} \sin(\omega t_{n+i}) - \frac{\omega}{A_{0,i+n-1}^2 + \omega^2} \cos(\omega t_{n+i}) \right] \right) \quad (3.58)
\end{aligned}$$

where $M = e^{A_{0,i+n-1} \Delta_{i+n-1}} \dots e^{A_{0,i+1} \Delta_{i+1}} e^{A_{0,i} \Delta_i}$. By inserting $\xi_0(t_i)$ of (3.58) into (3.55), we obtain the solution of $\xi_0(t)$ at the steady state as

$$\begin{aligned}
\xi_0(t) = & \varphi + \frac{H_i \gamma_i'}{A_{0i}} + B_{0i} A_c \left(\frac{-A_{0i}}{A_{0i}^2 + \omega^2} \sin(\omega t) \right. \\
& \left. - \frac{\omega}{A_{0i}^2 + \omega^2} \cos(\omega t) \right) \quad (3.59)
\end{aligned}$$

where φ is the periodic decaying term defined as

$$\begin{aligned}
\varphi = & \frac{e^{A_{0i}(t-t_i)}}{1-M} \left(-\frac{H_i \gamma_i'}{A_{0i}} - B_{0i} A_c \left[\frac{-A_{0i}}{A_{0i}^2 + \omega^2} \sin(\omega t_i) - \frac{\omega}{A_{0i}^2 + \omega^2} \cos(\omega t_i) \right] \right) \\
& + e^{A_{0,i+n-1}(t_{n+i}-t_{n+i-1})} e^{A_{0,i+n-2}(t_{n+i-1}-t_{n+i-2})} \dots e^{A_{0,i+1}(t_{i+2}-t_{i+1})} \\
& \left[\left(\frac{H_i \gamma_i'}{A_{0i}} - \frac{H_{i+1} \gamma_{i+1}'}{A_{0,i+1}} \right) + A_c \left[\left(\frac{-B_{0i} A_{0i}}{A_{0i}^2 + \omega^2} + \frac{B_{0,i+1} A_{0,i+1}}{A_{0,i+1}^2 + \omega^2} \right) \sin(\omega t_{i+1}) - \left(\frac{B_{0i} \omega}{A_{0i}^2 + \omega^2} \right. \right. \right. \\
& \left. \left. \left. - \frac{B_{0,i+1} \omega}{A_{0,i+1}^2 + \omega^2} \right) \cos(\omega t_{i+1}) \right] \right] + \dots \\
& + e^{A_{0,i+n-1}(t_{n+i}-t_{n+i-1})} \left[\left(\frac{H_{i+n-2} \gamma_{i+n-2}'}{A_{0,i+n-2}} - \frac{H_{i+n-1} \gamma_{i+n-1}'}{A_{0,i+n-1}} \right) \right. \\
& + A_c \left[\left(\frac{-B_{0,i+n-2} A_{0,i+n-2}}{A_{0,i+n-2}^2 + \omega^2} + \frac{B_{0,i+n-1} A_{0,i+n-1}}{A_{0,i+n-1}^2 + \omega^2} \right) \sin(\omega t_{n+i-1}) \right. \\
& \left. \left. - \left(\frac{B_{0,i+n-2} \omega}{A_{0,i+n-2}^2 + \omega^2} - \frac{B_{0,i+n-1} \omega}{A_{0,i+n-1}^2 + \omega^2} \right) \cos(\omega t_{n+i-1}) \right] \right] + \left(\frac{H_{i+n-1} \gamma_{i+n-1}'}{A_{0,i+n-1}} \right) \\
& \left. + B_{0,i+n-1} A_c \left[\frac{-A_{0,i+n-1}}{A_{0,i+n-1}^2 + \omega^2} \sin(\omega t_{n+i}) - \frac{\omega}{A_{0,i+n-1}^2 + \omega^2} \cos(\omega t_{n+i}) \right] \right) \quad (3.60)
\end{aligned}$$

3.5.3 Calculating the Bound on φ

We assume that there is a negative constant $-a$ such that $A_{0i} \leq -a$. Then for all i , $e^{A_{0i}\sigma} \leq e^{-a\sigma}$. M is bounded as $M \leq e^{-aT}$. We substitute the bound on M in (3.60) and then replace the duration for each segment by $\Delta_i = t_{i+1} - t_i$ and the sum of Δ_i 's over one cycle by T , which results in, for

$$t_i \leq t < t_{i+1},$$

$$\begin{aligned}
|\varphi| \leq & \frac{1}{1-e^{-aT}} \left(\left| -\frac{H_i \gamma_i'}{A_{0i}} - B_{0i} A_c \left[\frac{-A_{0i}}{A_{0i}^2 + \omega^2} \sin(\omega t_i) - \frac{\omega}{A_{0i}^2 + \omega^2} \cos(\omega t_i) \right] \right| \right. \\
& + e^{-a(T-\Delta_i)} \left| \left(\frac{H_i \gamma_i'}{A_{0i}} - \frac{H_{i+1} \gamma_{i+1}'}{A_{0,i+1}} \right) \right. \\
& + A_c \left[\left(\frac{-B_{0i} A_{0i}}{A_{0i}^2 + \omega^2} + \frac{B_{0,i+1} A_{0,i+1}}{A_{0,i+1}^2 + \omega^2} \right) \sin(\omega t_{i+1}) - \left(\frac{B_{0i} \omega}{A_{0i}^2 + \omega^2} - \frac{B_{0,i+1} \omega}{A_{0,i+1}^2 + \omega^2} \right) \cos(\omega t_{i+1}) \right] \left. \right| \\
& + \dots \\
& + e^{-a\Delta_n} \left| \left(\frac{H_{i+n-2} \gamma_{i+n-2}'}{A_{0,i+n-2}} - \frac{H_{i+n-1} \gamma_{i+n-1}'}{A_{0,i+n-1}} \right) + A_c \left[\left(\frac{-B_{0,i+n-2} A_{0,i+n-2}}{A_{0,i+n-2}^2 + \omega^2} \right. \right. \right. \\
& + \left. \left. \frac{B_{0,i+n-1} A_{0,i+n-1}}{A_{0,i+n-1}^2 + \omega^2} \right) \sin(\omega t_{n+i-1}) - \left(\frac{B_{0,i+n-2} \omega}{A_{0,i+n-2}^2 + \omega^2} \right. \right. \\
& \left. \left. - \frac{B_{0,i+n-1} \omega}{A_{0,i+n-1}^2 + \omega^2} \right) \cos(\omega t_{n+i-1}) \right] \left. \right| + \left| \left(\frac{H_{i+n-1} \gamma_{i+n-1}'}{A_{0,i+n-1}} \right) \right. \\
& \left. + B_{0,i+n-1} A_c \left[\frac{-A_{0,i+n-1}}{A_{0,i+n-1}^2 + \omega^2} \sin(\omega t_{n+i}) - \frac{\omega}{A_{0,i+n-1}^2 + \omega^2} \cos(\omega t_{n+i}) \right] \right| \left. \right) \quad (3.61)
\end{aligned}$$

Let us denote the right hand side by \mathcal{K} . Then φ is bounded at any time by this constant \mathcal{K} , $|\varphi| \leq \mathcal{K}$. The components of φ , which are described in Eq. (3.60), are functions of either B_{0i} which are bounded by $|B_0|_{\max}$ given in (3.44) or $H_i \gamma_i'$ where we can determine its bound $|(H \gamma')|_{\max}$ by inserting the matrix expressions. Note that

$$\begin{aligned}
H_i \gamma_i' &= -C \left[A - k_p \frac{m_i + \Delta m_i}{m_i} B C \right]^{-1} B \left(\frac{m_i \Delta \gamma_i - \gamma_i \Delta m_i}{m_i} \right) \\
&= \frac{-h(m_i \Delta \gamma_i - \gamma_i \Delta m_i)}{1 + k_p(m_i + \Delta m_i)h} \quad (3.62)
\end{aligned}$$

The bound on $H_i\gamma_i'$ of all segments can be obtained as

$$|(H\gamma')|_{\max} \leq \frac{h|\gamma_{\max}||\Delta m|_{\max} + m_{\max}\Delta\gamma_{\max}|}{1 + k_p(m_{\min})h} \quad (3.63)$$

By replacing $|B_{0i}|$ by $|B_0|_{\max}$ and $H_i\gamma_i'$ by $|(H\gamma')|_{\max}$ in (3.61) we get the upper bound for all segments $|\varphi| \leq |\varphi|_{\max}$. However, this bound is very conservative and might not be useful in calculating the bound on the error. It is noted from Table 3.1 that φ is small particularly at high frequency and can be ignored. This is can be explained from (3.60) as follows; at a sufficiently large frequency the exponential terms inside the parenthesis becomes close to one. We also observe that every term inside the parenthesis has a similar term with opposite sign that cancels it out when the exponential terms becomes close to one.

3.5.4 Solution for ξ_1

To solve for ξ_1 , insert ξ_0 from (3.59) into (3.25)

$$\begin{aligned} \dot{\xi}_1 &= A_{0i}\xi_1 - HLA_{0i}[\varphi \\ &\quad - \frac{H_i\gamma_i'}{A_{0i}} + B_{0i}A_c(\frac{A_{0i}}{A_{0i}^2 + \omega^2} \sin(\omega t) - \frac{\omega}{A_{0i}^2 + \omega^2} \cos(\omega t))] \\ &\quad + [A_0HW - HLB_1 - A_1B_2]A_c \sin(\omega t) + HWA_c\omega \cos(\omega t) \end{aligned} \quad (3.64)$$

By combining similar terms, we can rewrite (3.64) as

$$\dot{\xi}_1 = A_0\xi_1 + \alpha_1 \sin(\omega t) + \alpha_2 \cos(\omega t) + \alpha_3 \omega \cos(\omega t) + Q \quad (3.65)$$

where Q is a constant and α_1 , α_2 , and α_3 are bounded uniformly in ω . We notice from (3.65) that $\dot{\xi}_1$ has the same form as $\dot{\xi}_0$ of (3.24) except with an extra term which comes from \dot{y}_r and is proportional to the frequency ω . Since ξ_1 in the solution of the error will be multiplied by ε , it matters in determining the bound only if any terms of its solution can be approximated by a quantity that is proportional to ω . However, through similar derivation as for ξ_0 , we will have a solution to ξ_1 with extra terms of sine and cosine terms multiplied by ω . These terms appears as follows

$$\alpha_3 \omega \left(\frac{\omega}{A_{0i}^2 + \omega^2} \sin(\omega t) + \frac{A_{0i}}{A_{0i}^2 + \omega^2} \cos(\omega t) \right)$$

which are bounded by a constant independent of the frequency and hence belong to the e_{ε} terms of Eq. (3.32).

3.5.5 Fast Variable Analysis

Now we need to express the fast variable η using its model (3.22) by finding $O(1)$ and $O(\varepsilon)$ terms.

Let us simplify (3.22) as

$$\varepsilon \dot{\eta} = A_{\eta_i} \eta + B_{\eta_i} y_r + \dot{\gamma}_i - \varepsilon W \dot{y}_r \tag{3.66}$$

where $A\eta = (A_{22} + \varepsilon LA_{12})$, $B\eta = B_2 + \varepsilon LB_1 - (A_{22} + \varepsilon LA_{12})W$. The solution of (3.66) for $t_i \leq t < t_{i+1}$ is

$$\begin{aligned}
\eta(t) &= e^{A\eta_i(t-t_i)/\varepsilon} \eta(t_i) + \frac{1}{\varepsilon} \int_{t_i}^t e^{A\eta_i(t-\tau)/\varepsilon} [B\eta_i y_r + \gamma_i' \\
&\quad - \varepsilon W y_r(\tau)] d\tau \\
&= e^{A\eta_i(t-t_i)/\varepsilon} \eta(t_i) - A\eta_i^{-1} e^{A\eta_i(t-\tau)/\varepsilon} \Big|_{t_i}^t \gamma_i' \\
&\quad + \frac{1}{\varepsilon} \int_{t_i}^t e^{A\eta_i(t-\tau)/\varepsilon} B\eta_i y_r(\tau) d\tau \\
&\quad - \int_{t_i}^t e^{A\eta_i(t-\tau)/\varepsilon} W y_r(\tau) d\tau
\end{aligned} \tag{3.67}$$

In order to simplify the integration of (3.67), we use the change of variables $\tau = t - \varepsilon\sigma$

$$\begin{aligned}
\eta(t) &= e^{A\eta_i(t-t_i)/\varepsilon} \eta(t_i) - A\eta_i^{-1} \gamma_i' + A\eta_i^{-1} e^{A\eta_i(t-t_i)/\varepsilon} \gamma_i' \\
&\quad + \int_0^{(t-t_i)/\varepsilon} e^{A\eta_i\sigma} B\eta_i y_r(t - \varepsilon\sigma) d\sigma \\
&\quad - \varepsilon \int_0^{(t-t_i)/\varepsilon} e^{A\eta_i\sigma} W y_r(t - \varepsilon\sigma) d\sigma
\end{aligned} \tag{3.68}$$

With integration by parts, the first integral becomes

$$\begin{aligned}
&\int_0^{(t-t_i)/\varepsilon} e^{A\eta_i\sigma} B\eta_i y_r(t - \varepsilon\sigma) d\sigma \\
&= A\eta_i^{-1} e^{A\eta_i\sigma} B\eta_i y_r(t - \varepsilon\sigma) \Big|_0^{(t-t_i)/\varepsilon} \\
&\quad - \int_0^{(t-t_i)/\varepsilon} A\eta_i^{-1} e^{A\eta_i\sigma} B\eta_i \frac{d}{d\sigma} (y_r(t - \varepsilon\sigma)) d\sigma
\end{aligned} \tag{3.69}$$

By simplifying the integration in (3.69)

$$\begin{aligned}
& \int_0^{(t-t_i)/\varepsilon} A_{\eta_i}^{-1} e^{A_{\eta_i} \sigma} B_{\eta_i} \frac{d}{d\sigma} (y_r(t - \varepsilon \sigma)) d\sigma \\
&= -\varepsilon A_{\eta_i}^{-2} e^{A_{\eta_i} \sigma} B_{\eta_i} \dot{y}_r(t - \varepsilon \sigma) \Big|_0^{(t-t_i)/\varepsilon} \\
&+ \int_0^{(t-t_i)/\varepsilon} \varepsilon^2 A_{\eta_i}^{-2} e^{A_{\eta_i} \sigma} B_{\eta_i} \frac{d^2}{d\sigma^2} (y_r(t - \varepsilon \sigma)) d\sigma \\
&= -\varepsilon A_{\eta_i}^{-2} e^{A_{\eta_i} (t-t_i)/\varepsilon} B_{\eta_i} \dot{y}_r(t_i) \\
&+ \varepsilon A_{\eta_i}^{-2} B_{\eta_i} \dot{y}_r(t) + O(\varepsilon^2)
\end{aligned} \tag{3.70}$$

Then we insert (3.70) in (3.69) to obtain

$$\begin{aligned}
& \int_0^{(t-t_i)/\varepsilon} e^{A_{\eta_i} \sigma} B_{\eta_i} y_r(t - \varepsilon \sigma) d\sigma \\
&= A_{\eta_i}^{-1} e^{A_{\eta_i} (t-t_i)/\varepsilon} B_{\eta_i} y_r(t_i) - A_{\eta_i}^{-1} B_{\eta_i} y_r(t) \\
&+ \varepsilon A_{\eta_i}^{-2} e^{A_{\eta_i} (t-t_i)/\varepsilon} B_{\eta_i} \dot{y}_r(t_i) - \varepsilon A_{\eta_i}^{-2} B_{\eta_i} \dot{y}_r(t) + O(\varepsilon^2)
\end{aligned} \tag{3.71}$$

Similarly, we can simplify the second integral in (3.68) to obtain

$$\begin{aligned}
& \varepsilon \int_0^{(t-t_i)/\varepsilon} e^{A_{\eta_i} \sigma} W \dot{y}_r(t - \varepsilon \sigma) d\sigma \\
&= \varepsilon A_{\eta_i}^{-1} e^{A_{\eta_i} (t-t_i)/\varepsilon} W \dot{y}_r(t_i) - \varepsilon A_{\eta_i}^{-1} W \dot{y}_r(t) \\
&+ \varepsilon^2 A_{\eta_i}^{-2} e^{A_{\eta_i} (t-t_i)/\varepsilon} W \dot{y}_r(t_i) - \varepsilon^2 A_{\eta_i}^{-2} W \dot{y}_r(t) + O(\varepsilon^3)
\end{aligned} \tag{3.72}$$

We then insert (3.71) and (3.72) into (3.68) to obtain

$$\begin{aligned}
\eta(t) &= e^{A\eta_i(t-t_i)/\varepsilon} \left(\eta(t_i) + A\eta_i^{-1} \gamma_i' + A\eta_i^{-1} B\eta_i y_r(t_i) \right. \\
&\quad \left. + \varepsilon A\eta_i^{-2} B\eta_i \dot{y}_r(t_i) - \varepsilon A\eta_i^{-1} W\dot{y}_r(t_i) - A\eta_i^{-1} \gamma_i' \right) \\
&\quad - A\eta_i^{-1} B\eta_i y_r(t) + \varepsilon A\eta_i^{-1} W\dot{y}_r(t) - \varepsilon A\eta_i^{-2} B\eta_i \dot{y}_r(t) + O(\varepsilon^2)
\end{aligned} \tag{3.73}$$

To obtain the initial value $\eta(t_i)$, we do not need to solve (3.73) by getting the accumulation around one cycle because we assume ε is small and the decaying within each segments makes the transients of $O(\varepsilon)$ order. Thus, initial values of the current segment, $i = i + n$, only depends on the driving terms of the previous segment, $i + n - 1$.

$$\begin{aligned}
\eta(t_i) &= e^{A\eta_{i+n-1}(t_i-t_{i+n-1})/\varepsilon} \left(\eta(t_{i+n-1}) + A\eta_{i+n-1}^{-1} \gamma_{i+n-1}' \right. \\
&\quad \left. + A\eta_{i+n-1}^{-1} B\eta_{i+n-1} y_r(t_{i+n-1}) + \varepsilon A\eta_{i+n-1}^{-2} B\eta_{i+n-1} \dot{y}_r(t_{i+n-1}) \right. \\
&\quad \left. - \varepsilon A\eta_{i+n-1}^{-1} W\dot{y}_r(t_{i+n-1}) \right) - A\eta_{i+n-1}^{-1} \gamma_{i+n-1}' \\
&\quad - A\eta_{i+n-1}^{-1} B\eta_{i+n-1} y_r(t_i) - \varepsilon A\eta_{i+n-1}^{-2} B\eta_{i+n-1} \dot{y}_r(t_i) \\
&\quad + \varepsilon A\eta_{i+n-1}^{-1} W\dot{y}_r(t_i) + O(\varepsilon^2)
\end{aligned} \tag{3.74}$$

Now by ignoring the term in the parenthesis in (3.74) and substituting the remaining term of $\eta(t_i)$ into (3.73), we obtain

$$\begin{aligned}
\eta(t) &= \psi - A\eta_i^{-1} \gamma_i' - A\eta_i^{-1} B\eta_i y_r(t) \\
&\quad + \varepsilon A\eta_i^{-1} W\dot{y}_r(t) - \varepsilon A\eta_i^{-2} B\eta_i \dot{y}_r(t) + O(\varepsilon^2)
\end{aligned} \tag{3.75}$$

where,

$$\begin{aligned}
\psi &= e^{A\eta_i(t-t_i)/\varepsilon} \left(-A_{\eta_{i+n-1}}^{-1} \gamma'_{i+n-1} - A_{\eta_{i+n-1}}^{-1} B_{\eta_{i+n-1}} y_r(t_i) \right. \\
&\quad + \varepsilon A_{\eta_{i+n-1}}^{-1} W \dot{y}_r(t_i) - \varepsilon A_{\eta_{i+n-1}}^{-2} B_{\eta_{i+n-1}} \dot{y}_r(t_i) + A_{\eta_i}^{-1} \gamma'_i \\
&\quad \left. + A_{\eta_i}^{-1} B_{\eta_i} y_r(t_i) - \varepsilon A_{\eta_i}^{-1} W \dot{y}_r(t_i) + \varepsilon A_{\eta_i}^{-2} B_{\eta_i} \dot{y}_r(t_i) \right) \quad (3.76)
\end{aligned}$$

The term ψ is bounded as follows; First, the highest value happens in the beginning of each segment i at time $t = t_i$, which makes the exponential term equals to one. Second, we assume $|\Delta m| < m$. With this assumption the terms which are function of y_r or \dot{y}_r cancel out because every term has a similar term with opposite sign and close to it in value. The contribution of remaining term, $A_{\eta_i}^{-1} \gamma'_i - A_{\eta_{i+n-1}}^{-1} \gamma'_{i+n-1}$ to the tracking error is calculated by multiplying it by A_{12} . This results in $H_i \gamma'_i - H_{i+n-1} \gamma'_{i+n-1}$. Looking back to simplifications of these terms from (3.62), we require that the gain K_P be high enough to reduce the value of $|m_i \Delta \gamma_i - \gamma_i \Delta m_i|$.

Then for all segments, the bound $|\psi|_{\max}$ is approximated by

$$|\psi|_{\max} \leq |H_i \gamma'_i - H_{i+n-1} \gamma'_{i+n-1}|_{\max} \quad (3.77)$$

Using $y_r = A_C \sin(\omega t)$ in (3.29) and including the subscript i for the parameters, we have the expression of η for the time from t_i to t_{i+1}

$$\begin{aligned}
\eta &= \psi - A_{\eta,i}^{-1} B_{\eta,i} A_C \sin(\omega t) - A_{\eta,i}^{-1} \gamma'_i + \varepsilon (A_{\eta,i}^{-1} W \\
&\quad - A_{\eta,i}^{-2} B_{\eta,i}) A_C \omega \cos(\omega t) + O(\varepsilon^2) \quad (3.78)
\end{aligned}$$

3.5.6 Calculating the Bound on the Frequency-dependent Term of the Error

To determine the upper bound on the third term $\varepsilon(H_i A_{22,i}^{-1} B_{2,i}) \omega_{A_c}$ of (3.38), we replace H_i by $A_{12} A_{22,i}^{-1}$ and $B_{2,i}$ by $B \beta_2$, where $\beta_2 = \frac{m_i + \Delta m_i}{m_i} (g + kp)$. We also replace $A_{22,i}^{-1}$ by $A - B \beta_1 C$, where $\beta_1 = \frac{m_i + \Delta m_i}{m_i} kp$ and simplify the expressions

$$\begin{aligned} H_i A_{22,i}^{-1} B_{2,i} &= A_{12} A_{22,i}^{-2} B_{2,i} \\ &= - \left[CA^{-2} B + CA^{-2} (BC)^2 A^{-2} B \left(\frac{\beta_1}{1 + h\beta_1} \right)^2 \right. \\ &\quad \left. + 2CA^{-2} B \left(\frac{\beta_1}{1 + h\beta_1} \right) CA^{-1} B \right] \beta_2 \end{aligned} \quad (3.79)$$

Because C is a row vector and B is a column vector, the multiplications of all the matrices in (3.79) are scalar quantities. let us denote them by q_1 , q_2 and q_3 and replace β_1 and β_2 by their expressions.

$$\begin{aligned} H_i A_{22,i}^{-1} B_{2,i} &= - \left[q_1 + q_2 \left(\frac{(m_i + \Delta m_i) kp}{m_i + kp(m_i + \Delta m_i)h} \right)^2 \right. \\ &\quad \left. + q_3 \left(\frac{(m_i + \Delta m_i) kp}{m_i + kp(m_i + \Delta m_i)h} \right) \right] \frac{m_i + \Delta m_i}{m_i} (g + kp) \end{aligned} \quad (3.80)$$

Let us denote the bound on $H_i A_{22,i}^{-1} B_{2,i}$ by $(H A_{22}^{-1} B_2)_{\max}$ for all segments. This is obtained by substituting the largest slope m_{\max} and uncertainty $|\Delta m|_{\max}$ in the numerator and the smallest

m_{\min} in the denominator of (3.80)

$$\begin{aligned}
(HA_{22}^{-1}B_2)_{\max} = & -\frac{m_{\max} + |\Delta m|_{\max}}{m_{\min}}(g + k_p) [q_1 \\
& + q_2 \left(\frac{(m_{\max} + |\Delta m|_{\max})k_p}{m_{\min}(1 + k_ph)} \right)^2 \\
& + q_3 \left(\frac{(m_{\max} + |\Delta m|_{\max})k_p}{m_{\min}(1 + k_ph)} \right)] \quad (3.81)
\end{aligned}$$

We notice from (3.80), in the case when $|\Delta m_i| \ll m_i$ such that we can ignore $|\Delta m_i|$, Eq. (3.80) becomes independent of the slopes and uncertainties. In this case the term of $H_i A_{22,i}^{-1} B_{2,i}$ becomes constant through all the segments.

3.6 Summary

Hysteresis nonlinearity is affecting the overall tracking performance of many applications. Analysis of tracking error is important for understanding different factors that can affect its behavior. In this Chapter, we analyzed a closed-loop system involving hysteresis inversion, proportional-integral feedback control, and a constant-gain feedforward element. Some researchers in the literature use optimization [49], neural networks [61], or trial-and-error to determine both k_i and k_p Depending on the uncertainties on the operator parameters. In this work we found criteria for choosing those gains. For instance, the ratio k_i/k_p should be high to guarantee good performance, which agrees with the results in [49, 61]. Singular perturbation analysis was used in order to separate the fast dynamics of the plant from slow dynamics of the controller. The analysis quantifies the effect of the reference frequency on the tracking performance, which is important in applications such as high-speed nanopositioning. Simulation results were compared with the calculated ones based on the analytical expressions. The agreement between the simulation and analytical

results provides support for the analysis. Experimental results further strengthens the validity of the analysis.

Table 3.1: Simulation, analytical, and experimental results on maximum tracking errors in μm for a system involving a perturbed PI-operator and a second-order plant.

frequency	Simulation Max $ e(t) $	Analytical Max $ e(t) $	φ Max $ \varphi $
1 Hz	0.177	0.26	0.019
10 Hz	0.375	0.57	0.009
20 Hz	0.38	0.58	0.004
50 Hz	0.39	0.586	0.001
80 Hz	0.41	0.592	3×10^{-4}
100 Hz	0.42	0.597	5×10^{-5}
150 Hz	0.475	0.61	2.6×10^{-4}
200 Hz	0.53	0.63	4.2×10^{-4}
400 Hz	0.82	0.77	6.9×10^{-4}
600 Hz	1.2	0.95	7.3×10^{-4}
800 Hz	1.66	1.16	7.7×10^{-4}
1000 Hz	2.2	1.38	7.9×10^{-4}

Table 3.2: Experimental results on maximum tracking errors in μm with and without feedforward compensation.

frequency	With feedforward Max $ e(t) $	Without feedforward Max $ e(t) $
1 Hz	0.02	0.025
10 Hz	0.04	0.2
20 Hz	0.045	0.38
50 Hz	0.08	0.8
80 Hz	0.11	1.4
100 Hz	0.12	1.7
150 Hz	0.32	2.2
200 Hz	0.6	3.0

Chapter 4

Sliding Mode Control Design

4.1 Introduction

In this chapter, we present a Sliding-Mode control (SMC) scheme for tracking of systems with hysteresis. SMC is attractive because of its robustness against disturbances and parameter uncertainties [75]. Some existing works on the SMC methods for piezo-actuated systems incorporate hysteresis inversion to reduce the amount of uncertainty introduced by hysteresis [56, 57], while others do not [76, 58]. In our work, we will integrate the inversion control with SMC control as presented in the general form in Fig. 4.1.

In many SMC designs, the control signal has two components, the switching control, which is in the form of $\beta \operatorname{sgn}(\cdot)$ and the equivalent control. The switching control is used to dominate the disturbances while the equivalent control is used to compensate for the known terms. Existing work [76, 56, 57, 58, 59] typically uses a constant coefficient β for the switching function. Furthermore, no systematic approaches have been given for deriving such coefficients. In contrast to existing work, the switching component of the controller in our work is obtained by using an upper bound on the inversion error, computed based on the estimate of uncertainties in the hysteresis model and the control signal. The control signal is time-dependent and varies with the positioning range. This allows implementation with a coefficient which is self-adjusting.

In this chapter we provide analysis of the tracking error for a k^{th} order system. To avoid con-

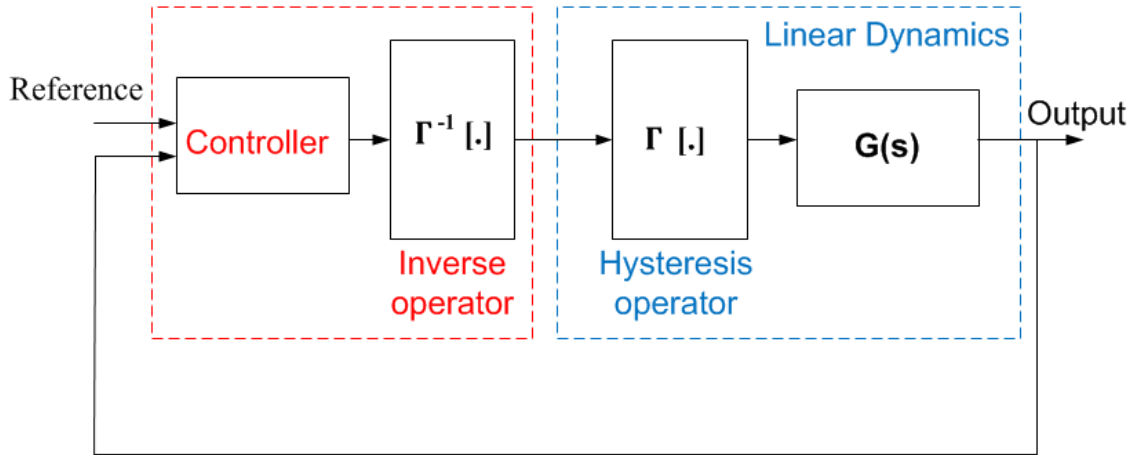


Figure 4.1: A general control framework for systems preceded by hysteresis.

trol chattering, the sliding mode control is implemented with the signum function replaced by a high-slope saturation function, which acts as a high gain feedback in a boundary layer around the switching surface. We analyze the trajectories inside the boundary layer. By design, the coefficients of the sliding surface have different orders of magnitude such that the resulting system has a multi-time-scale structure inside the boundary layer. We derive an analytical expression for the tracking error at the steady state under periodic references and provide insight as to how the error depends on the hysteresis uncertainties, reference frequency, and the controller parameters.

We have conducted simulation and experiments to validate the proposed SMC approach. In simulation, we show that the proposed scheme is able to track successfully “irregular” references, for different levels of parameter uncertainties. We also simulate the system with sinusoidal inputs and show that tracking error inside the boundary layer increases with frequency at a low frequency range then it remains constant in a mid-range after which it decreases until the resonance frequency, where it starts to increase again. We also show that it is better to use a control that includes switching and equivalent control rather than to use only switching component. We present results on the effect of the switching component amplitude and the boundary layer size on the performance. Ex-

perimental results on the tracking control of a commercially available nanopositioner show close qualitative behavior to the simulation, particularly when a rate limiter is added to the simulated system. Experimental results also demonstrate that the presented SMC approach delivers performance comparable to that of servocompensation [54] for sinusoidal references.

4.2 Controller Design

For a general discussion, we consider a plant with linear dynamics of order k . The linear dynamics are given by;

$$\begin{aligned}\dot{x}_j &= x_{j+1}, \quad 1 \leq j \leq k-1 \\ \dot{x}_k &= -a_{k-1}x_k - a_{k-2}x_{k-1} - \cdots - a_0x_1 + a_0(u_d + d)\end{aligned}\quad (4.1)$$

where $x_1 = y$ denotes the position. The parameters a_0, a_1, \dots, a_{k-1} are positive. The tracking error e_1 is defined as

$$e_1 = y - y_r = x_1 - y_r \quad (4.2)$$

A bound on the inversion error can be obtained from (2.10) as

$$|d| \leq k_1 + k_0 |u_d| \quad (4.3)$$

where $\frac{|\Delta m_{max}|}{|m_{min}|} \leq k_0$ and $|\Delta_{dc,max}| \leq k_1$. To eliminate the DC error at the steady state, we add an integrator, the state of which is e_0 , defined via $\dot{e}_0 = e_1$. Then (4.1) can be written in terms of

the error as

$$\begin{aligned}
\dot{e}_0 &= e_1 \\
\dot{e}_j &= e_{j+1}, \quad 1 \leq j \leq k-1 \\
\dot{e}_k &= -a_{k-1}(e_k + y_r^{(k-1)}) - \dots - a_0(e_1 + y_r) + a_0(u_d + d) - y_r^{(k)}
\end{aligned} \tag{4.4}$$

The sliding surface s is designed in terms of the error

$$s = e_k + \sigma_{k-1}e_{k-1} + \dots + \sigma_1e_1 + \sigma_0e_0 \tag{4.5}$$

The coefficients $\sigma_0, \sigma_1, \dots, \sigma_{k-1}$ are chosen such that the polynomial $\lambda^k + \sigma_{k-1}\lambda^{k-1} + \dots + \sigma_0$ is Hurwitz. To obtain \dot{s} , we differentiate both sides of (4.5), substitute \dot{e}_k from (4.4), and arrange terms

$$\dot{s} = (\sigma_{k-1} - a_{k-1})e_k + \dots + (\sigma_0 - a_0)e_1 - a_{k-1}y_r^{(k-1)} - \dots - a_0y_r + a_0(u_d + d) - y_r^{(k)} \tag{4.6}$$

The control, u_d , which is composed of two component u_{eq} and u_s , can then be chosen such that u_{eq} eliminates all terms in (4.6) except for the uncertainty d , which is compensated by u_s .

$$u_{eq}(t, e) = \frac{1}{a_0} [(a_{k-1} - \sigma_{k-1})e_k + \dots + (a_0 - \sigma_0)e_1 + a_{k-1}y_r^{(k-1)} + \dots + a_0y_r + y_r^{(k)}] \tag{4.7}$$

Now, we may write the control u_d as the sum of an equivalent component u_{eq} and switching component u_s control

$$u_d = u_{eq} + u_s \quad (4.8)$$

where,

$$u_s = -\beta \text{sgn}(s) \quad (4.9)$$

By inserting (4.8) into (4.3), we can write the bound on d as

$$\begin{aligned} |d(t)| &\leq k_1 + k_0 |u_s(t) + u_{eq}(t, e)| \\ &\leq k_1 + k_0 |u_s(t)| + k_0 |u_{eq}(t, e)| \end{aligned} \quad (4.10)$$

Define

$$\phi(|u_{eq}(t, e)|) = k_1 + k_0 |u_{eq}(t, e)| \quad (4.11)$$

which implies

$$|d(t)| \leq \phi(|u_{eq}(t, e)|) + k_0 |u_s(t)| \quad (4.12)$$

Substituting (4.7) and (4.8) in (4.6), we obtain

$$\dot{s} = a_0 (d(t) + u_s(t)) \quad (4.13)$$

For the stability analysis, we define a Lyapunov function $V = \frac{1}{2}s^2$. Then by taking the derivative of V , we obtain

$$\begin{aligned}\dot{V} &= s\dot{s} = a_0s(d(t) + u_s(t)) \\ &\leq a_0(|s(t)||d(t)| + s(t)u_s(t))\end{aligned}\tag{4.14}$$

Now we substitute the bound on d into (4.14)

$$\begin{aligned}\dot{V} &\leq a_0(|s|[\phi(|u_{eq}(t,e)|) + k_0|u_s|] + su_s) \\ &\leq a_0(|s|[\phi(|u_{eq}(t,e)|) + k_0\beta] - \beta|s|) = a_0(-[1 - k_0]\beta + \phi(|u_{eq}|))|s|\end{aligned}\tag{4.15}$$

$$\phi(|u_{eq}(t,e)|) = k_1 + k_0|u_{eq}(t,e)|\tag{4.16}$$

Therefore $\dot{V} < 0$ for

$$\beta > \frac{\phi(|u_{eq}(t,e)|)}{1 - k_0}\tag{4.17}$$

Following the discussions in Chapter 2, we assume $0 \leq k_0 < 1$. The coefficient β is chosen as $\beta(t,e) \geq \frac{\phi(|u_{eq}(t,e)|)}{1 - k_0} + b_0$, where b_0 is a small positive number. By selecting β in this way we guarantee that any trajectory starting away from the surface $s = 0$ reaches it in finite time.

With the signum function in the switching controller (4.9), the error would asymptotically converge to zero. The signum function, however, results in chattering in practice. Therefore, we replace the signum function with the saturation function given by

$$u_s = -\beta \text{sat}(s/\mu)\tag{4.18}$$

where μ determines the size of the boundary layer $|s| \leq \mu$.

To analyze the performance of the control with the switching component (4.18), we examine the derivative of the Lyapunov function $V = \frac{1}{2}s^2$ outside the boundary layer.

Plugging (4.18) into the first inequality (4.15), we have

$$\dot{V} \leq a_0(|s|[\phi(|u_{eq}(t, e)|) + k_0] - \beta \text{sat}(s/\mu)) - \beta s \text{sat}(s/\mu) \quad (4.19)$$

Then for $|s| \geq \mu$, we get

$$\dot{V} \leq a_0(-[1 - k_0]\beta + \phi(|u_{eq}|))|s| \quad (4.20)$$

Thus, with the same $\beta(t, e)$ in (4.17), $|s|$ will decrease until it enters the boundary layer $|s| \leq \mu$ in finite time and never leaves it thereafter.

Another way to design the control is to use a constant β . This requires us to limit the system variables to the compact set $\Omega = \{\eta^T P \eta \leq c_1\} \times \{|s| \leq c_2\}$, where $\eta = [e_0 \ e_1 \ \cdots \ e_{k-1}]$, $\dot{\eta} = A\eta + Bs$, c_1 and c_2 are constants and P is the solution of the Lyapunov equation $PA + A^T P = -I$. For more details refer to [73].

4.2.1 System Scaling

When the linear dynamics have a large bandwidth, as in the nanopositioner that will be used later in the simulation and experiments, it is beneficial to normalize the model. We show this for a second-order-system, which can be readily generalized for higher-order ones. With ω_n as the natural frequency of the system, we have $a_0 = \omega_n^2$ and $a_1 = 2\zeta\omega_n$. The augmented integral

control $\dot{e}_0 = e_1$. The closed-loop system is given by

$$\begin{aligned}
\dot{e}_0 &= e_1 \\
\dot{e}_1 &= e_2 \\
\dot{e}_2 &= -a_1(e_2 + \dot{y}_r) - a_0(e_1 + y_r) + a_0(u_d + d) - \ddot{y}_r
\end{aligned} \tag{4.21}$$

For scaling the system we apply the change of variables $\tau = \omega_n t$, $z_0 = e_0 \omega_n$, $z_1 = e_1$, and $z_2 = \frac{e_2}{\omega_n}$.

This will result in a transformed system

$$\begin{aligned}
\frac{d z_0}{d \tau} &= z_1 \\
\frac{d z_1}{d \tau} &= z_2 \\
\frac{d z_2}{d \tau} &= -2\zeta z_2 - z_1 + u_d + d - \frac{1}{\omega_n}(\ddot{y}_r + 2\zeta \omega_n \dot{y}_r + \omega_n^2 y_r)
\end{aligned} \tag{4.22}$$

Now for the transformed system, with the surface chosen as $s = z_2 + \check{\sigma}_1 z_1 + \check{\sigma}_0 z_0$ and for a boundary layer constant $\check{\mu}$, the switching component of the control is

$$u_s = -\beta \operatorname{sat}\left(\frac{s}{\check{\mu}}\right) = -\beta \operatorname{sat}\left(\frac{z_2 + \check{\sigma}_1 z_1 + \check{\sigma}_0 z_0}{\check{\mu}}\right) \tag{4.23}$$

Then we substitute the original coordinates in (4.23) to obtain

$$\begin{aligned}
u_s &= -\beta \operatorname{sat}\left(\frac{e_2 + \check{\sigma}_1 \omega_n e_1 + \check{\sigma}_0 \omega_n^2 e_0}{\check{\mu} \omega_n}\right) \\
&= -\beta \operatorname{sat}\left(\frac{e_2 + \sigma_1 e_1 + \sigma_0 e_0}{\mu}\right)
\end{aligned} \tag{4.24}$$

From (4.24), we can see that the parameters of the sliding surface for the non-scaled system are related to those of the scaled one as $\sigma_0 = \check{\sigma}_0 \omega_n^2$, $\sigma_1 = \check{\sigma}_1 \omega_n$, and $\mu = \check{\mu} \omega_n$. This makes the choice of non-scaled parameters in the order of ω_n as we will see in the simulation and experimental sections.

4.3 Determining the tracking error inside the boundary layer

In this section we investigate the tracking error inside the boundary layer when β is constant. Inside the boundary layer $|s| < \mu$, $\beta \text{sat}(s/\mu) = \frac{\beta s}{\mu}$. To find an expression for $\dot{e} = [e_0 \ e_1 \ \dots \ e_k]^T$ inside the boundary layer, we insert d from (2.10) into \dot{e}_k of (4.4), substitute both u_{eq} and $u_s = \frac{-\beta s}{\mu}$ into \dot{e}_k , and simplify terms. Note that the differential equations are given for any segment $i = 1, 2, \dots, l$ in the hysteresis-loop and l is the number of segments.

$$\begin{aligned}
\dot{e}_k = & \left[\left(1 + \frac{\Delta m_i}{m_i}\right) \left(\frac{-a_0 \beta}{\mu} - \sigma_{k-1}\right) + a_{k-1} \frac{\Delta m_i}{m_i} \right] e_k + \left[\left(1 + \frac{\Delta m_i}{m_i}\right) \left(\frac{-a_0 \beta \sigma_{k-1}}{\mu} - \sigma_{k-2}\right) \right. \\
& + a_{k-2} \frac{\Delta m_i}{m_i} \left. \right] e_{k-1} + \dots + \left[\left(1 + \frac{\Delta m_i}{m_i}\right) \left(\frac{-a_0 \beta \sigma_1}{\mu} - \sigma_0\right) + a_0 \frac{\Delta m_i}{m_i} \right] e_1 + a_0 \Delta \gamma_i \\
& + \left[\left(1 + \frac{\Delta m_i}{m_i}\right) \left(\frac{-a_0 \beta}{\mu} \sigma_0\right) \right] e_0 + \frac{\Delta m_i}{m_i} y_r^{(k)} + a_{k-1} \frac{\Delta m_i}{m_i} y_r^{(k-1)} + \dots + a_1 \frac{\Delta m_i}{m_i} \dot{y}_r + a_0 \frac{\Delta m_i}{m_i} y_r
\end{aligned} \tag{4.25}$$

We divide both sides of \dot{e}_k of (4.25) by $\frac{a_0 \beta}{\mu}$. Then we combine small coefficients other than σ 's which are multiplied by the states e_1, \dots, e_k and denote them by $\delta_k, \delta_{k-1}, \dots, \delta_1$. Eq. (4.25) can

then be written in the form

$$\begin{aligned} \varepsilon_k \dot{e}_k = & \left(1 + \frac{\Delta m_i}{m_i}\right) \left[-(1 + \delta_k) e_k - (\sigma_{k-1} + \delta_{k-1}) e_{k-1} - \dots - (\sigma_1 + \delta_1) e_1 - \sigma_0 e_0 \right] \\ & + \frac{\mu}{\beta} \Delta \gamma_i + \frac{\Delta m_i}{m_i} \frac{\mu}{\beta} \left(\frac{y_r^{(k)}}{a_0} + \frac{a_{k-1}}{a_0} y_r^{(k-1)} + \dots + \frac{a_1}{a_0} \dot{y}_r + y_r \right) \end{aligned} \quad (4.26)$$

where $\varepsilon_k = \frac{\mu}{a_0 \beta}$. Define $\lambda = \frac{\sigma_0}{\sigma_1 + \delta_1}$. In order to solve the differential equations of the system, we have the following assumptions:

1) For the system to be represented in singularly perturbed multi-time-scale structure we require that $\varepsilon_k \ll \varepsilon_{k-1} \ll \dots \ll \varepsilon_1 \ll \frac{1}{\lambda}$, which satisfy the inequality $\frac{\mu}{a_0 \beta} \ll \frac{1 + \delta_k}{\sigma_{k-1} + \delta_{k-1}} \ll \dots \ll \frac{1 + \delta_2}{(\sigma_1 + \delta_1)} \ll \frac{\sigma_1 + \delta_1}{\sigma_0}$.

2) The magnitude of the slope uncertainty in each segment i is smaller than the slope itself, $|\Delta m_i| < |m_i|$. This assumption implies that the segment slopes of the perturbed operator are positive.

By nested application of the singular perturbation method [74], we approximate the tracking error e_1 . This process is shown below by an example of a second-order system.

4.3.1 Example of the Second Order System

Let $k = 2$. By using Eq. (4.26), the singularly perturbed closed-loop system is given by

$$\begin{aligned}
 \dot{e}_0 &= e_1 \\
 \dot{e}_1 &= e_2 \\
 \varepsilon_2 \dot{e}_2 &= (1 + \frac{\Delta m_i}{m_i})[-(1 + \delta_2)e_2 - (\sigma_1 + \delta_1)e_1 - \sigma_0 e_0] + \frac{\mu}{\beta} \Delta_{dc,i} + \frac{\Delta m_i}{m_i} \frac{\mu}{\beta} (\frac{\ddot{y}_r}{a_0} + \frac{a_1}{a_0} \dot{y}_r + y_r)
 \end{aligned} \tag{4.27}$$

Set $\varepsilon_2 = 0$ and use the following equation to eliminate e_2 from the \dot{e}_1 equation.

$$(1 + \delta_2)e_2 = -(\sigma_1 + \delta_1)e_1 - \sigma_0 e_0 + \frac{\mu}{\beta} \frac{m_i \Delta_{dc,i}}{m_i + \Delta m_i} + \frac{\Delta m_i}{m_i + \Delta m_i} \frac{\mu}{\beta} (\frac{\ddot{y}_r}{a_0} + \frac{a_1}{a_0} \dot{y}_r + y_r) \tag{4.28}$$

With the assumption $\varepsilon_1 \ll \frac{1}{\lambda}$, the reduced system can be presented as a singularly perturbed system again by multiplying (4.28) with $1/(\sigma_1 + \delta_1)$ and taking $\varepsilon_1 = (1 + \delta_2)/(\sigma_1 + \delta_1)$,

$$\begin{aligned}
 \dot{e}_0 &= e_1 \\
 \varepsilon_1 \dot{e}_1 &= -e_1 - \frac{\sigma_0}{\sigma_1 + \delta_1} e_0 + \frac{\mu}{(\sigma_1 + \delta_1)\beta} \frac{m_i \Delta_{dc,i}}{m_i + \Delta m_i} + \frac{\mu}{(\sigma_1 + \delta_1)\beta} \frac{\Delta m_i}{m_i + \Delta m_i} (\frac{\ddot{y}_r}{a_0} + \frac{a_1}{a_0} \dot{y}_r + y_r)
 \end{aligned} \tag{4.29}$$

By setting $\varepsilon_1 = 0$, we get

$$e_1 = -\frac{\sigma_0}{(\sigma_1 + \delta_1)} e_0 + \frac{\mu}{(\sigma_1 + \delta_1)\beta} \frac{m_i \Delta_{dc,i}}{m_i + \Delta m_i} + \frac{\mu}{(\sigma_1 + \delta_1)\beta} \frac{\Delta m_i}{m_i + \Delta m_i} (\frac{\ddot{y}_r}{a_0} + \frac{a_1}{a_0} \dot{y}_r + y_r) \tag{4.30}$$

Since $e_0 = e_1$, at this point we arrive at a scalar differential equation in one variable e_0 , which can be solved to get e_0 and then we plug the solution in (4.30) to obtain the tracking error expression.

We can follow the procedure in this example for a k -th order system. In that case, we have $\varepsilon_k = \frac{\mu}{a_0\beta}$, $\varepsilon_{k-1} = \frac{1+\delta_k}{\sigma_{k-1}+\delta_{k-1}}$, \dots , $\varepsilon_1 = \frac{1+\delta_2}{(\sigma_1+\delta_1)}$. The tracking error $e_1 = \dot{e}_0$ is given by

$$\begin{aligned} \dot{e}_0 = & -\frac{\sigma_0}{\sigma_1 + \delta_1} e_0 + \frac{\mu}{(\sigma_1 + \delta_1)\beta} \frac{m_i \Delta d_{c,i}}{m_i + \Delta m_i} \\ & + \frac{\mu}{(\sigma_1 + \delta_1)\beta} \frac{\Delta m_i}{m_i + \Delta m_i} \left(\frac{y_r^{(k)}}{a_0} + \frac{a_{k-1}}{a_0} y_r^{(k-1)} + \dots + \frac{a_1}{a_0} \dot{y}_r + y_r \right) \end{aligned} \quad (4.31)$$

Note that the solution of (4.31) only depends on σ_0 and σ_1 while the higher parameters of the surface $\geq \sigma_2$ are not part of the equation because they are part of the fast transient of the original system which is approximated using singular perturbation method. The above steps show how we obtain e_0 for a given hysteresis segment i . In order to accommodate the effect of traversing from one segment to another, we follow the procedure described below, where we consider a sinusoidal reference for ease of presentation.

4.3.2 Tracking Error for a Sinusoidal Reference

In order to discuss how the error scales with frequency, a sinusoidal reference $y_r = A_C \sin(\omega t)$ is applied to the system. We assume that the solution of the closed-loop system converges to a periodic function with the same period T of the reference input. This assumption is reasonable in view of the simulation and experimental results in this work and also in [53, 55, 56, 1, 57].

The idea of getting a solution that shows the impact of all hysteresis segments on each other is explained by the following steps, which are analogous to those for analyzing a proportional-

integral-controlled system discussed in chapter 3. We start by solving (4.31) for the segment i with initial value $e_0(t_i)$, where $i = 1, \dots, l$ and l is the number of segments of a hysteresis-loop at the steady state. The final value of this segment $e_0(t_{i+1})$ will be inserted as the initial value for the following segment $i + 1$. We continue this process around one cycle until we get $e_0(t_i + T)$. The periodicity of the solution implies that $e_0(t_i + T) = e_0(t_i)$ and this allows us to obtain an expression for $e_0(t_i)$. We substitute the solution of $e_0(t)$ in (4.31) to obtain $e_1(t)$, $t_i \leq t < t_{i+1}$. A sinusoidal reference $y_r = A_c \sin \omega t$ is inserted in (4.31) to get

$$\dot{e}_0 = -\lambda_i e_0 + \mathcal{K}_i + \mathcal{M}_i \sin \omega t + \mathcal{N}_i \cos \omega t = e_1 \quad (4.32)$$

Without loss of generality, we can take the dimension of the linear dynamics k as an even number, which is common in linear systems with complex modes. From 4.31, we have $\lambda_i = \frac{\sigma_0}{\sigma_1 + \delta_1}$, $\mathcal{K}_i = \frac{\mu}{(\sigma_1 + \delta_1)\beta} \frac{m_i \Delta dc_i}{m_i + \Delta m_i}$, $\mathcal{M}_i = \frac{\mu A_c}{(\sigma_1 + \delta_1)\beta} \frac{\Delta m_i}{m_i + \Delta m_i} (1 - \frac{a_2}{a_0} \omega^2 + \dots \frac{\omega^k}{a_0})$ and $\mathcal{N}_i = \frac{\mu A_c}{(\sigma_1 + \delta_1)\beta} \frac{\Delta m_i}{m_i + \Delta m_i} (\frac{a_1}{a_0} \omega - \frac{a_3}{a_0} \omega^3 + \dots \frac{a_{k-1}}{a_0} \omega^{k-1})$. Note that if k is an odd number we only need to redefine the quantities \mathcal{M}_i and \mathcal{N}_i . The solution of the first-order equation (4.32) is

$$\begin{aligned} e_0(t) = & e^{-\lambda_i(t-t_i)} e_0(t_i) + \frac{\mathcal{K}_i}{\lambda_i} [1 - e^{-\lambda_i(t-t_i)}] + \frac{\mathcal{M}_i}{\lambda_i^2 + \omega^2} [(\lambda_i \sin \omega t - \omega \cos \omega t) \\ & - e^{\lambda_i(t-t_i)} (\lambda_i \sin \omega t_i - \omega \cos \omega t_i)] + \frac{\mathcal{N}_i}{\lambda_i^2 + \omega^2} [(\lambda_i \cos \omega t + \omega \sin \omega t) \\ & - e^{-\lambda_i(t-t_i)} (\lambda_i \cos \omega t_i + \omega \sin \omega t_i)] \end{aligned} \quad (4.33)$$

To simplify expressions, let us define the quantities

$$\rho_i = \frac{\mathcal{K}_i}{\lambda_i} [1 - e^{-\lambda_i(t_{i+1}-t_i)}]$$

$$\Omega_i = \frac{\mathcal{M}_i}{\lambda_i^2 + \omega^2} [(\lambda_i \sin \omega t_{i+1} - \omega \cos \omega t_{i+1}) - e^{-\lambda_i(t_{i+1}-t_i)}(\lambda_i \sin \omega t_i - \omega \cos \omega t_i)]$$

$$\varpi_i = \frac{\mathcal{N}_i}{\lambda_i^2 + \omega^2} [(\lambda_i \cos \omega t_{i+1} + \omega \sin \omega t_{i+1}) - e^{-\lambda_i(t_{i+1}-t_i)}(\lambda_i \cos \omega t_i + \omega \sin \omega t_i)]$$

The final value of the error $e_0(t_{i+1})$ at the segment i can be calculated by replacing t by t_{i+1} in (4.33). Then the obtained expression is used as an initial value for the segment $i + 1$ for the time $t_{i+1} < t < t_{i+2}$.

$$e_0(t_{i+1}) = e^{-\lambda_i(t_{i+1}-t_i)} e_0(t_i) + \rho_i + \Omega_i + \varpi_i \quad (4.34)$$

By following the same procedure, at $t = t_{i+2}$ we get

$$e_0(t_{i+2}) = e^{-\lambda_{i+1}(t_{i+2}-t_{i+1})} e^{-\lambda_i(t_{i+1}-t_i)} e_0(t_i) + e^{-\lambda_{i+1}(t_{i+2}-t_{i+1})} [\rho_i + \Omega_i + \varpi_i] \\ + \rho_{i+1} + \Omega_{i+1} + \varpi_{i+1} \quad (4.35)$$

at $t = t_{i+l}$, the error $e_0(t_{i+l})$ can be written as

$$\begin{aligned}
e_0(t_{i+l}) &= e^{-\lambda_{i+l-1}(t_{i+l}-t_{i+l-1})} \dots e^{-\lambda_i(t_{i+1}-t_i)} e_0(t_i) \\
&\quad + e^{-\lambda_{i+l-1}(t_{i+l}-t_{i+l-1})} \dots e^{-\lambda_{i+1}(t_{i+2}-t_{i+1})} [\rho_i + \Omega_i + \varpi_i] \\
&\quad + \dots \\
&\quad + e^{-\lambda_{i+l-1}(t_{i+l}-t_{i+l-1})} [\rho_{i+l-2} + \Omega_{i+l-2} + \varpi_{i+l-2}] \\
&\quad + \rho_{i+l-1} + \Omega_{i+l-1} + \varpi_{i+l-1} \\
&= e_0(t_i)
\end{aligned} \tag{4.36}$$

We obtain $e_0(t_i)$ from (4.36)

$$\begin{aligned}
e_0(t_i) &= \frac{1}{1-M} \left[e^{-\lambda_{i+l-1}(t_{i+l}-t_{i+l-1})} \dots e^{-\lambda_{i+1}(t_{i+2}-t_{i+1})} [\rho_i + \Omega_i + \varpi_i] \right. \\
&\quad + \dots \\
&\quad + e^{-\lambda_{i+l-1}(t_{i+l}-t_{i+l-1})} [\rho_{i+l-2} + \Omega_{i+l-2} + \varpi_{i+l-2}] \\
&\quad \left. + \rho_{i+l-1} + \Omega_{i+l-1} + \varpi_{i+l-1} \right]
\end{aligned} \tag{4.37}$$

where $M = e^{-\lambda_{i+l-1}(t_{i+l}-t_{i+l-1})} \dots e^{-\lambda_i(t_{i+1}-t_i)}$. Then, we plug (4.37) into (4.33) and

arrange terms to get

$$\begin{aligned}
e_0(t) &= \frac{e^{-\lambda_i(t-t_i)}}{1-M} \left[e^{-\lambda_{i+l-1}(t_{i+l}-t_{i+l-1})} \dots e^{-\lambda_{i+1}(t_{i+2}-t_{i+1})} (\rho_i + \Omega_i + \varpi_i) \right. \\
&+ \dots \\
&+ e^{-\lambda_{i+l-1}(t_{i+l}-t_{i+l-1})} (\rho_{i+l-2} + \Omega_{i+l-2} + \varpi_{i+l-2}) \\
&+ \rho_{i+l-1} + \Omega_{i+l-1} + \varpi_{i+l-1} \left. \right] + \frac{\mathcal{K}_i}{\lambda_i} [1 - e^{-\lambda_i(t-t_i)}] + \frac{\mathcal{M}_i}{\lambda_i^2 + \omega^2} [(\lambda_i \sin \omega t - \omega \cos \omega t) \\
&- e^{-\lambda_i(t-t_i)} (\lambda_i \sin \omega t_i - \omega \cos \omega t_i)] + \frac{\mathcal{N}_i}{\lambda_i^2 + \omega^2} [(\lambda_i \cos \omega t + \omega \sin \omega t) \\
&- e^{-\lambda_i(t-t_i)} (\lambda_i \cos \omega t_i + \omega \sin \omega t_i)] \tag{4.38}
\end{aligned}$$

By inserting $e_0(t)$ from (4.38) into (4.32), we obtain $e_1(t)$ as

$$\begin{aligned}
e_1(t) &= \frac{-\lambda_i e^{-\lambda_i(t-t_i)}}{1-M} \left[e^{-\lambda_{i+l-1}(t_{i+l}-t_{i+l-1})} \dots e^{-\lambda_{i+1}(t_{i+2}-t_{i+1})} [\rho_i + \Omega_i + \varpi_i] \right. \\
&+ \dots \\
&+ e^{-\lambda_{i+l-1}(t_{i+l}-t_{i+l-1})} [\rho_{i+l-2} + \Omega_{i+l-2} + \varpi_{i+l-2}] \\
&+ \rho_{i+l-1} + \Omega_{i+l-1} + \varpi_{i+l-1} \left. \right] - \mathcal{K}_i [1 - e^{-\lambda_i(t-t_i)}] + \frac{-\lambda_i \mathcal{M}_i}{\lambda_i^2 + \omega^2} [(\lambda_i \sin \omega t - \omega \cos \omega t) \\
&- e^{-\lambda_i(t-t_i)} (\lambda_i \sin \omega t_i - \omega \cos \omega t_i)] + \frac{-\lambda_i \mathcal{N}_i}{\lambda_i^2 + \omega^2} [(\lambda_i \cos \omega t + \omega \sin \omega t) \\
&- e^{-\lambda_i(t-t_i)} (\lambda_i \cos \omega t_i + \omega \sin \omega t_i)] + \mathcal{K}_i + \mathcal{M}_i \sin \omega t + \mathcal{N}_i \cos \omega t \tag{4.39}
\end{aligned}$$

4.4 Tracking Error at the Steady State

It is concluded from Eq. (4.39) that the tracking error at the steady state is composed of periodic exponentially decaying terms and sinusoidal terms. The decaying terms can be made to decrease

fast by making λ_i large enough. The initial values depend on the sinusoidal terms, which also can be made small by choice of parameters. Let us investigate closely the effect of different parameters on the non-decaying sinusoidal terms of (4.39)

$$e_{sin}(t) = \frac{-\lambda_i \mathcal{M}_i}{\lambda_i^2 + \omega^2} (\lambda_i \sin \omega t - \omega \cos \omega t) + \mathcal{M}_i \sin \omega t + \frac{-\lambda_i \mathcal{N}_i}{\lambda_i^2 + \omega^2} (\lambda_i \cos \omega t + \omega \sin \omega t) + \mathcal{N}_i \cos \omega t \quad (4.40)$$

To see how we can use this equation to calculate the bound on the tracking error, let us use an example with a second-order linear dynamics and substitute $\mathcal{M}_i, \mathcal{N}_i$ by their equivalent expressions $\mathcal{M}_i = \frac{\mu A_c}{(\sigma_1 + \delta_1) \beta} \frac{\Delta m_i}{m_i + \Delta m_i} (1 - \frac{1}{a_0} \omega^2)$ and $\mathcal{N}_i = \frac{\mu A_c}{(\sigma_1 + \delta_1) \beta} \frac{\Delta m_i}{m_i + \Delta m_i} (\frac{a_1}{a_0} \omega)$ in (4.40). We also approximate $(\sigma_1 + \delta_1)$ by σ_1

$$e_{sin}(t) = \frac{\mu A_c}{\sigma_1 \beta} \frac{\Delta m_i}{m_i} \left[\left(\frac{\omega^2}{\lambda_i^2 + \omega^2} \left[1 - \frac{\omega^2}{a_0} \right] - \frac{\lambda_i \omega}{\lambda_i^2 + \omega^2} \left[\frac{a_1}{a_0} \omega \right] \right) \sin \omega t + \left(\frac{\omega^2}{\lambda_i^2 + \omega^2} \left[\frac{a_1}{a_0} \omega \right] + \frac{\lambda_i \omega}{\lambda_i^2 + \omega^2} \left[1 - \frac{\omega^2}{a_0} \right] \right) \cos \omega t \right] \quad (4.41)$$

The error size depends on how the frequency ω is related to the parameter $\lambda_i = \frac{\sigma_0}{\sigma_1}$. We see from (4.41) that the sinusoidal portion of the error is proportional to the segment slope uncertainty Δm_i , the size of the reference input A_c , and the chosen size of the boundary layer. However, we can reduce this error by increasing σ_1 or β . We know that β is the amplitude of the switching component of the control signal which is constrained by the actuator limits. By increasing σ_1 , we are also required to increase σ_0 and this leads to using high gains.

For frequencies $\omega \ll \lambda_i$, the error $e_{sin}(t) \propto \frac{\omega}{\lambda_i}$ and increases as the frequency increases. However, when $\lambda_i \ll \omega \ll \omega_n$, the error will be in the form $e_{sin} \cong \frac{\mu A_c}{\sigma_1 \beta} \frac{\Delta m_i}{m_i} (\sin \omega t + \frac{\lambda}{\omega} \cos \omega t)$. The

cosine-term decreases as we increase the frequency, which causes the error to decrease. We do not have a similar term in the case of the PI controller and that is why its frequency response does not have the decreasing band. At higher frequencies as we approach the resonance frequency ω_n the terms that depend on a_1 and a_2 start to be effective and proportional to ω causing the total error to increase.

4.5 Simulation Results

The same commercial nanopositioner Nano-OP65 with Nano Drive controller, Mad City Labs Inc. is used to demonstrate the results. The simulation is based on its model and its parameters identified experimentally. The linear dynamics are fitted using experimental data with a second-order system with characteristic equation $s^2 + a_1s + a_0s$, where $a_1 = 5.743 \times 10^3$ and $a_0 = 1.717 \times 10^8$, yielding $\omega_n = 1.3 \times 10^4$ rad/s as the resonance frequency. The hysteresis is modeled with a PI-operator with 5 play operators with thresholds $r = [0, 0.63, 1.27, 2.54, 4.45]^T$ and the vector of weights for the operator is $w^T = [5.88, 1.58, 0.47, 0.98, 0.4]$. In Chapter 2, we calculated bounds on the inversion error due a perturbation with $\Delta_{w,max} = 0.15$. For the weight-threshold method, the bounds are $k_0 = 0.1282$ and $k_1 = 10.53$ while for the slope-intercept method, $k_0 = 0.09$ and $k_1 = 3.6$. Our simulation results will be presented for the smaller bounds (i.e. with the slope-intercept method) unless we compare the results of the two different methods. We insert a zero-order-hold (ZOH) in the simulation, to make the results close to the experimental ones when digital control is used.

To validate the proposed approach, non-sinusoidal reference signals are generated using the van der Pol oscillator with traveling ranges of $20 \mu\text{m}$ to $50 \mu\text{m}$. Parameters for this simulation were tuned for the best performance and found to be $\mu = 10 \times 10^3 \mu\text{m/s}$, $\sigma_1 = 5 \times 10^3$, and

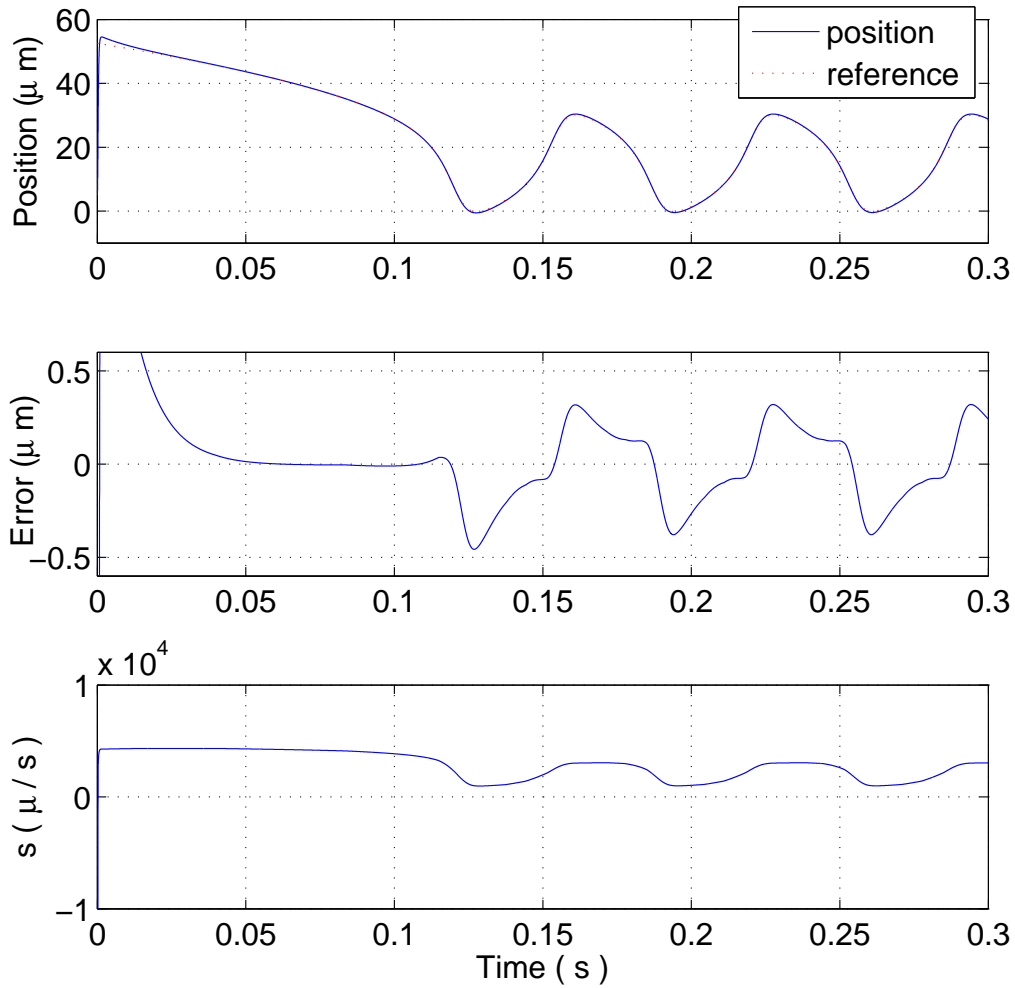


Figure 4.2: Simulation results on tracking a van der Pol oscillator-generated reference: position, tracking error and s trajectories. The bounds are calculated using slope-intercept method

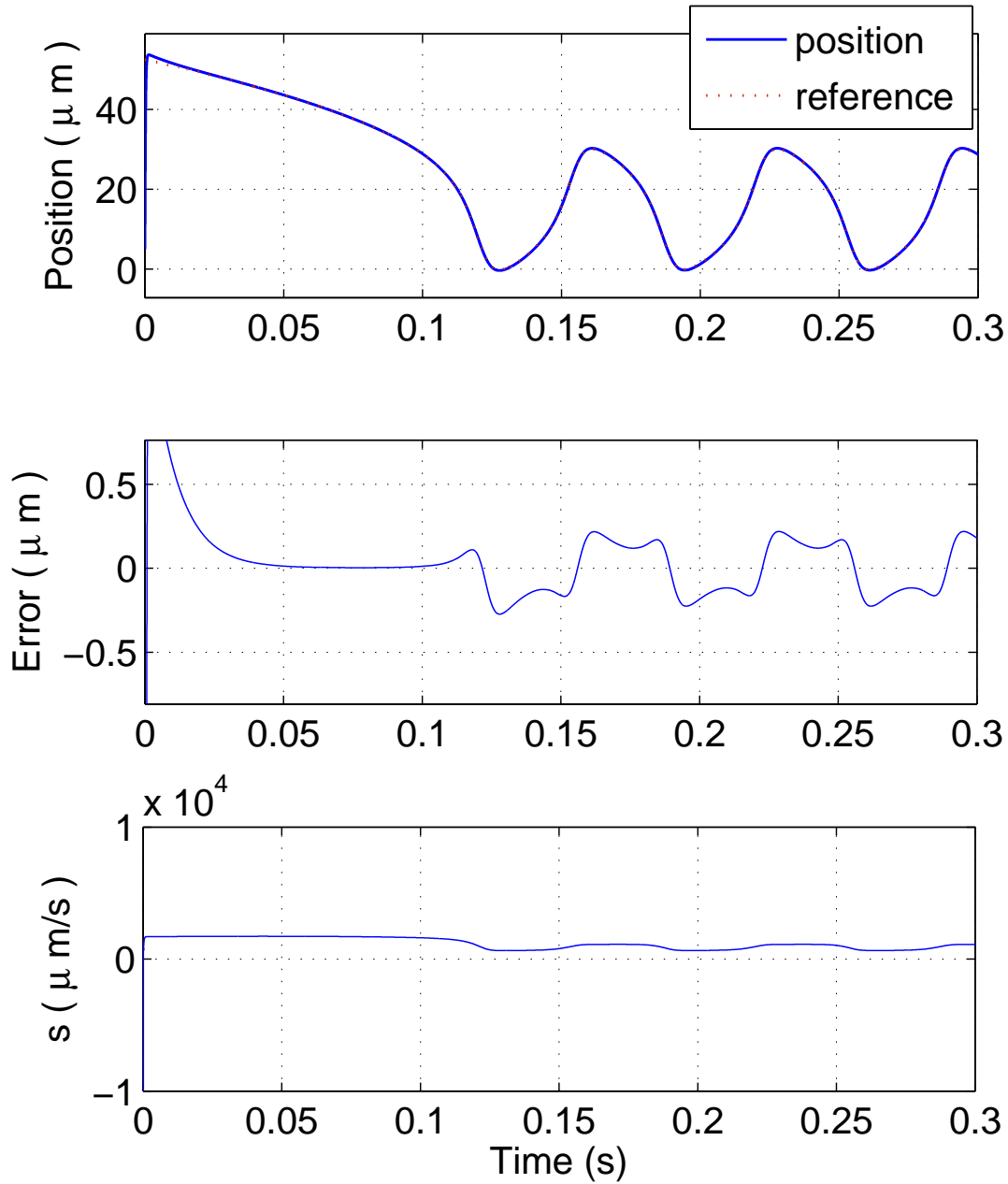


Figure 4.3: Simulation results on tracking a Van Der Pol oscillator-generated reference: position, tracking error and s trajectories. The bounds are calculated using weight-threshold method

$\sigma_0 = 25 \times 10^3$, while β is chosen as in (4.17) with $k_0 = 0.09$ and $k_1 = 3.6$. These values are high because of large bandwidth ω_n , see the scaling example of Section 4.2. The normalized values can be calculated as explained in the system scaling section. Fig. 4.2 depicts the output, tracking error and s for a reference that has a “fundamental frequency” of 15 Hz. From these results we notice that the trajectories enter the boundary layer in a very short time and the output tracks the reference after a few cycles. For comparison, we repeat the simulation with larger β calculated using the bounds from the weight-threshold method, which is illustrated in Fig. 4.3. The maximum tracking error in this case, $0.2\mu\text{m}$, compared with $0.34\mu\text{m}$ with the smaller β . This agrees with what we obtain from the analysis that the tracking error is proportional to β .

We have further run the simulation with larger parameter uncertainties, $\Delta_{w,max} = 0.25$. From Fig. 4.4, we see that the tracking error is larger than what is achieved when $\Delta_{w,max} = 0.15$. Despite the larger tracking error, the system is still stable for larger uncertainty because the bounds used to design the controller are conservative.

The following results are given when we apply sinusoidal references to the system, because it is convenient to use them to examine the system for its frequency response. Moreover, it is common to run nanopositioners with periodic signals. We, first, want to investigate how the tracking error scales with the frequency. In Fig. 4.5, we compare the maximum amplitudes of the tracking error, when the reference signal is a sinusoid with amplitude of $25\mu\text{m}$ and frequency ranging from 1 to 1000 Hz. The sliding surface coefficients are chosen as $\sigma_1 = 3 \times 10^4$ and $\sigma_0 = 3 \times 10^5$ while the boundary layer parameter is $\mu = 1 \times 10^4$. The value of μ is chosen in the order of σ_1 . From Fig. 4.5, we notice that the error increases with the frequency up to 50 Hz, then it remains almost constant for the mid-frequency range until about 400 Hz, after which it starts to decrease with the frequency until the resonance frequency. Then it increases again. The error bound of the previous section has similar characteristics for all frequencies. The tracking errors of references

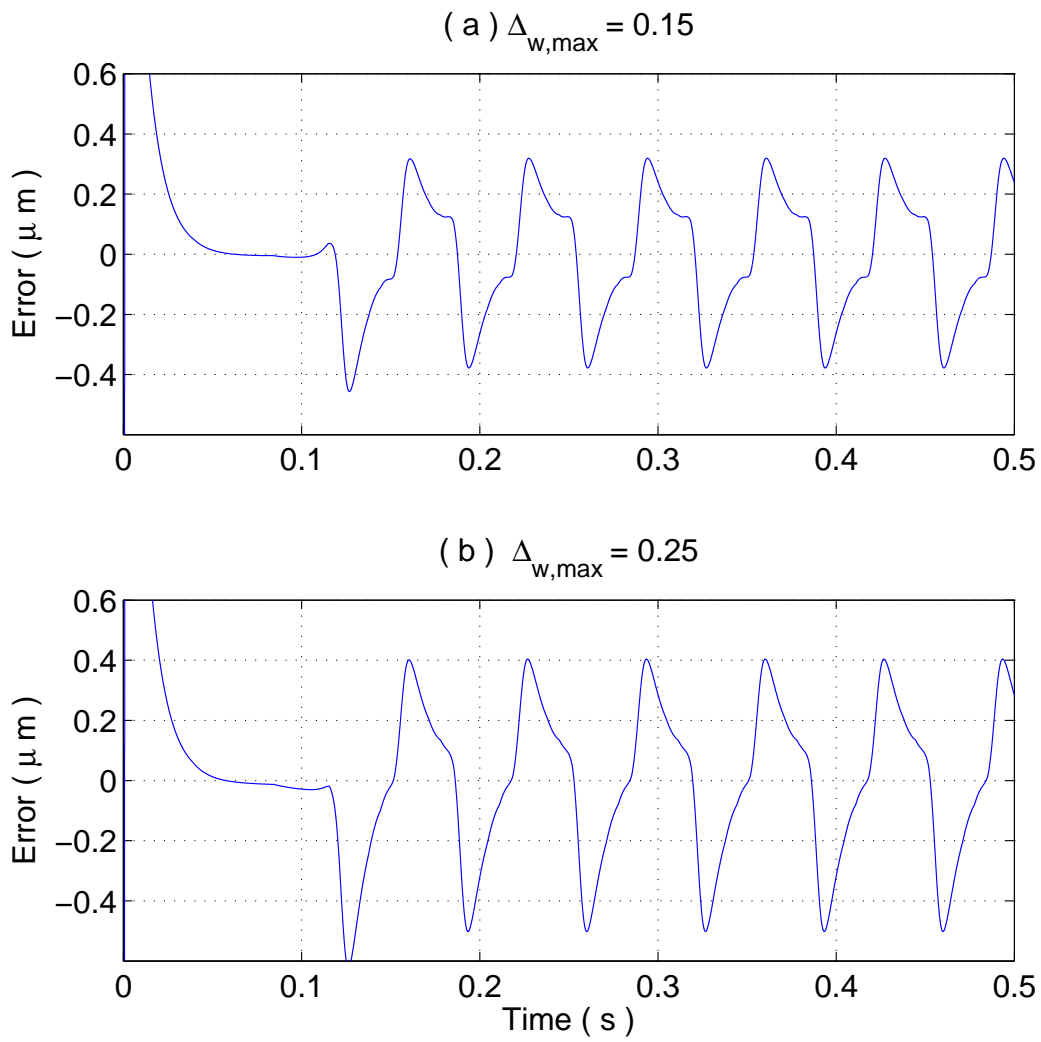


Figure 4.4: Tracking error with different $\Delta_{w,max}$

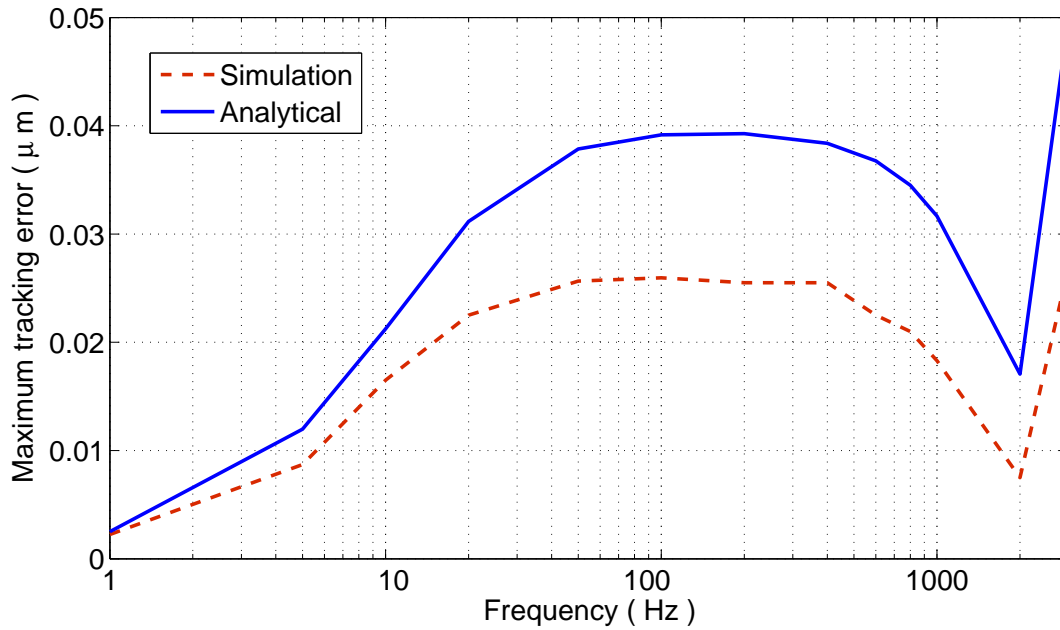


Figure 4.5: Comparison of simulation and analytical results on the tracking error at different frequencies.

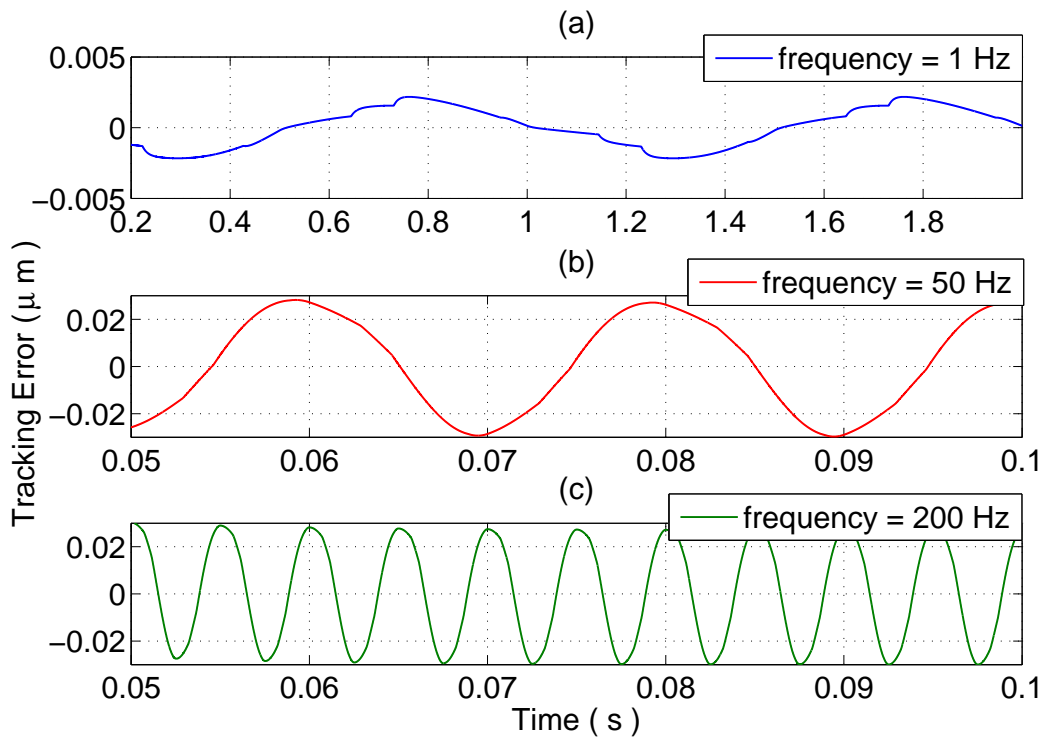


Figure 4.6: Simulation results of the tracking error of 1 Hz, 50 Hz, and 200 Hz sinusoidal references.

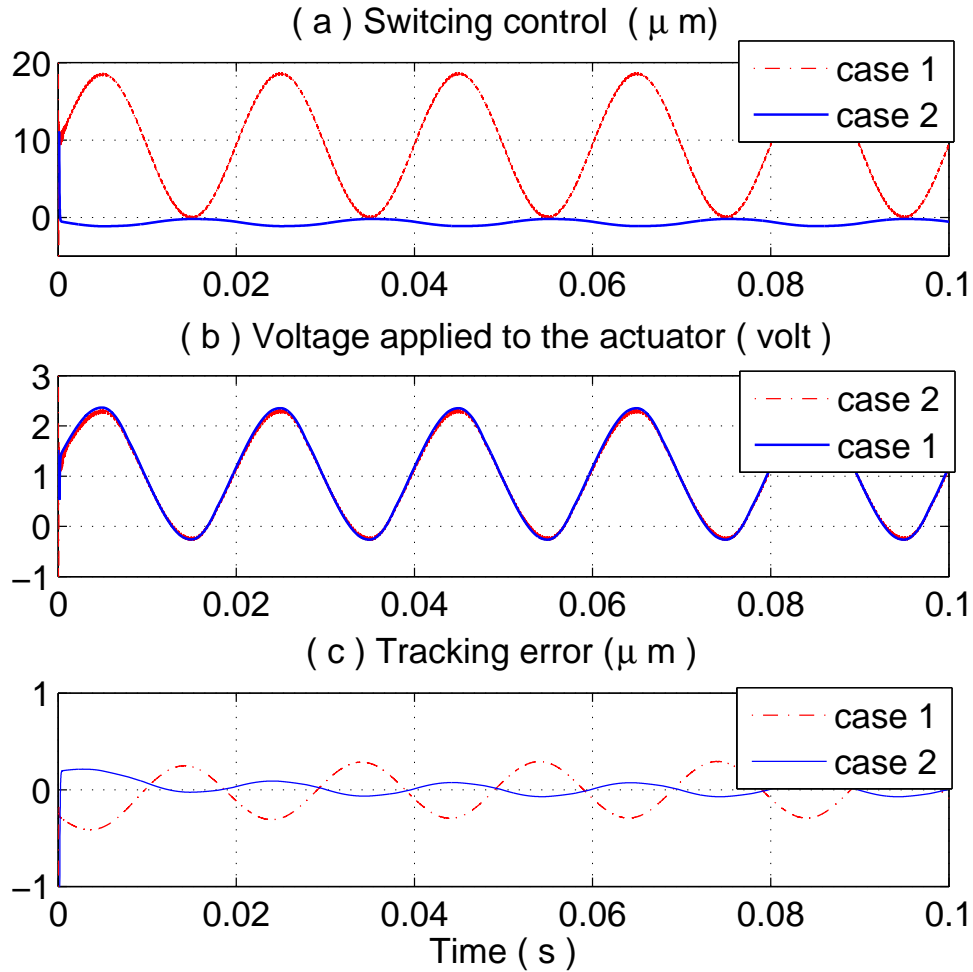


Figure 4.7: Simulation results when SMC uses only a switching control to dominate both known and uncertain terms (case 1) and when it uses a switching control to dominate the uncertain terms and equivalent control to cancel the known terms (case 2).

of amplitude $25 \mu\text{m}$ with frequencies of 1 Hz, 50 Hz, and 200 Hz are plotted in Fig. 4.6. We can see increases in the error with the frequency increasing from 1 Hz to 50 Hz, then the error becomes almost constant with very slight increase as we can see by comparing the error under the references of 50 Hz and 200 Hz.

In the SMC literature, some designers use only the switching component to dominate both known and uncertain terms [73]. In Fig. 4.7, we demonstrate that for the same choice of μ , the tracking error is much smaller when we use a control law composed form equivalent control and

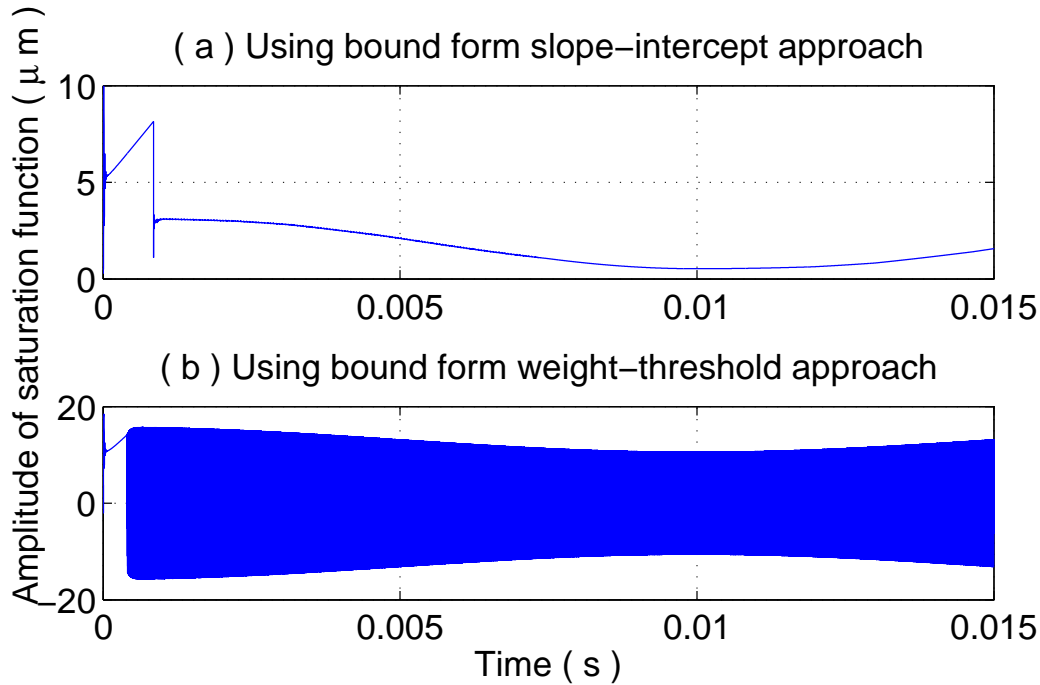


Figure 4.8: Simulation results of the tracking error for different values of β for the same value of μ .

switching control (case 2). This is because the switching function is only required to dominate the uncertain terms inside the boundary layer while the known terms are canceled using the equivalent control.

We can also show that it is better to use a smaller amplitude, β , of the saturation function. First, when μ is fixed and β is increased, chattering will occur as shown in Fig. 4.8. Then we need to increase μ in order to maintain the ratio β/μ (the slope of the saturation function) to prevent chattering. Second, using a larger β with multiple switching adversely impacts the lifetime of the actuator.

In the experiments, we add a rate limiter as a safety component to the nanopositioning system. This has an effect on the performance, especially at high frequency. We run simulations with and without rate limiter to study its effect. In Fig. 4.9, we present this comparison for 100 Hz and 200 Hz frequencies. It is obvious that the performance deteriorate when we increase the frequency at

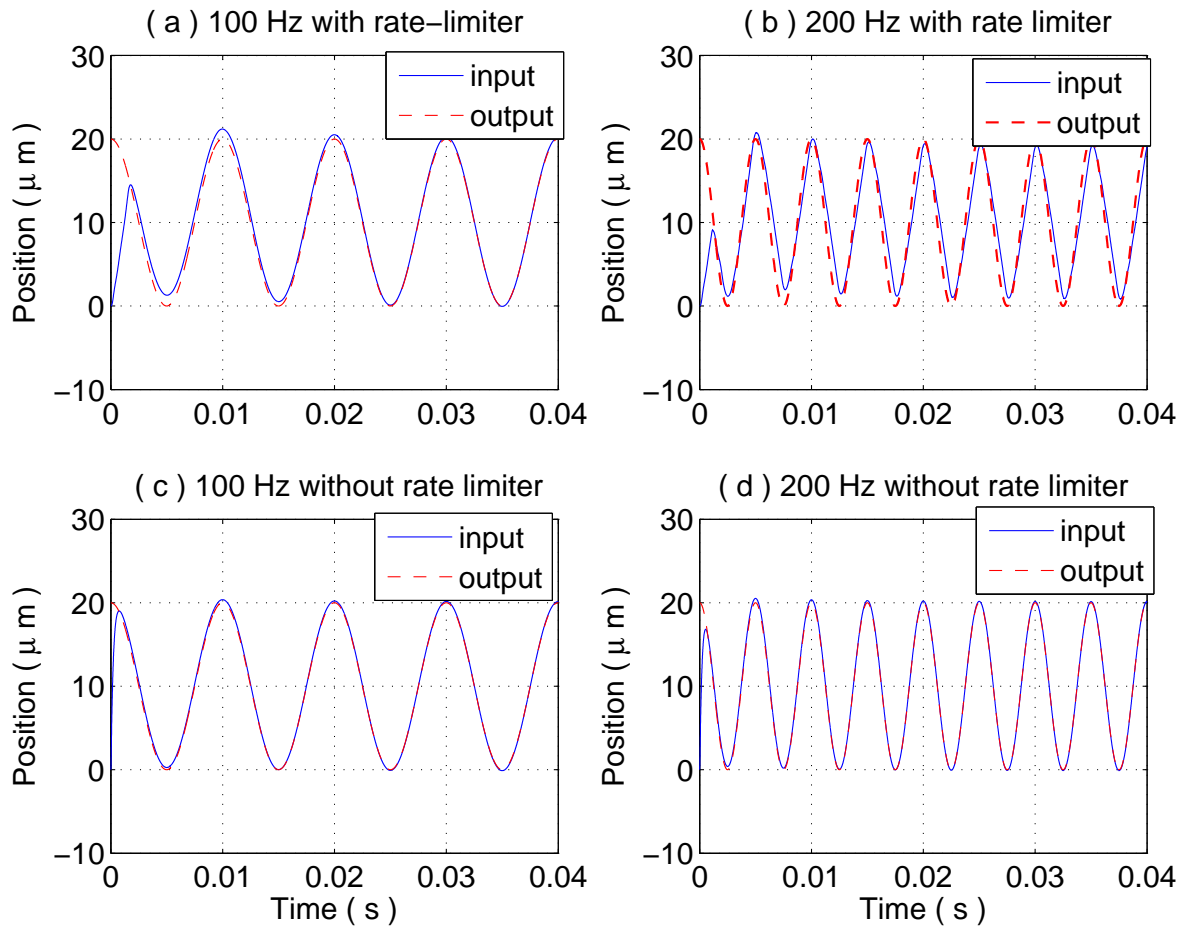


Figure 4.9: Simulation results show tracking of sinusoidal references with and without rate limiter for 100 Hz and 200 Hz.

the present of the rate limiter.

4.6 Experimental Results

Since the velocity x_2 of the nanopositioner is not measured, a linear observer is used to estimate it. In experiments, sinusoidal signals are used as reference trajectories in order to compare the proposed method with other methods that have been applied to the same nanopositioner. Fig. 4.10 shows the results for the cases of tracking a 10 Hz signal. At steady state, the maximum tracking error is 1.1%.

In Tables 4.1 and 4.2, we list more experimental results and compare them with the servo-compensator methods. Here we cite the results for Single Harmonic Servo-Compensator (SHSC) and Multi-Harmonic Servo-Compensator (MHSC) presented in [54], and these servocompensators were implemented on the same nanopositioner used in this work. It can be seen that the proposed SMC controller delivers results close to those of SHSC and behaves better at low frequencies, while the tracking performance of MHSC is in general better than SMC and SHSC. The mean error of the SMC method at 5 Hz, however, is much smaller than those of SHSC and MHSC. This indicates that the imposed rate limiter in the SMC output during the experiments could have led to larger errors at higher frequencies. We note that while the servocompensators are designed for periodic references of given frequencies, frequency of the periodic reference is not used in SMC designs.

Sinusoidal signals are also used to examine the response of the system when different bounds of the inversion error are used in the SMC design. First, we compare when the controller with and without the equivalent control u_{eq} . The results as shown in Fig. 4.11 confirms with simulation results that the performance is improved when the equivalent control is included.

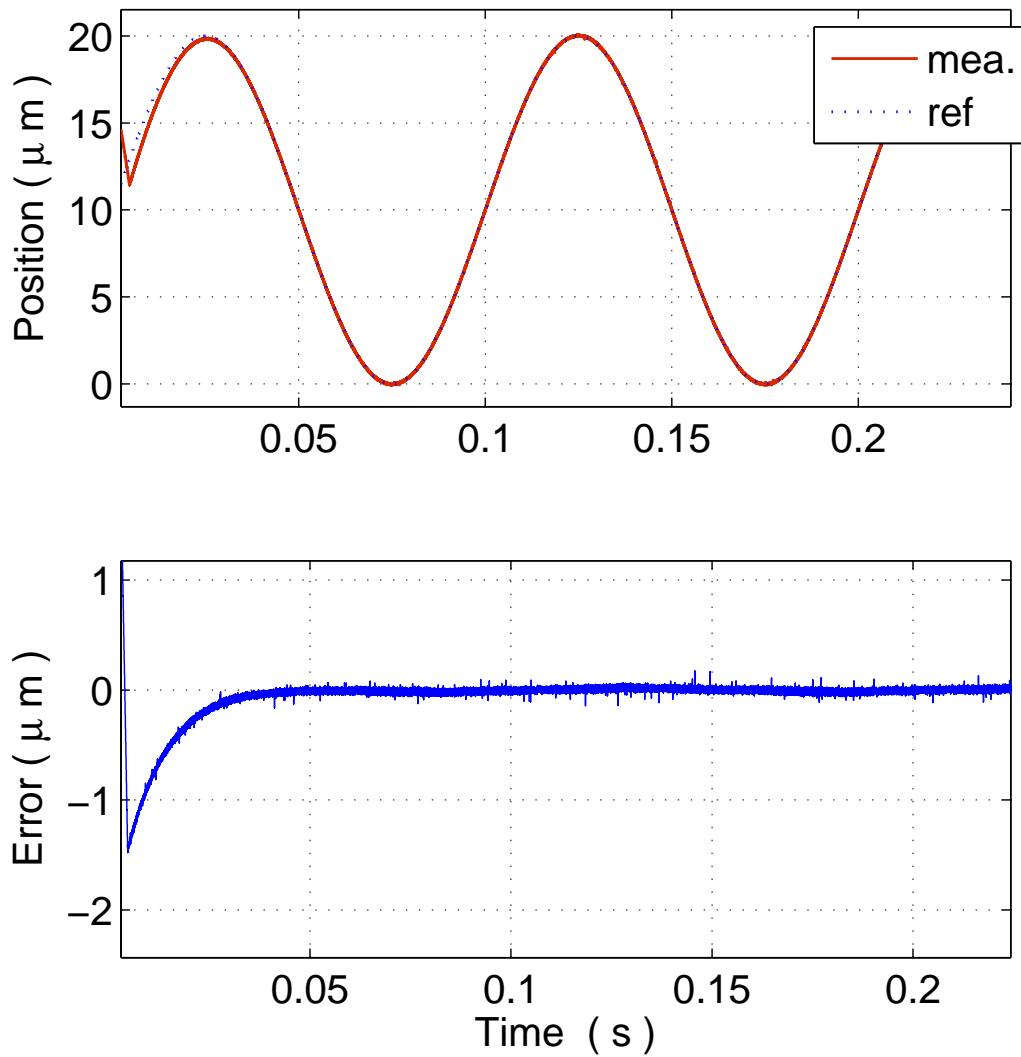


Figure 4.10: Experimental results on tracking a 10 Hz sinusoidal reference. The curve “mea.” was obtained from measurement, while “ref” represents the reference signal.

Table 4.1: Comparison between maximum tracking errors for SMC-, MHSC- and SHSC- methods

frequencies	SMC-controller	MHSC-controller	SHSC
	Max $ e(t) $ %	Max $ e(t) $ %	Max $ e(t) $ %
5 Hz	0.95	0.899	1.72
25 Hz	1.7	0.881	1.85
50 Hz	2.25	1.01	1.93
100 Hz	2.75	1.57	2.38

Table 4.2: Comparison between mean tracking errors for SMC-, MHSC- and SHSC- methods

frequencies	SMC-controller	MHSC-controller	SHSC
	Mean $ e(t) $ %	Mean $ e(t) $ %	Mean $ e(t) $ %
5 Hz	0.119	0.271	0.649
25 Hz	0.62	0.268	0.707
50 Hz	0.66	0.284	0.770
100 Hz	0.83	0.352	0.815

In all experiments, a rate limiter is implemented, to protect the positioner from sudden changes of the applied voltage. The rate limiter modifies the control input to meet the rate constraint, which distorts the control signal when tracking relatively high-frequency references. At high frequency, it introduces a phase lag between the reference signal and the output causing a larger tracking error as shown in Fig. 4.12. We add a rate limiter to the simulation for the purpose of comparison and we see that the frequency response in this case is similar to the experimental response as illustrated in Fig. 4.13. It makes the tracking error increases with frequency and we do not see the flat region as in Fig. 4.5 when the rate limiter is not used.

The bounds on the inversion error determine the amplitude of the saturation function β , which is used to dominate the uncertainties on the system. From our analysis, we observe that by increasing β , the error size will be smaller. On the other hand, the controller amplitude will be larger and this is limited by the constraint of the control signal, particularly when we want to achieve a larger positioning range. In Fig. 4.14 we use a bound with $\beta = 5.5$. In Fig. 4.15 we use $\beta = 25$. We

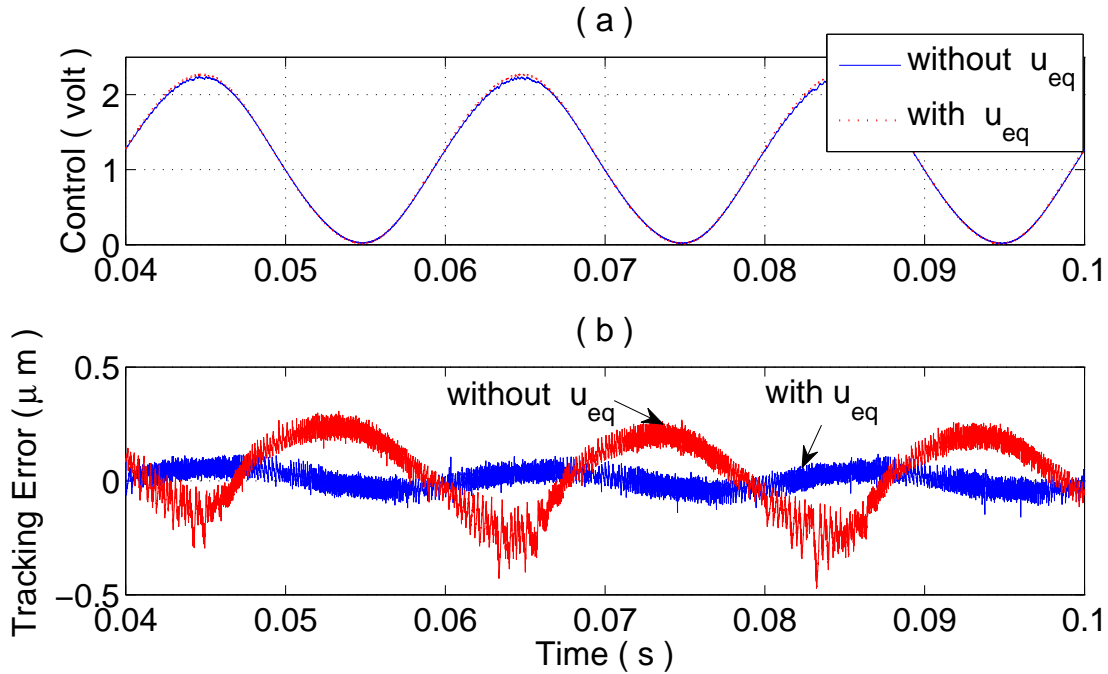


Figure 4.11: Experimental results at steady state (a) applied control signal on actuator (b) Tracking Error.

can see that we have a smaller tracking error $0.18\mu\text{m}$ for the larger β of Fig. 4.15 compared with $0.2\mu\text{m}$ of Fig. 4.14.

4.7 Summary

Hysteresis nonlinearity is a challenge in many applications that require tracking control. The general approach to dealing with it is to use hysteresis-inverse compensation integrated with feedback control. In this chapter, we presented a sliding mode control method to handle systems with hysteresis nonlinearities. We have used the bounds, which are derived in Chapter 2 to design the SMC

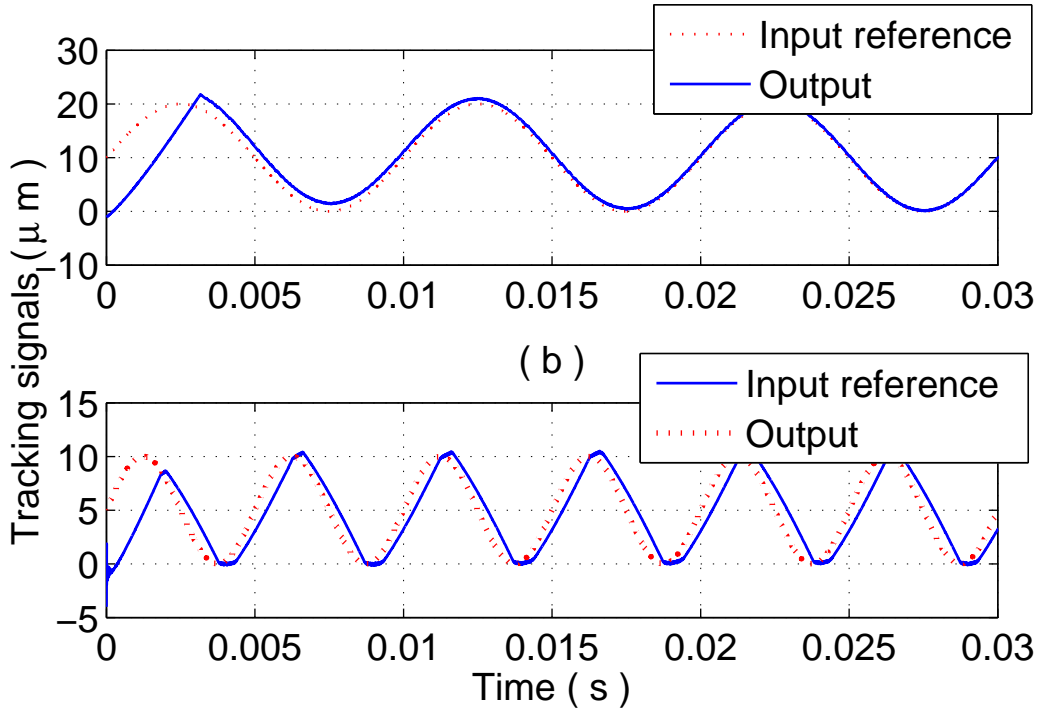


Figure 4.12: Experimental results show tracking of sinusoidal references at (a) 100 Hz and (b) 200 Hz.

controller. Furthermore, we derived an expression for the tracking error inside the boundary layer of the sliding surface. It is shown that the error is proportional to the chosen boundary layer size (μ) and inversely proportional to the coefficient of the error term (σ_1) in the surface equation as well as the amplitude of the saturation function (β) of the control signal. Decreasing (β) allows more traveling range for the actuator but at the cost of the performance. The expression of the tracking error shows how the error scales with frequency. It is shown analytically and by simulation that the error increases in the first portion ($\omega < \lambda$) of range of interest and stays constant before it is affected by resonance frequency of the linear dynamics. Simulation results also show that we can obtain good tracking performance with general (non-sinusoidal) waveforms. Experiments were conducted for a piezo-electric actuator, where the results confirm the effect of changing different parameters on the qualitative behavior of the signals. In these experiments, we included

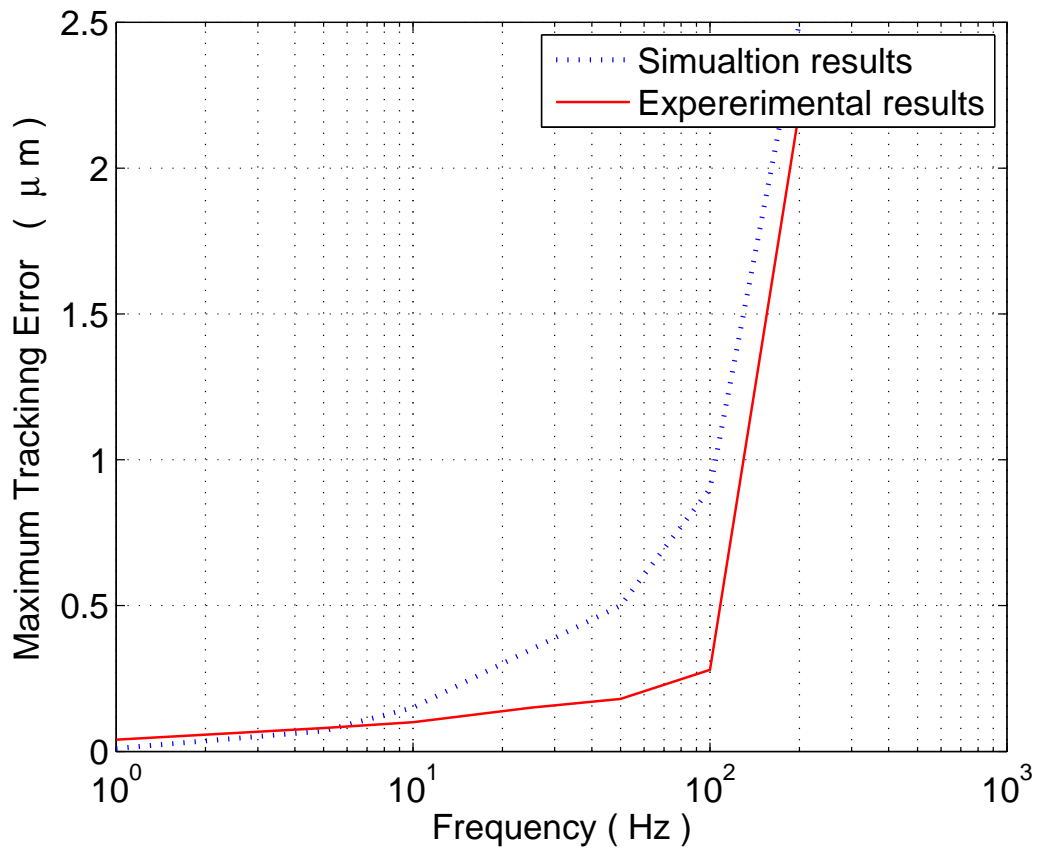


Figure 4.13: A comparison between experimental and simulation results when the rate limiter is included in the simulated system.

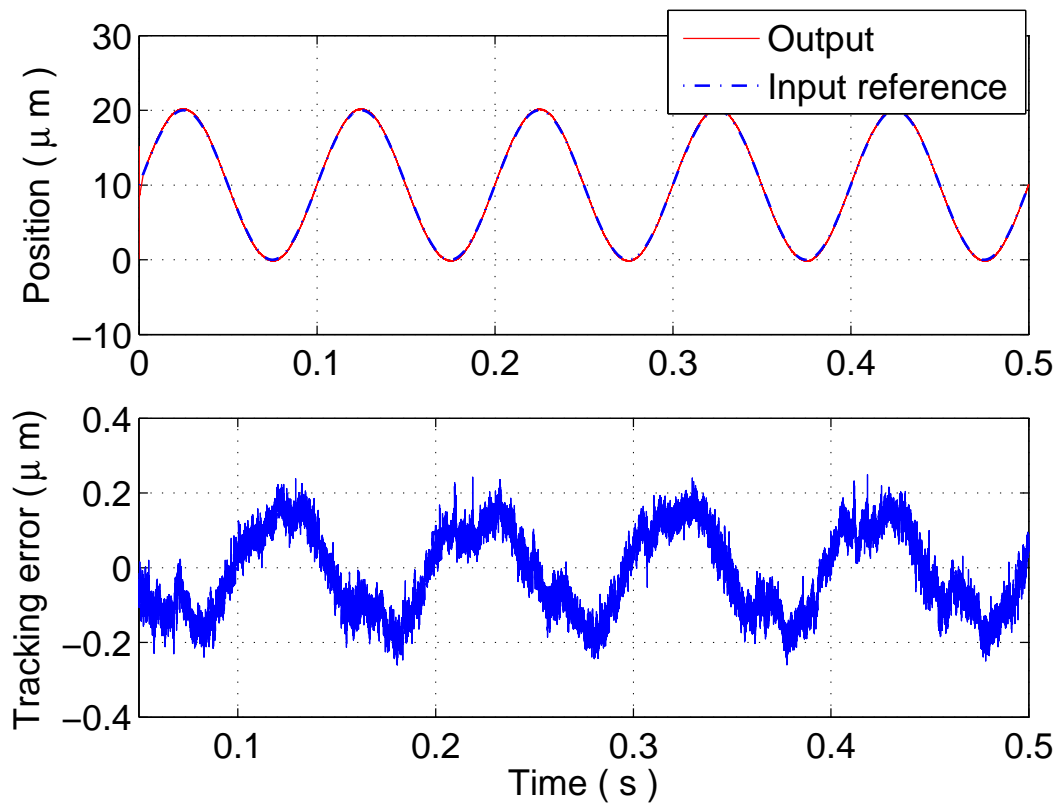


Figure 4.14: Experimental results of the tracking error with saturation function of $5\mu\text{m}$ amplitude.

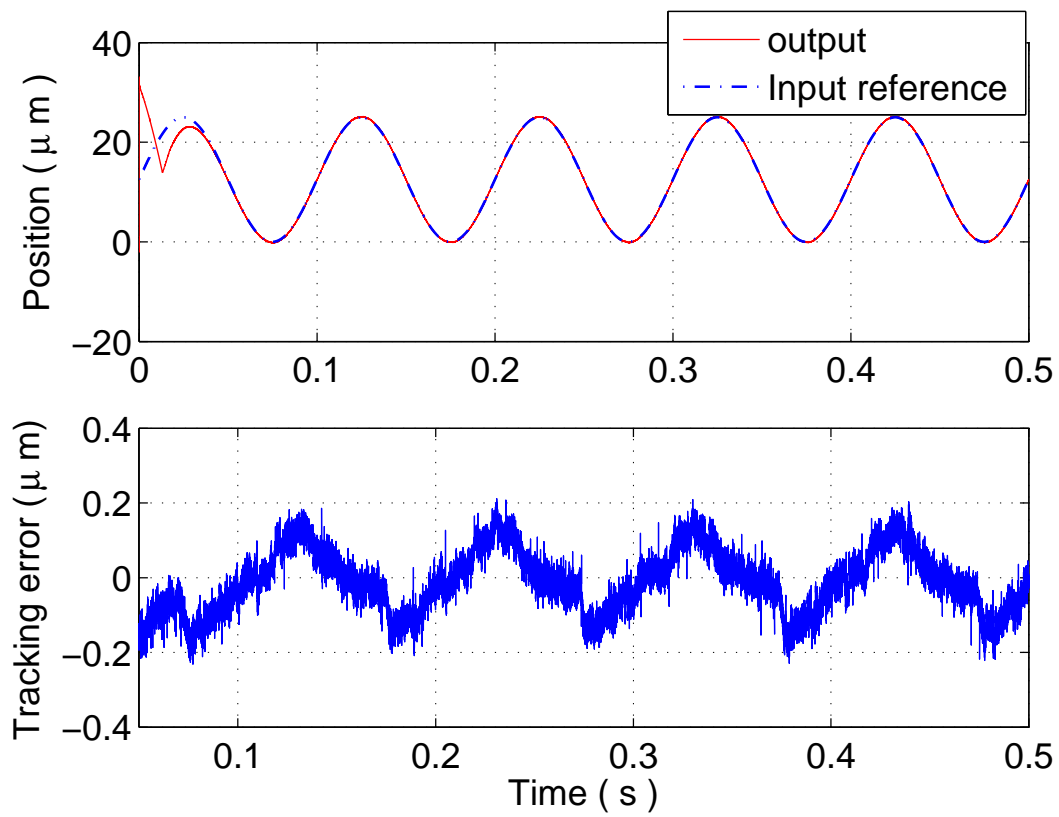


Figure 4.15: Experimental results of the tracking error with saturation function of $25\mu\text{m}$ amplitude.

a rate-limiter to protect the device, which resulted in less smooth trajectories compared with the simulation. Simulation and experimental results show that the performance deteriorates especially at high frequency due to the rate limiter. A comparison with the SHSC method shows that the proposed controller has comparable performance to the servo-compensator whereas MHSC has better results than SMC. Yet, SMC is able to track arbitrarily-shaped references and periodic references with unknown frequencies.

Chapter 5

H_∞ Control Design

5.1 Introduction

In this chapter, we propose a linear robust controller the systems comprising a hysteresis operator preceding a linear stable system. The hysteresis operator is modeled with piecewise linear characteristics with uncertainties, and a nominal inverse operator is included to mitigate the hysteresis effect. An H_∞ control design is proposed to handle the remaining uncertainties in a two-degree-of-freedom (2DOF) framework. In the existing work [62, 63, 64, 65], the H_∞ control is designed for a nominal plant while hysteresis is treated as uncertainty. The hysteresis nonlinearity is not modeled or inverted in those methods. In our work we reduce the effect of hysteresis by inversion and only the remaining inversion error determines the size of the uncertainty. We compared the proposed H_∞ method with a PI controller when 2DOF is applied to both system. The PI controller usually has good performance at low frequencies, however, it does not take advantage of knowing the dynamics of the system as in H_∞ design, where we can improve the performance at high frequency. Simulation results on a model of piezoelectric actuator-based nanopositioner are presented to illustrate the design and analysis, where the hysteresis nonlinearity is represented by a Prandtl-Ishlinskii operator.

5.2 Problem Formulation

Robust control methods are developed for uncertain linear systems. The design, in general, aims to achieve the desired performance while maintaining stability. We recall from the previous chapter that the inversion error is composed of two components: $\frac{\Delta m}{m}u$ and Δ_{dc} . We can represent the second component as an external disturbance $d = \Delta_{dc}$, while the first component $\frac{\Delta m}{m} = \Delta$ depends on the control u and can lead to instability in the closed loop system if not treated carefully. With this treatment for the uncertainty, the system can be represented as in Fig. 5.1.

The H_∞ control problem is defined for a system representable by the general block diagram of Fig. 5.2, where P is the interconnection matrix, K is the controller, Δ is the set of all possible uncertainties, w is a vector signal including noise, disturbances, and reference signals, z is a vector signal including all controlled signal, and y is the measurement.

The block diagram in Fig. 5.2 represents the following equations:

$$o = \Delta v \tag{5.1}$$

$$y = Ku \tag{5.2}$$

and

$$\begin{bmatrix} v \\ z \\ y \end{bmatrix} = \begin{bmatrix} p_{11} & p_{12} & p_{13} \\ p_{21} & p_{22} & p_{23} \\ p_{31} & p_{32} & p_{33} \end{bmatrix} \begin{bmatrix} o \\ w \\ u \end{bmatrix} \tag{5.3}$$

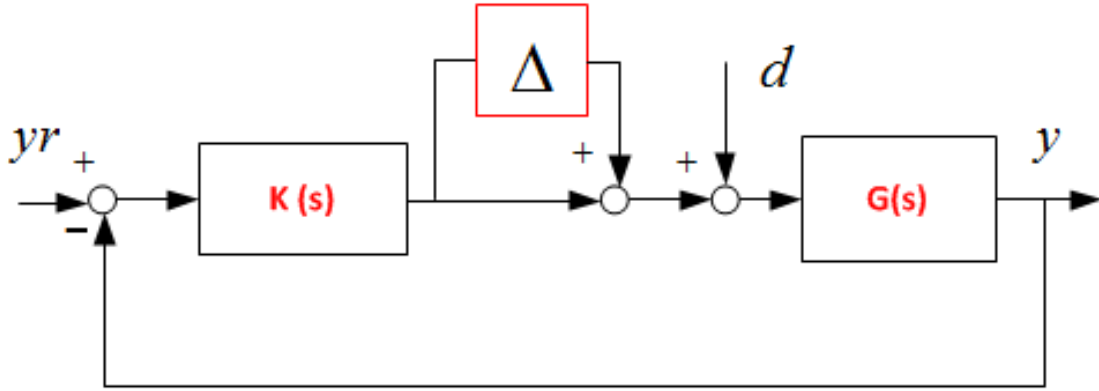


Figure 5.1: The closed-loop system with the inversion error represented as multiplicative uncertainty.

Let the transfer function from w to z be denoted by T_{zw} . The objective is to design a controller K such that the closed-loop system is stable for all admissible Δ and $\|T_{zw}\|_{\infty} \leq \gamma_p$ for prespecified $\gamma_p > 0$, where $\|T_{zw}\|_{\infty}$ is the H_{∞} norm defined by $\|T_{zw}\|_{\infty} = \sup_{\omega} \bar{\sigma}(T_{zw}(j\omega))$, where $\bar{\sigma}(\cdot)$ is the maximum singular value of the matrix.

The design objective in our problem is to obtain the smallest tracking error e which is chosen as one of the output component of the vector z in the presence of the exogenous signals $w = [d \ y_r \ n]^T$, where y_r is the reference signal, n is the measurement noise and d is the disturbance. It is useful to specify the performance objectives as the requirements on a sensitivity function $S = (I + L)^{-1}$ and the complementary sensitivity function $T = L(I + L)^{-1}$, where L is a loop function defined as $L = KG$ for a plant G and a controller K . By definition,

$$S + T = I \quad (5.4)$$

For a SISO system $S + T = 1$. Ideally, we want S small to obtain the benefits of feedback (small tracking error for commands and disturbances), and T small to avoid sensitivity to noise which

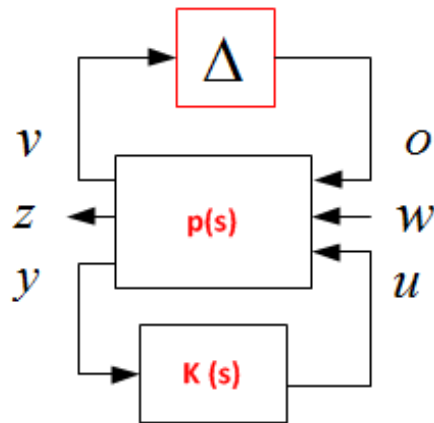


Figure 5.2: A general robust control framework for systems uncertainties.

is one of the disadvantages of feedback. From (5.4), it is clear that these requirements are not simultaneously possible at any frequency, and $|S(j\omega)|$ and $|T(j\omega)|$ at any frequency can differ by one.

One important component when designing optimal control problem is to choose weighting matrices or weighting functions in the scalar case. We shall modify the feedback diagram in Fig. 5.1 into Fig. 5.3. The weighting functions are chosen to reflect the design objectives and the knowledge of the disturbances and sensor noise. However, in many occasions, the weights are chosen purely as design parameters without any physical bases, so these weights may be treated as tuning parameters that are chosen by the designer to achieve the best compromise between conflicting objectives. For example, W_d may be chosen to reflect the frequency contents of the disturbance d , the weight matrix W_n is used to model the frequency contents of the sensor noise, while W_e may be used to reflect the requirements on the shape of certain closed-loop transfer functions. Similarly, W_u may be used to reflect some restrictions on the control or actuator signal. It is interesting to know that the H_∞ design framework does not in general produce integral control, but integral action can be introduced by the choice of the weighting functions. The resulting

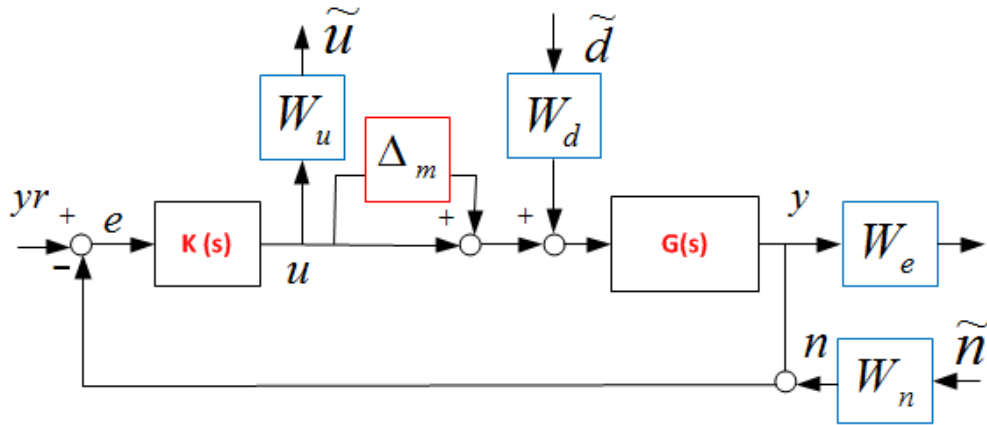


Figure 5.3: Adding weight functions in the closed-loop system for optimal design.

controller must have a pole at $s = 0$. This will violate the assumptions of H_∞ theory because we will have uncontrollable pole of the feedback system [72]. Instead, we shift that pole to the left by introducing $s + \varepsilon$, where ε is a sufficiently small positive number.

5.3 Control System Design and Analysis

When feedback-only configuration is used, the performance specification can be quantified by analyzing the tracking error. For a given controller $K(s)$, the tracking error is given by

$$e = y_r - y = S(y_r - d) + Tn \quad (5.5)$$

From (5.5), we can see that to achieve small tracking error we require S and T to be small but at different frequency ranges depending on the frequency content of the signals y_r , d , n . This feedback configuration has several limitations and instead we use a Two-degree-of-freedom (2DOF)

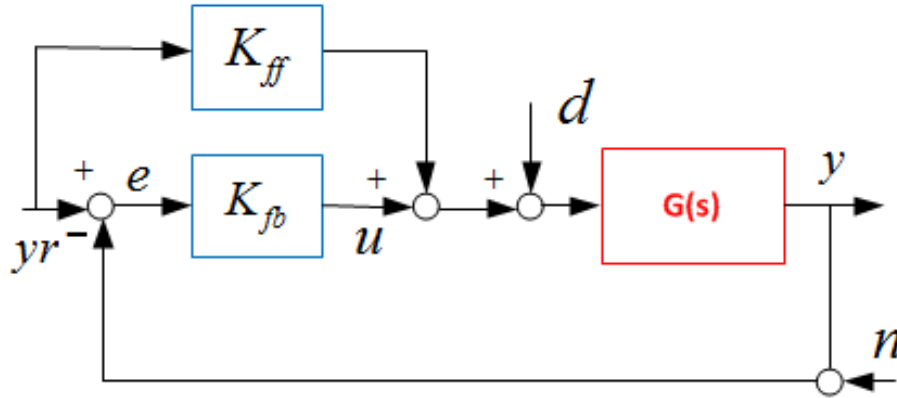


Figure 5.4: Two degree of freedom feedback design.

structure. There are different 2DOF designs in the literature, but we consider the configuration which is shown in Fig 5.4 to compare the results with the PI -controller when 2DOF design is considered. In this case we denote the feedforward controller by K_{ff} and the feedback controller by K_{fb} . The control law is

$$u_d = K_{ff}y_r + K_{fb}(y_r - y) \quad (5.6)$$

Robustness in this case is still determined by the sensitivity function $S = (1 + GK_{fb})^{-1}$ and the transfer function from n to y is determined by the complementary sensitivity function $T = (1 + GK_{fb})^{-1}GK_{fb}$. In 2DOF design, the transfer functions from y_r to y and from n to y are designed independently.

Let us denote the transfer function from y_r to e by $S_{er} = S(1 - GK_{ff})$. In this case, by choice of $K_{ff}(s) \simeq G(s)^{-1}$ provided that K_{ff} is proper, we can make S_{er} close to zero.

It should be noted that these optimization problems have been studied extensively and there exist standard software routines (for instance in MatLab) where H_∞ problems can be solved. we use

MatLab to solve the feedback problem in optimal control setting. In order to reflect the performance objectives and physical constraints, the weighting functions are chosen as

$$W_e = \frac{20(s + 800)}{s + 2.05 \times 10^4} \quad (5.7)$$

$$W_n = \frac{0.1s + 25 \times 10^4}{s + 1200} \quad (5.8)$$

The final expressions of W_e and W_n are determined in an ad-hock way in simulations. We choose them as first order transfer functions in order to make the controller simple. Our first choice is also related to the nominal plant bandwidth $\omega_n = 1.3 \times 10^4$ rad/s, where we chose W_e to reject disturbances at low frequencies less than $\omega = 2\pi \times 250$ rad/s, and W_n to reject high frequency noise above 250 Hz. The exogenous variable $w = [e \ \tilde{u}]^T$ and the regulated variables $z = [\tilde{d} \ \tilde{n}]^T$.

The transfer function from w to z is

$$\begin{bmatrix} e \\ \tilde{u} \\ y \end{bmatrix} = \begin{bmatrix} W_e W_d G & 0 & W_e G W_u \\ 0 & 0 & W_u \\ W_d G & W_n & G \end{bmatrix} \begin{bmatrix} \tilde{d} \\ \tilde{n} \\ u \end{bmatrix} \quad (5.9)$$

The controller obtained by Matlab is

$$K_{fb}(s) = \frac{2700s + 1.62 \times 10^6}{s^2 + 376s + 4.1 \times 10^4} \quad (5.10)$$

To check the stability of the closed-loop system, we need to check for the transfer function G_{p11} , which is given below that $\|G_{p11}\|_\infty \leq \gamma$ when the uncertainty $\|\Delta\|_\infty < 1/\gamma$.

$$\begin{bmatrix} v \\ z \end{bmatrix} = \begin{bmatrix} G_{p11} & G_{p12} \\ G_{p21} & G_{p22} \end{bmatrix} \begin{bmatrix} o \\ w \end{bmatrix} \quad (5.11)$$

It is found that $\|G_{p11}\|_\infty = 0.99$, which confirms that our design is stable for the uncertainties $\|\Delta\|_\infty \leq 0.114$. For the H_∞ control, we use K_{fb} of Eq. (5.10) and we use $K_{fb} = k_p + k_I s$ for the PI controller, while we use $K_{ff} = 1$ for both controllers. Since the gain of $G(s)$ approximately equals one for wide range of frequencies, we have $|G^{-1}(s)| \simeq 1$, which implies that $S_{er} = S(1 - GK_{ff})$ is made small by having $K_{ff} = 1$.

5.4 Simulation Comparison between including and not including the inverse operator with H_∞ control

The commercial nanopositioner is used to demonstrate the results. The simulation is based on an experimentally-identified model. The linear dynamics are fitted experimentally with a second-order system with characteristic equation $s^2 + a_1 s + a_0$, where $a_1 = 5.743 \times 10^3$ and $a_0 = 1.717 \times 10^8$, implying the resonant frequency of $\omega_n = 1.3 \times 10^4$ rad/s. The hysteresis is modeled with a PI-operator with 5 play operators with thresholds $r = [0, 0.63, 1.27, 2.54, 4.45]^T$ and the vector of weights for the operator is $w^T = [5.88, 1.58, 0.47, 0.98, 0.4]$. We start the simulation by examining the performance for the case when the inverse operator is not included in the feedback loop with the case when it is present. We compare the tracking errors in Fig. 5.5 for sinusoidal references of frequencies 25 and 100 Hz. Regardless of the frequency, the tracking error is smaller

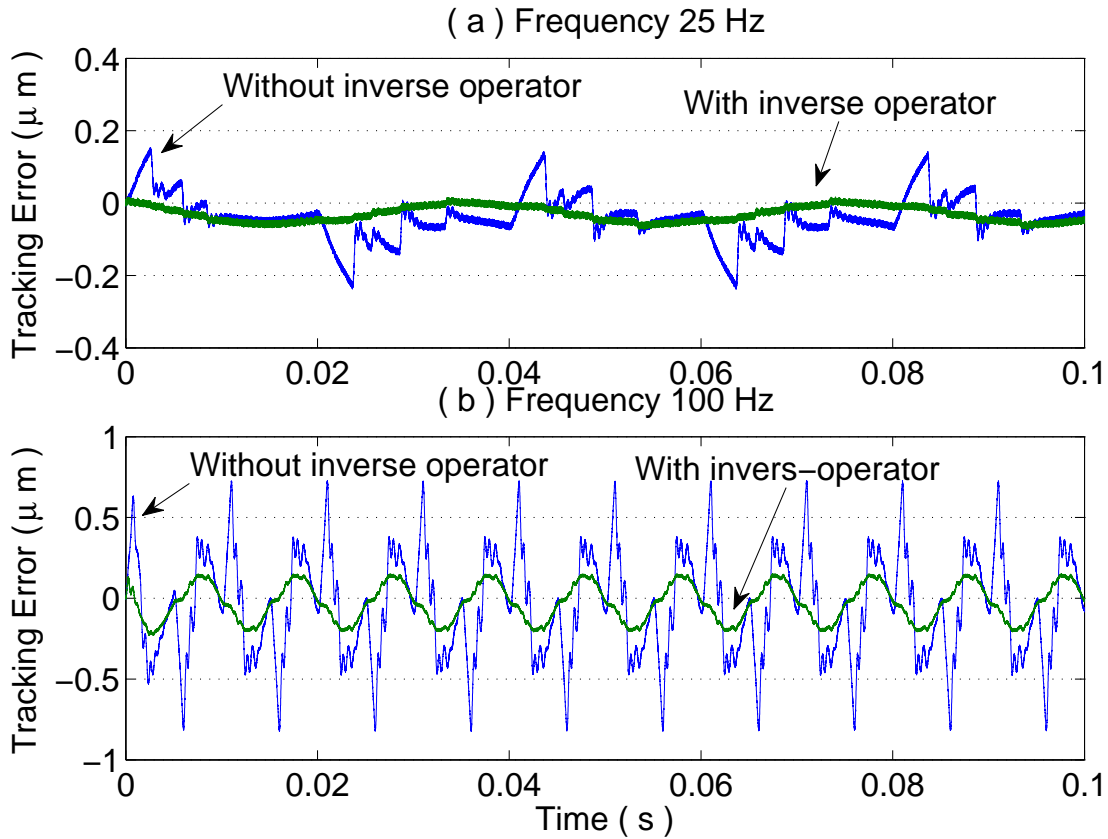


Figure 5.5: Simulations results of H_{∞} control with and without inverse-operator at frequencies (a) 25 Hz and (b) 100 Hz.

when the inverse-operator is used. This is expected because the size of the plant perturbation is larger when hysteresis inversion is not included. Another observation from Fig. 5.5 is that the tracking error in the case with inverse-operator has a smoother waveform, while in the other case we can see sharp changes corresponding to transversing from one segment to another. These changes can affect the overall performance of the system and can create more harmonics in the closed loop system.

5.5 Simulation Comparison between H_∞ and PI control

For the purpose of simulation, we perturbed each component on the weight vector by $\Delta_{w,max} = 0.15$. This perturbation is done in such a way that the size of the inversion error is close to what we have from experiment when the inverse operator is cascaded with the real nanopositioner. We calculated the corresponding maximum uncertainties as $|\Delta_{m,max}| = 0.08$ and $|\Delta_{\gamma,max}| = 3.7$.

Sinusoidal reference signals with amplitude of $50 \mu\text{m}$ and different frequencies are applied to PI and H_∞ control systems. Parameters for the PI controller are chosen as $k_i = 3154$ and $k_p = 1$ by tuning them for the best performance. In Fig. 5.6 we compare the two control methods at 1 Hz, 50 Hz, and 350 Hz. We can see that the tracking error for PI controller is smaller at 1 Hz. The error for PI controller is centered at zero because integral control can eliminate the DC error. At 50 Hz we can see that we achieve better performance using H_∞ control because it is designed to have good response up to 250 Hz according to the choice of the weighting function. Then, the PI controller starts to have a less tracking error as illustrated in Fig. 5.6 c at frequency of 350 Hz. In Table 5.1, we present more results for the maximum tracking error versus frequency for both methods.

Simulation results are also depicted in Fig 5.7, to examine adding a rate limiter to the system. It is noted that the rate limiter has little effect at low frequencies, but it increases the tracking error when we are close to 90 Hz.

5.6 Simulation Comparison between H_∞ , PI, and SMC control

We conclude this chapter by a comparison for the three proposed control methods of this chapter and Chapters 3 and 4. The maximum value of the absolute error of the tracking error ($\text{Max } |e(t)|$) is compared at different frequencies. A reference sinusoidal signal of amplitude $50 \mu\text{m}$ is applied to

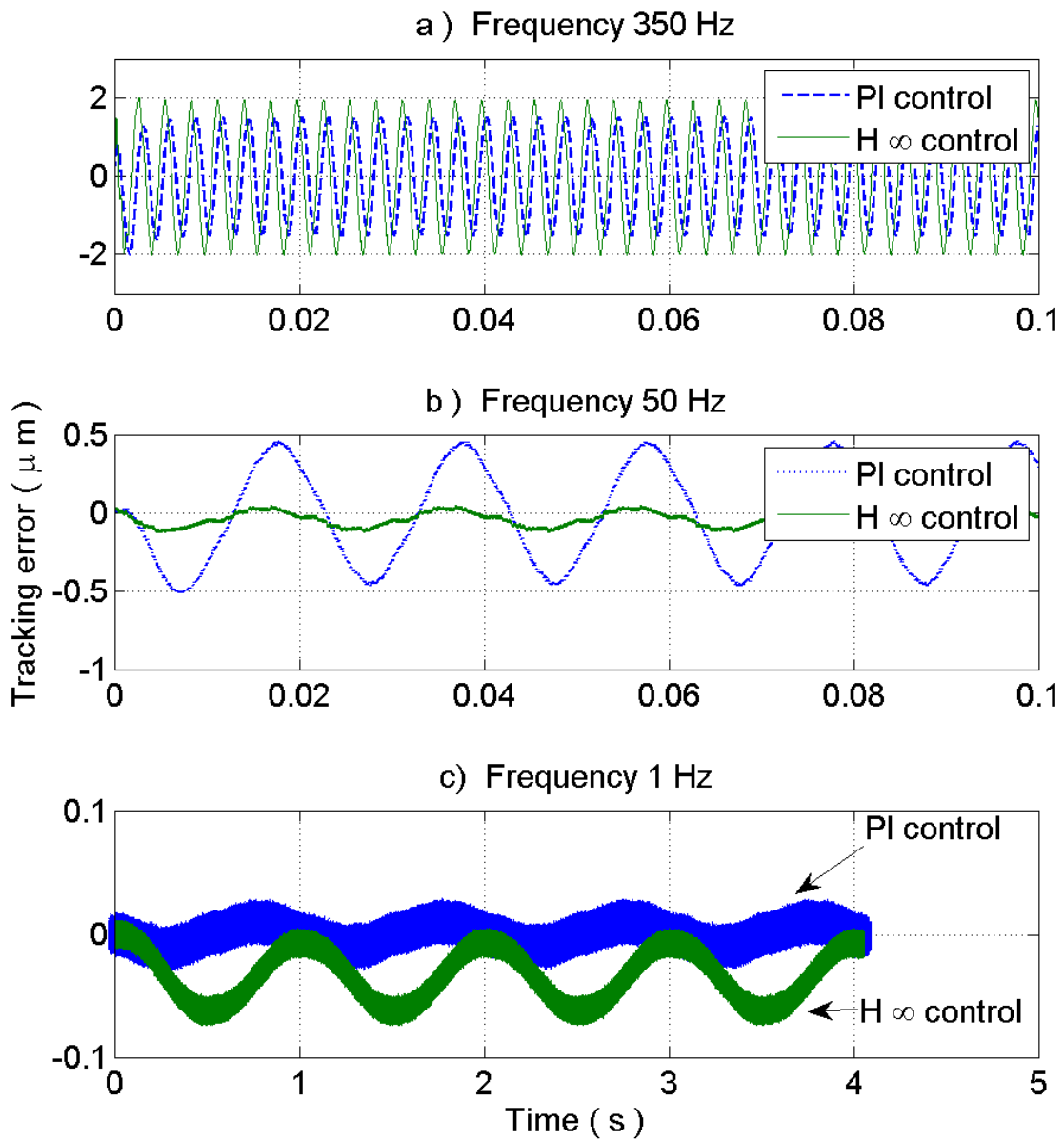


Figure 5.6: Simulations results for tracking error with PI and H^∞ control for frequencies a) 350 Hz, b) 50 Hz, c) 1 Hz.

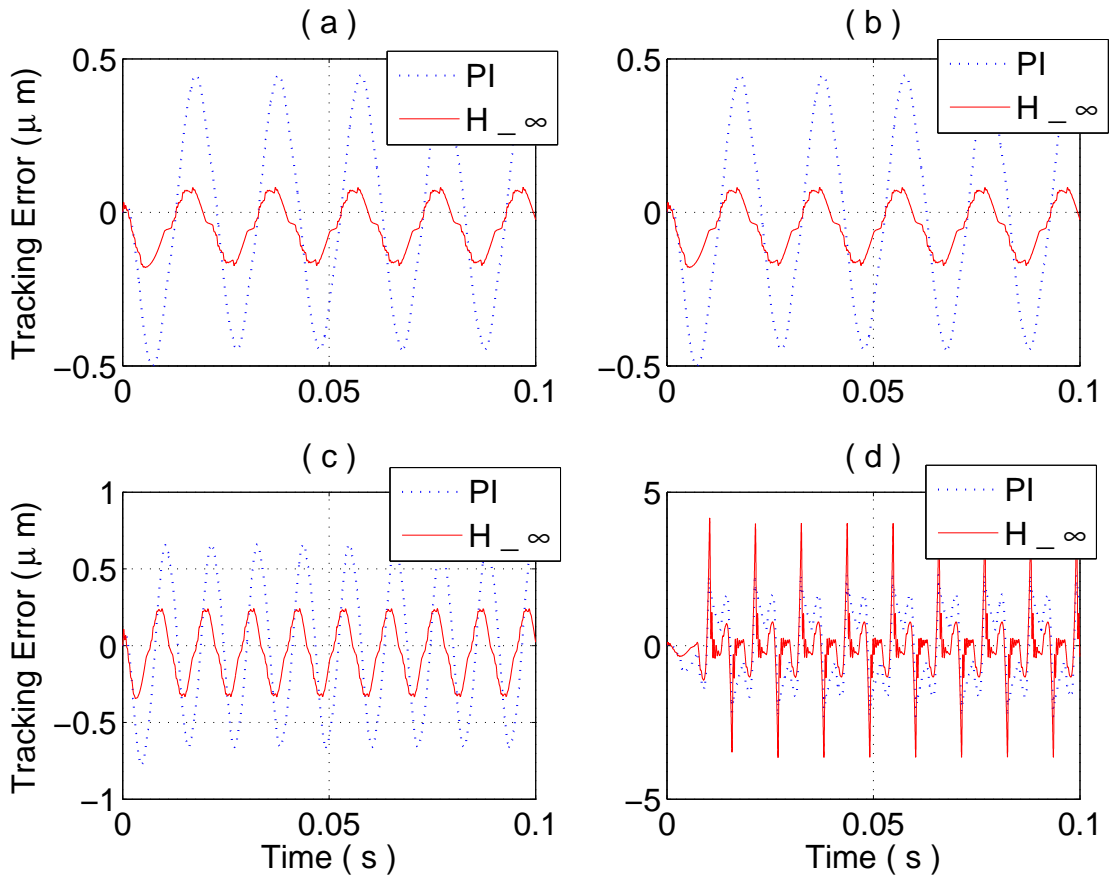


Figure 5.7: Simulations results for tracking error with PI and H_{∞} control: a) without rate limiter at 50 Hz, b) with rate limiter at 50 Hz, c) without rate limiter at 90 Hz, and d) with rate limiter at 90 Hz.

the system. The gains for the PI controller are chosen as $k_i = 2500$ and $k_p = 3$, which are obtained by tuning them for the best performance. The bounds used to calculate β for the SMC design are $k_0 = 0.05$ and $k_1 = 7$. For the H_∞ controller, we used the controller K_{fb} presented by (5.10). The results are presented in Table 5.1 and illustrated in Fig 5.8. Although the tracking error has acceptable values for frequencies less than 200 Hz, the results are presented from 1 Hz to 3000 Hz to show how this error scales with frequency. We notice that at 1 Hz the PI-controller outperforms the other controllers. This is expected because the PI-controller has a very high gain at frequencies close to zero, which dominates uncertainties. Although, the H_∞ controller includes integral action in our design, it performs worse than the PI controller alone because approximation was used to include integral action in the H_∞ controller. This appears as a shift of the tracking error from zero at very low frequency. This shift actually appears at all frequencies with the H_∞ controller but its size is smaller than the peak-to-peak error and not noticeable at high frequencies. The tracking error of the PI controller will continue increasing with the frequency until about 50 Hz. The error then stays almost constant, which is about $0.2 \mu\text{m}$ and slightly increases up to 100 Hz. Then it starts to increase fast again. The H_∞ controller has smaller tracking error than the PI control from 1 Hz to 100 Hz. Then it increases larger than the PI control. The Sliding-Mode controller (SMC) has larger tracking error than the other two methods when the frequency is less than 50 Hz, but it outperforms them for larger frequencies. It is also notable that SMC also has almost constant tracking error in the frequency band from 80–200 Hz. However, unlike the other two methods, the tracking error decreases after this band until close to the resonance frequency, when it starts to increase again. A more discussion for SMC frequency response is provided in Chapter 4. It is noted that it is not easy to get this fine frequency response experimentally, because there are some components in the experiment that affect the performance. We have seen in previous chapters the effect of the rate limiter for example, which will add a phase shift to the response that increases

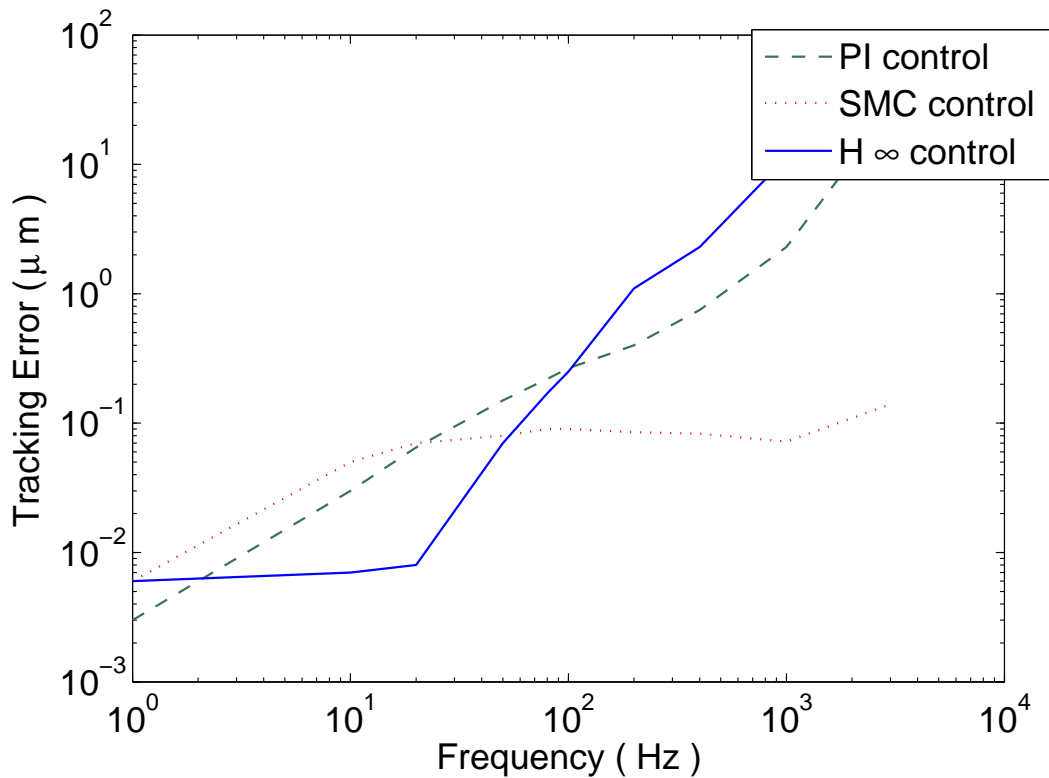


Figure 5.8: Simulations results for comparing the changes of the tracking errors with frequency for PI, SMC, and H_{∞} control.

with frequency particularly, beyond 100 Hz.

5.7 Summary

In this chapter we presented hysteresis inversion with H_{∞} feedback control in order to reduce the tracking error. We also introduced integral action in the H_{∞} controller to eliminate the DC error. We ran simulation to demonstrate the effectiveness of using this method. From comparisons, we conclude the following. First, including the inverse-operator in the closed-loop system improves the tracking performance. Second, depending on the choice of the weighting function, we can have a better performance for the H_{∞} controller over the PI controller for a selected frequency band, but

Table 5.1: Simulation results providing a comparison between maximum tracking errors for PI, SMC, and H_∞ control

freq.	PI Max $ e(t) $	SMC Max $ e(t) $	H_∞ Max $ e(t) $
1 Hz	0.003	0.006	0.006
10 Hz	0.03	0.05	0.006
20 Hz	0.065	0.07	0.006
50 Hz	0.15	0.08	0.07
80 Hz	0.22	0.09	0.17
100 Hz	0.265	0.09	0.25
200 Hz	0.4	0.085	1.1
400 Hz	0.7	0.08	2.3
1000 Hz	2.3	0.072	11.3
3000 Hz	26	0.14	47

we cannot achieve this performance for all frequencies. The H_∞ controller outperforms SMC only at low frequencies of a few tens of Hertz. Another shortcoming of the H_∞ controller is the high order of its transfer function, which makes it hard to implement.

Chapter 6

Conclusion and Future Work

6.1 Conclusions

Hysteresis is a nonlinear phenomenon, which appears in many control system applications. The performance of these systems, especially the ones that require precise tracking, can deteriorate very much or even can go unstable in the presence of hysteresis when good control designs are not considered. Motivated by applications such as Piezo-actuated nanopositioners, in this dissertation we considered systems with fast linear dynamics preceded by hysteresis. We followed a general scheme to deal with hysteresis, which incorporates both feedforward compensation and feedback techniques in the closed-loop control system. The feedforward compensation is simply an inverse hysteresis operator which is designed based on modeling the actual Hysteresis by Prandtl-Ishlinskii (PI) operators.

In this dissertation, we first discussed the effect of model uncertainties on the hysteresis operator. When an inverse PI operator is cascaded with its modeled PI operator, it results in a perfect inversion. However, when it is cascaded with actual hysteresis it will produce an inversion error. Because, we used the PI operator to implement our hysteresis, it is natural to characterize the inversion error by the parameter used to model the hysteresis, which are the threshold (i.e. radius of the play operators) and the vector of weights which determines the slope of each play operator. We assumed the uncertainty only happens on the weights of the play operators and assumed the thresh-

olds are exact. This is justified because we expect to have uncertainty on the slopes and intercepts of each segment of the hysteresis loop while the number of segments does not change. Having no uncertainty in thresholds also implies that the changes on the slopes happens at some certain amplitudes of the input signal. This motivated us to find bounds on the uncertainties appears in the slopes and intercepts directly. This method, which is based on the slopes and intercepts of the segments, applies to other operators that have piecewise linear characteristics. Moreover, we found that the bounds derived for the inversion error is less conservative than the ones obtained from the weight-threshold method.

This lead us to the second part of our work, where we used these bounds in both design and analysis of three different control methods. The first control method we explored was Proportional-Integral (PI) control. This method is extensively used in commercial applications such as Atomic-Force-Microscopes. The main drawback of the Proportional-Integral control is that it has low performance for applications that require high tracking speeds such as fast scanning. In existing work of systems with hysteresis, researchers compare their methods with PI or PID control as the standard methods. They show that their proposed methods outperform the PI controller, particularly at high frequency. However, by modifying the PI controller we showed that it provides comparable results with other methods and even outperform them at low frequency. In the PI control, we did not use the bounds on the inversion error in our design because it is a tuning control method. However, we used the bound on the inversion error that was calculated by the slope-intercept method to quantify the tracking error. We provided analysis for the tracking error when the system is driven by a periodic input. We discussed the effect of the model uncertainty on both the performance and stability. The most important part which we extracted from these expressions was that we can tell how the control gains affect the steady-state errors. We found for example that the proportional gain k_p can destabilize the system if increased in the presence of the uncertainty. The $\frac{k_i}{k_p}$ ratio

is not only important to make the system reach steady state fast but also to make the exponential terms generated in each segment to decay fast before the signal goes to the next segment at steady state. We also discussed how the tracking error scaled with frequency. We found that it has three regions; an increasing, an almost constant, and then another increasing region of tracking error for a low, medium, and high frequency bands, respectively. We exploited that the closed-loop system was expressed in two-time scales to separate variables using the singular perturbation theory. The slow variables came from the controller and the fast variables came from the plant. We also transformed the system in different coordinates to investigate the frequency effect on the system.

We then used a more sophisticated method, which is Sliding-Mode-Control as a feedback controller. In this method, we utilized the bounds on the inversion error in our design. In the existing work, the bounds on the uncertainties, which are used in the SMC designs have constant values and usually are determined by tuning them through simulations or experiments. However, in our method we found that the bounds depend on the size of the input signals and thus gave us more flexibility in the design. We compared the results which are obtained from this method with others such as servo-compensators and found they are comparable particularly at high frequency. However, this method has the advantage that it can track arbitrarily-shaped trajectories while servo-compensators are only designed for sinusoidal inputs. We also provided analysis of the tracking error when the trajectories enter the boundary layer. We again used the singular perturbation theory to derive the expression for the tracking error, where this time we put the system in multi-time scales by selecting the sliding-surface parameters. We provided simulation results which agree with the analytical expression for the tracking error as it changes with frequency. We also provided experimental results which qualitatively has a similar behavior as the simulation. We may mention here that we used a rate limiter as a safety component, to protect the nanopositioner in the experimental setup which, makes its behavior deviate from simulation especially at high

frequency. This was confirmed by adding a rate-limiter block in the simulated system.

The third controller, which we presented in this dissertation is the linear H_∞ controller. The simulation results of the tracking performance of this controller were compared with the other two methods. We found that the H_∞ Control has better tracking performance than the PI controller at frequency range from a few Hz to about 100 Hz. However, SMC outperforms both H_∞ and PI control at high frequencies. It is also noted that the H_∞ control is designed in an ad-hoc way, particularly, the choice of weighing functions. We also need to run numerical algorithms to obtain the controller.

6.2 Future Work

The work in this dissertation can be extended in several directions. First, some issues related to the hysteresis model requires more investigations and exploring. We used the finite dimensional Prandtl-Ishlinskii (PI) operator to model the hysteresis. Although the exact inverse of this model can be calculated, the model itself is always symmetrical for its ascending and descending branches, which is not the case for most of physical hysteresis. We propose to use other models, which are not symmetrical such as modified PI operator and examine its behavior with the proposed robust control methods in this research. We presented two methods to calculate the bounds on the inversion error, but we assumed only uncertainties in the weighting vector. The uncertainty in the thresholds will open many issues that require investigation. For example, the number of the segments may change and there will be mismatch between the operator and its inverse-operator. Providing analysis for performance and stability in these situations will help in understanding the behavior of the hysteresis operator and the choice of the feedback method to complement the feed-forward compensation. Moreover, we applied inputs on the positioner to operate in its full range

and produce a major loop and studied uncertainties and bounds for this case. It would be interesting to apply different signals which produce major and minor loops and study the effect of the uncertainty in both of them.

Second, we compared between different robust feedback control methods to improve the system performance. We provided design and analysis for these systems under some assumptions. There is still room to improve these methods and investigate areas which has not been explored. For the PI controller, for instance, we found that the inverse-operator can be introduced in the added feedforward branch instead of cascading it with the hysteresis. Preliminary experimental results showed the potential to have smaller tracking errors for this method. This can be a result of having the inverse operator outside the closed-loop which makes it less susceptible to the harmonics generated in the closed-loop. However, the analysis for this method is much more complicated than the cascaded operators because a signal from the feedback controller will be added to the output of the inverse-operator and cause a mismatch between operators. We also provided the analysis for the PI control and for SMC control when the applied inputs are periodic. It will be more comprehensive to determine the inversion and tracking errors for more general input references. Furthermore, our design and analysis was limited to linear plants with stable poles; however in many nanopositioners the plant includes some zeros in the right hand-side. It would be of interest to investigate the design and analysis of non-minimum phase systems. Another assumption, which is also motivated by the piezo-actuator is that we have a large bandwidth or fast dynamics of the linear plant. This was helpful in both design and analysis of the system. We succeeded to improve the tracking performance of frequency range, which was about a tenth of the bandwidth. The investigation of having narrow bandwidths would show how the controller dynamics interact with plant dynamics and affect the control system design.

BIBLIOGRAPHY

BIBLIOGRAPHY

- [1] X. Tan and J. S. Baras, "Modeling and control of hysteresis in magnetostrictive actuators," *Automatica*, vol. 40, no. 9, pp. 1469–1480, 2004.
- [2] R. Smith, *Smart Material Systems: Model Developments*. Society of Industrial and Applied Mathematics, 2005.
- [3] C.J and C. P, "Piezoelectric and allied phenomena in rochelle salt," *Comput Rend Acad Sci*, vol. 91, pp. 294–297, 1880.
- [4] W. J. Buehler and F. E. Wang, "A summary of recent research on the nitilon alloys and thier potential application in ocean engineering," *Ocean Engineering*, vol. 1, no. 1, pp. 105–120, 1968.
- [5] Z. Chen, X. Tan, and M. Shahinpoor, in *Proceedings of the 2005 IEEE/ASME International Conference on the Advanced Intelligent Mechatronics*, 2005, pp. 60–65.
- [6] H. S. Majumdar, A. Bandyopadhyay, A. Bolognesi, and A. J. Pal, "Memory device applications of a conjugated polymer: Role of space charges," *Journal of Applied Physics*, vol. 91, no. 4, pp. 2433–2437, 2002.
- [7] S. Devasia, E. Eleftheriou, and S.O.Moheimani, "A survey of control issues in nanopositioning," *IEEE Transactions on Control Systems Technology*, vol. 15, no. 5, pp. 802 –823, sept. 2007.
- [8] Y. K. Yong, S.S.Aphale, and S. R. Moheimani, "Design, identification, and control of a flexure-based xy stage for fast nanoscale positioning," *IEEE Transactions On Nanotechnology*, vol. 8, no. 1, pp. 46–54, 2009.
- [9] D. Croft, G. Shedd, and S. Devasia, "Creep, hysteresis, and vibration compensation for piezoactuators: atomic force microscopy application," in *Proceedings of the 2000 American Control Conference*, 2000, pp. 2123–2128.
- [10] D. Jiles and D. Atherton, "Theory of ferromagnetic hysteresis," *Journal of Magnetism and Magnetic Materials*, vol. 61, no. 5, pp. 48–60, 1986.

- [11] A. Adly, I. Mayergoyz, and A. Bergqvist, "Preisach modeling of magnetostrictive hysteresis," *Journal of Applied Physics*, vol. 69, pp. 5777–5779, 1991.
- [12] K. Kuhnen, "Modeling, identification and compensation of complex hysteretic nonlinearities - a modified Prandtl-Ishlinskii approach," *European Journal of Control*, vol. 9, no. 4, pp. 407–418, 2003.
- [13] J. Muir, "On the recovery of iron from overstrain," *Philosophical Transactions of the Royal Society of London Series A*, vol. 193, pp. 1–46, 1900.
- [14] F. G. Baily, "The hysteresis of iron and steel in a rotating magnetic field," *Philosophical Transactions of the Royal Society of London Series A*, vol. 187, pp. 715–746, 1896.
- [15] K. Kuhnen and Janocha, "Inverse feedforward controller for complex hysteretic nonlinearities in smart-material systems," *Control and Intelligent systems*, vol. 29, no. 3, pp. 74–83, 2001.
- [16] M. Krasnoselskii and A. Pokrovskii, "Periodic oscillation in systems with relay nonlinearities," *Akademiia Nauk SSSr, Doklady*, vol. 216, pp. 733–736, 1974.
- [17] ———, *Systems with Hysteresis*. New York: Springer-Verlag, 1989.
- [18] I. Mayergoyz, "Mathematical models of hysteresis," *IEEE Transactions on Magnetics*, vol. 22, no. 5, pp. 603–608, 1986.
- [19] P. Ge and M. Jouaneh, "Generalized preisach model for hysteresis nonlinearity of piezoceramic actuators," *Precision Engineering*, vol. 20, no. 2, pp. 99–111, 1997.
- [20] J. Schfer and H. Janocha, "Compensation of hysteresis in solid-state actuators," *Sensors and Actuators A: Physical*, vol. 49, no. 1-2, p. 97102, 1995.
- [21] K. Kuhnen and Janocha, "Adaptive inverse control of piezoelectric actuators with hysteresis operator," in *Proceedings of the European Control Conference*, Karlsruhe, Germany, 1999, paper F 0291.
- [22] M. A. Janaideh, S. Rakheja, and C.-Y. Su, "An analytical generalized prandtl-ishlinskii model inversion for hysteresis compensation in micropositioning control," *IEEE/ASME Trans. on Mechatron.*, vol. 16, no. 4, pp. 734–744, 2011.
- [23] M. Brokate and J. Sprekels, *Hysteresis and phase transitions*. Springer Verlag, 1996.

- [24] R. Mrad and H. Hu, "A model for voltage-to-displacement dynamics in piezoceramic actuators subject to dynamic-voltage excitations," *IEEE/ASME Transactions on Mechatronics*, vol. 7, no. 4, pp. 479–489, 2002.
- [25] X. Tan and J. Baras, "Adaptive identification and control of hysteresis in smart materials," *IEEE Transactions on Automatic Control*, vol. 50, no. 6, pp. 827–839, 2005.
- [26] R. Iyer and X. Tan, "Approximate inversion of the preisach hysteresis operator with application to control of smart actuators," *IEEE Transactions on Automatic Control*, vol. 50, no. 6, pp. 798–810, 2005.
- [27] H. Hu and R. Mrad, "On the classical preisach model for hysteresis in piezoceramic actuators," *Mechatronics*, vol. 13, no. 2, pp. 85–94, 2002.
- [28] H. Hu, H. Georgiou, and R. Ben-Mrad, "Enhancement of tracking ability in piezoceramic actuators subject to dynamic excitation conditions," *IEEE/ASME Transactions on Mechatronics*, vol. 10, no. 2, pp. 230–239, 2005.
- [29] D. Carnevale, S. Nicosia, and L. Zaccarian, "Generalized constructive model of hysteresis," *IEEE Transactions on Magnetics*, vol. 42, no. 12, pp. 3809–3817, 2006.
- [30] R. Mrad and H. Hu, "Dynamic modeling of hysteresis in piezoceramics," in *IEEE/ASME International Conference on Advanced Intelligent Mechatronics*, 2001, pp. 510–515.
- [31] J. W. Macki, P. Nistri, and P. Zecca, "Mathematical models for hysteresis," *SIAM Review*, vol. 35, no. 1, pp. 94–123, 1993.
- [32] R. Iyer and M. Shirley, "Mathematical models of hysteresis," *IEEE Transactions on Magnetics*, vol. 40, no. 5, pp. 3227–3239, 1986.
- [33] K. Hoffmann and G. H. Meyer, "A least squares method for finding the preisach hysteresis operator from measurements," *Numerische Mathematik*, vol. 55, no. 6, pp. 695–710, 1989.
- [34] P. Krejci and K. Kuhnen, "Inverse control of systems with hysteresis and creep," *IEE Proceedings - Control Theory and Applications*, vol. 148, no. 3, pp. 185–192, 2001.
- [35] H. Janocha and K. Kuhnen, "Real-time compensation of hysteresis and creep in piezoelectric actuators," *Sensors and Actuators A: Physical*, vol. 79, no. 2, pp. 83–89, 2000.
- [36] G. Tao and P. Kokotovic, "Adaptive control of plants with unknown hystereses," *IEEE Transactions on Automatic Control*, vol. 40, no. 2, pp. 200–212, 1995.

- [37] H. Hu and R.Mrad, "Active control of flexible systems," *Journal of Optimization Theory and Applications*, vol. 25, no. 3, pp. 415–436, 1978.
- [38] K. K. Leang and S. Devasia, "Feedback-linearized inverse feedforward for creep, hysteresis, and vibration compensation in afm piezoactuators," *IEEE Transactions on Control Systems Technology*, vol. 15, no. 5, pp. 209–216, 2007.
- [39] Y. Okazaki, "A micro-positioning tool post using a piezoelectric actuator for diamond turning machines," *Precision Engineering*, vol. 12, no. 3, pp. 151–156, 2003.
- [40] J. Zhong and B. Yao, "Adaptive robust precision motion control of a piezoelectric positioning stage," *IEEE Transactions on Control Systems Technology*, vol. 16, no. 5, pp. 1039–1046, 2008.
- [41] Y. Wu and Q. Zou, "Iterative control approach to compensate for both the hysteresis and the dynamics effects of piezo actuators," *IEEE Transactions on Control Systems Technology*, vol. 15, no. 5, pp. 936–944, 2007.
- [42] M. Tsai, "Robust tracking control of a piezoactuator using a new approximate hysteresis model," *Journal of dynamic systems, measurement, and control*, vol. 125, pp. 96–102, 2003.
- [43] G. Schitter, P. Menold, H. Knapp, F. Allgwer, and A. Stemmer, "High performance feedback for fast scanning atomic force microscopes," *Review of Scientific Instruments*, vol. 72, no. 8, pp. 3320–3327, 2001.
- [44] S. Salapaka, A. Sebastian, J. Cleveland, and M. Salapaka, "High bandwidth nano-positioner: A robust control approach," *Review of Scientific Instruments*, vol. 73, no. 9, pp. 3232–3241, 2002.
- [45] A. Sebastian and S. Salapaka, "Design methodologies for robust nano-positioning," *IEEE Transactions on Control Systems Technology*, vol. 13, no. 6, pp. 868–876, 2005.
- [46] J. Slotine and W.Li, *Applied Nonlinear control*. Printce-Hall, 1991.
- [47] X. Chen, T. Hisayama, and C.-Y. Su, "Pseudo-inverse-based adaptive control for uncertain discrete time systems preceded by hysteresis," *Journal of Dynamic Systems*, vol. 45, pp. 469–476, 2008.
- [48] X. Tan and H. K. Khalil, "Two-time-scale averaging of systems involving operators and its application to adaptive control of hysteretic systems," in *Proceedings of the 2009 American Control Conference*, 2009, pp. 4476–4481.

- [49] S. Valadkhan, K. Morris, and A. Khajepour, "Robust PI control of hysteretic systems," in *Proceedings of the 47th IEEE Conference on Decision and Control*, 2008, pp. 3787–3792.
- [50] B. Jayawardhana, H. Logemann, and E. Ryan, "PID control of second-order systems with hysteresis," in *Proceedings of the 46th IEEE Conference on Decision and Control*, 2007, pp. 4626–4630.
- [51] C. Knospe, "Pid control," *IEEE Control Systems Magazine*, vol. 26, no. 1, pp. 30–31, 2006.
- [52] H. Logemann, E. Ryan, and Shvartsman, "Integral control of infinite-dimensional systems in the presence of hysteresis: An input-output approach," *ESAIM: Control, Optimization and Calculus of Variations*, vol. 13, pp. 458–483, 2007.
- [53] P. Ge and M. Jouaneh, "Tracking control of a piezoceramic actuator," *IEEE Transactions on Control Systems Technology*, vol. 4, no. 3, pp. 209–216, 1996.
- [54] A. Esbrook, M. Guibord, X. Tan, and H. K. Khalil, "Control of systems with hysteresis via servocompensation and its application to nanopositioning," in *Proceedings of the 2010 American Control Conference*, 2010, pp. 6531–6536.
- [55] A. Esbrook, X. Tan, and H. K. Khalil, "Control of systems with hysteresis via servocompensation and its application to nanopositioning," *IEEE Transactions on Control Systems Technology*, to appear, DOI: 10.1109/TCST.2012.2192734.
- [56] J. Shen, W. Jywea, H. Chiang, and Y. Shub, "Precision tracking control of a piezoelectric-actuated system," *Precision Engineering*, vol. 32, pp. 71–78, 2008.
- [57] S. Bashash and N. Jalili, "Robust multiple frequency trajectory tracking control of piezo-electrically driven micro/nanopositioning systems," *IEEE Transactions on Control Systems Technology*, vol. 15, no. 5, pp. 867–878, sept. 2007.
- [58] H. Liaw, B. Shirinzadeh, and J. Smith, "Enhanced sliding mode motion tracking control of piezoelectric actuators," *Sensors and Actuators A*, vol. 138, pp. 194–202, 2007.
- [59] C. Jan and C. Hwang, "A nonlinear observer-based sliding-mode control for piezoelectric actuator systems: Theory and experiments," *Journal of the Chinese Institute of Engineers*, vol. 27, no. 1, pp. 9–22, 2004.
- [60] M. Edardar, X. Tan, and H. K. Khalil, "Sliding-mode tracking control of piezo-actuated nanopositioner," in *Proceedings of the 2012 American Control Conference*, 2012, pp. 3825–3830.

- [61] Q. Wei, C. Hu, and D. Zhang, "Precision control of piezoelectric actuated mechanism in scanning tunneling microscope," in *Proceedings of the 8th World Congress on Intelligent Control and Automation (WCICA)*, 2010, pp. 1262–1267.
- [62] Y. Wu and Q. Zou, "Robust inversion-based 2-dof control design for output tracking: Piezoelectric-actuator example," *IEEE Transactions on Control Systems Technology*, vol. 17, no. 5, pp. 1069–1082, 2009.
- [63] D. Youla and J. Bongiorno, "A feedback theory of two-degree-of-freedom optimal wiener-hopf design," *IEEE Transactions on Automatic Control*, vol. 30, no. 7, pp. 652–665, Jul 1985.
- [64] J. Howze and S. Bhattacharyya, "Robust tracking, error feedback, and two-degree-of-freedom controllers," *IEEE Transactions on Automatic Control*, vol. 42, no. 7, pp. 990–983, Jul 1997.
- [65] S. Hara and T. Sugie, "Independent parameterization of two-degree-of-freedom compensators in general robust tracking systems," *IEEE Transactions on Automatic Control*, vol. 33, no. 1, pp. 59–67, Jan 1988.
- [66] G. Schitter, A. Stemmer, and F. Allgwer, "Robust two-degree-of-freedom control of an atomic force microscope," *Asian Journal of Control*, vol. 6, no. 2, p. 156163, 2004.
- [67] A. Sebastian and S. Salapaka, "Robust broadband nanopositioning: fundamental trade-offs, analysis, and design in a two-degree-of-freedom control framework," *Nanotechnology*, vol. 20, no. 36, pp. 1–16, 2009.
- [68] J. Cuttino, A. Miller, and D. Schinstock, "Performance optimization of a fast tool servo for single-point diamond turning machines," *IEEE/ASME Transactions on Mechatronics*, vol. 4, no. 2, pp. 169–179, 1999.
- [69] R. C. Barrett and C. F. Quate, "Optical scan-correction system applied to atomic force microscopy," *Review of Scientific Instruments*, vol. 62, no. 6, pp. 1393–1399, 1991.
- [70] R. Iyer and X. Tan, "Control of hysteretic systems through inverse compensation: Inversion algorithms, adaptation, and embedded implementation," *IEEE Control Systems Magazine*, vol. 29, no. 1, pp. 83–99, 2009.
- [71] E. Prempain and I. Postlethwaite, "Feedforward control: A full-information approach," *Automatica*, vol. 37, no. 1, pp. 17–28, Jan 2001.

- [72] K. Zhou and J. Doyk, *Essentials of Robust Control*. Tom Robbins, 1998.
- [73] H. Khalil, *Nonlinear Systems*. Printce-Hall, 2002.
- [74] P. Kokotovic, H. K. Khalil, and J. O'reilly, *Singular Perturbation Methods in Control Analysis*. SIAM, 1999.
- [75] V. Utkin, J.Guldner, and J. Shi, *Sliding Mode Control in Electromechanical systems*. Taylor & Francis, 1999.
- [76] Q. Xu and Y. Li, "Radial basis function neural network control of an XY micropositioning stage without exact dynamic model," in *Proceedings of the 2009 IEEE/ASME International Conference on Advanced Intelligent Mechatronics*, july 2009, pp. 498–503.